

**Photoemission electron microscopy  
of magneto-ionic effects in  
 $\text{La}_{0.7}\text{Sr}_{0.3}\text{MnO}_3$**

Der Fakultät für Physik  
der Universität Duisburg-Essen  
zur Erlangung des akademischen Grades eines  
Doktors der Naturwissenschaften (Dr. rer. nat.) vorgelegte

Dissertation  
von  
Marek Wilhelm

geboren in Neuss

Erstgutachter: Prof. Dr. Claus M. Schneider (Universität Duisburg-Essen)  
Zweitgutachterin: Prof. Dr. Martina Müller (Universität Konstanz)

Tag der mündlichen Prüfung: 04.11.2021



*“Das Leben und sein Kind.”*

Cheech & Chong

## Kurzzusammenfassung

Eine der herausforderndsten Aufgaben in der Nanoelektronik ist die Realisierung neuartiger Bauelemente mit geringem Energieverbrauch für die Anwendung in nicht-flüchtigen Datenspeichern, Verarbeitungs-, Transduktions- und Sensoreinheiten. Die Steuerung des Magnetismus durch elektrische Felder, welche auf dem magneto-elektrischen (ME) Effekt basiert, könnte den Weg für ein alternatives Konzept zur Elektronik auf Si-Basis ebnen.

Zahlreiche Studien über magnetoelektrische Materialien zeigten eine ME-Kopplung über Kristallgitterdeformation, Ladungsträgerdotierung und Grenzflächenaustauschprozesse. In jüngster Zeit erhielt das Gebiet der Magnetoionik zunehmend Aufmerksamkeit, da die spannungsgesteuerte chemische Interkalation ionischer Spezies einen neuen Weg zur Kontrolle des Magnetismus in bulk-Materialien eröffnete.

Die vorliegende Arbeit berichtet über das durch ein elektrisches Feld induzierte magnetische Schalten in einem  $\text{La}_{0.7}\text{Sr}_{0.3}\text{MnO}_3$  (LSMO)-Dünnschicht-Modellsystem. Als stark korreliertes magnetisches Oxid kann LSMO in Abhängigkeit von der vorherrschenden Oxidationsstufe der Mangankationen in mehreren magnetischen Zuständen auftreten. Die Migration von Sauerstoffleerstellen und die lokale Umverteilung der Sauerstoffkonzentration verändern das Gleichgewicht der Doppelaustausch- und Superaustauschwechselwirkung zwischen Mangan- und Sauerstoffionen erheblich und ermöglichen so eine Kontrolle der chemischen, strukturellen und magnetischen Phasenübergänge.

10 nm dicke  $\text{La}_{0.7}\text{Sr}_{0.3}\text{MnO}_3$  Dünnschichten wurden unter Verwendung gepulster Laserdeposition (*Pulsed Laser Deposition, PLD*), epitaktisch auf  $\text{TiO}_2$ -terminierten Nb(0.5%):  $\text{SrTiO}_3$  (001)-Substraten gewachsen. Die Morphologie und die Kristallstruktur wurden durch *Atomic Force Microscopy* (AFM) und *X-ray Diffraction* (XRD) charakterisiert, wobei ein epitaktischer, einkristalliner Film und eine atomar flache Oberfläche ermittelt wurde. *Vibrating Sample Magnetometry* (VSM) und *X-ray Magnetic Circular Dichroism* (XMCD) wurden verwendet, um die magnetischen Eigenschaften zu untersuchen. Ferner wurden die elektronische Struktur und die chemischen Eigenschaften durch *Hard X-ray Photoemission Spectroscopy* (HAXPES) und *X-ray Absorption Spectroscopy* (XAS) bestimmt.

Mittels *Local Conductivity Atomic Force Microscopy* (LC-AFM) wurde der Widerstand von LSMO Dünnschichten elektrisch moduliert. Um die in den elektrisch modifizierten Bereichen vorhandenen Mikro-Redoxprozesse zu untersuchen, führten wir eine kombinierte und elementenselektive *XPEEM*-Studie im XAS- und XMCD-Modus durch. Die Ergebnisse zeigen das direkte Zusammenspiel zwischen spezifischem Widerstand, chemischer Zusammensetzung und magnetischer Ordnung, welches durch einen Sauerstoffaustauschprozess über die LSMO-Filmoberfläche gesteuert wird. Signifikante chemische Modifikationen werden im hochohmigen Zustand beobachtet, in dem der Einbau von Sauerstoffleerstellen zu einer deutlichen Valenzänderung von  $\text{Mn}^{3+/4+}$  zu  $\text{Mn}^{2+/3+}$  führt. Ferner wird eine direkte Korrelation zwischen Sauerstoffmangel und einer Verschlechterung der ferromagnetischen Eigenschaften gefunden.

Vor diesem Hintergrund liefern die Ergebnisse dieser Arbeit neue Einblicke in die durch Leerstellen angetriebene magnetoionische Steuerung magnetoelektrischer Oxide. Darüber hinaus eröffnen sie neue Wege zur mehrphasigen Kontrolle physikalischer und chemischer Eigenschaften in Magnetoxyden und neuartigen ionotronischen Bauelementen.

## Abstract

One of the most challenging tasks in future nanoelectronics is the realization of novel low-power consumption devices for the application in non-volatile memories, processing, transduction and sensing units. Electric-field-control of the magnetism, which is based on the *magnetoelectric* (ME) effect, may pave the way towards an alternative concept to Si-based electronics relying on dissipative electrical currents. Numerous studies reported on magnetoelectric materials showing ME coupling via strain, charge carrier doping and interfacial exchange processes. Recently, the field of magneto-ionics received increased attention as the voltage-driven chemical intercalation of ionic species opened a novel route towards the control of magnetism in bulk materials.

This thesis reports on electric-field-induced magnetic switching in a  $\text{La}_{0.7}\text{Sr}_{0.3}\text{MnO}_3$  (LSMO) thin film prototype system. As a strongly correlated magnetic oxide LSMO can appear in multiple magnetic states depending on the prevalent oxidation state of the manganese cations. The migration of oxygen vacancies and the local redistribution of the oxygen concentration profoundly alters the balance of the double-exchange and superexchange interactions between manganese and oxygen ions, thus providing a granular control of chemical, structural and magnetic phase transitions.

10 nm thick  $\text{La}_{0.7}\text{Sr}_{0.3}\text{MnO}_3$  films were epitaxially grown on  $\text{TiO}_2$ -terminated Nb (0.5%): $\text{SrTiO}_3$  (001) substrates by means of *pulsed laser deposition* (PLD). The morphology and the crystal structure were characterized by atomic force microscopy (AFM) and X-ray diffraction (XRD) revealing an epitaxial, single crystalline film and an atomically flat surface. Vibrating sample magnetometry (VSM) and *X-ray magnetic circular dichroism* (XMCD) were used to investigate the magnetic properties. Further, the electronic structure and the chemical properties were probed by *hard X-ray photoemission spectroscopy* (HAXPES) and *X-ray absorption spectroscopy* (XAS). *Local conductivity atomic force microscopy* (LC-AFM) was utilized to electrically modulate the resistance of LSMO thin films. To investigate the micro-scale redox processes present in the electrically modified areas, we performed a combined and element-selective *X-ray photoemission electron microscopy* (XPEEM) study in XAS and XMCD mode. The results demonstrate the direct interplay between resistivity, chemical composition, and magnetic ordering driven by an oxygen exchange process across the LSMO film surface. Significant chemical modifications are observed in the high resistive state, where the incorporation of oxygen vacancies leads to a distinct valence change from  $\text{Mn}^{3+/4+}$  to  $\text{Mn}^{2+/3+}$ . Further, a direct correlation between oxygen deficiency and a degradation of the ferromagnetic properties is found. In this light, the results of this thesis provide novel insights into the vacancy-driven magneto-ionic control of magnetoelectric oxides for the example LSMO. Moreover, they open up novel routes towards a multiphase-control of physical and chemical properties in magnetic oxides and novel ionotronic devices.

# Contents

<b>I</b>	<b>Theoretical Background</b>	<b>1</b>
<b>1</b>	<b>Introduction</b>	<b>3</b>
<b>2</b>	<b>Resistive Switching in Complex Oxides</b>	<b>7</b>
2.1	Introduction and Resistive Switching Mechanisms . . . . .	7
2.2	Valence Change Model . . . . .	10
2.3	Electronic Transport Across Metal/Insulator Interfaces . . . . .	11
<b>3</b>	<b>Properties of Lanthanum Manganites</b>	<b>15</b>
3.1	Introduction . . . . .	15
3.2	Crystal- and Electronic Structure . . . . .	16
3.2.1	Jahn-Teller-Effect . . . . .	18
3.3	Magnetic Structure . . . . .	20
3.3.1	Magnetic Moment in $\text{La}_{1-x}\text{Sr}_x\text{MnO}_3$ . . . . .	20
3.3.2	Superexchange Interaction . . . . .	21
3.3.3	Double-Exchange Interaction . . . . .	26
<b>4</b>	<b>Photoelectron Emission Spectroscopy &amp; Microscopy</b>	<b>27</b>
4.1	Photoemission Process . . . . .	28
4.2	The Photoexcitation Process - Fermi's Golden Rule . . . . .	30
4.3	Electron Spectroscopy for Chemical Analysis (ESCA) . . . . .	31
4.3.1	X-Ray Photoemission Spectroscopy (XPS) . . . . .	32
4.3.2	X-Ray Absorption Spectroscopy (XAS) . . . . .	33
4.4	Spin-Orbit-Coupling (SOC) . . . . .	34
4.5	X-Ray Magnetic Circular Dichroism (XMCD) . . . . .	35
4.6	Photoemission Electron Microscopy (PEEM) . . . . .	37
4.7	Synchrotron Radiation Photon Source . . . . .	40

<b>II</b>	<b>Experimental Methods</b>	<b>43</b>
<b>5</b>	<b>Sample Preparation</b>	<b>45</b>
5.1	Substrate Termination . . . . .	45
5.2	Pulsed Laser Deposition . . . . .	46
5.3	Reflection High Energy Electron Diffraction . . . . .	48
<b>6</b>	<b>Characterization Methods</b>	<b>51</b>
6.1	Atomic Force Microscopy (AFM) . . . . .	51
6.2	X-Ray Diffraction (XRD) . . . . .	52
6.3	Vibrating Sample Magnetometry (VSM) . . . . .	53
<b>III</b>	<b>Experimental Results</b>	<b>57</b>
<b>7</b>	<b>Growth and Characterization of <math>\text{La}_{0.7}\text{Sr}_{0.3}\text{MnO}_3</math> Thin Films</b>	<b>59</b>
7.1	PLD Growth Recipe for LSMO . . . . .	59
7.2	Structure and Morphology . . . . .	60
7.3	Electronic Structure . . . . .	62
7.4	Magnetic Properties . . . . .	64
	7.4.1 Vibrating Sample Magnetometry (VSM) . . . . .	64
	7.4.2 X-Ray Magnetic Circular Dichroism . . . . .	67
	7.4.3 Conclusion . . . . .	70
<b>8</b>	<b>Voltage-Driven Modification of Chemical and Physical Properties in <math>\text{La}_{0.7}\text{Sr}_{0.3}\text{MnO}_3</math> Thin Films</b>	<b>73</b>
8.1	Resistive Switching in $\text{La}_{0.7}\text{Sr}_{0.3}\text{MnO}_3$ . . . . .	73
	8.1.1 Voltage Sweep Measurements . . . . .	73
	8.1.2 Summary . . . . .	77
8.2	PEEM Study of the Magneto-Ionic Effect in $\text{La}_{0.7}\text{Sr}_{0.3}\text{MnO}_3$ . . . . .	78
	8.2.1 Electric Field Modification by LC-AFM . . . . .	78
	8.2.2 Chemical Fingerprint of Electrically Modified $\text{La}_{0.7}\text{Sr}_{0.3}\text{MnO}_{3-\delta}$ . . . . .	81
	8.2.3 Magnetic Fingerprint . . . . .	88
	8.2.4 Brownmillerite Phase: Structural Phase Transition in $\text{La}_{0.7}\text{Sr}_{0.3}\text{MnO}_{3-\delta}$ . . . . .	91
<b>9</b>	<b>Summary and Conclusions</b>	<b>99</b>

<b>A</b>	<b>Reciprocal Space Map (RSM)</b>	<b>103</b>
<b>B</b>	<b>Magnetic Characterization of varying LSMO Thin Film Thicknesses</b>	<b>105</b>
<b>C</b>	<b>Principal Component Analysis</b>	<b>109</b>
	<b>Bibliography</b>	<b>115</b>

---

## List of Abbreviations

---

<b>ME</b>	<b>M</b> agneto <b>e</b> lectric effect
<b>LSMO</b>	$\text{La}_{0.7}\text{Sr}_{0.3}\text{MnO}_3$
<b>PLD</b>	<b>P</b> ulsed <b>L</b> aser <b>D</b> eposition
<b>RHEED</b>	<b>R</b> eflection <b>H</b> igh <b>E</b> nergy <b>E</b> lectron <b>D</b> iffraction
<b>AFM</b>	<b>A</b> tom <b>F</b> orce <b>M</b> icroscopy
<b>XRD</b>	<b>X</b> - <b>R</b> ay <b>D</b> iffraction
<b>HAXPES</b>	<b>H</b> ard <b>X</b> - <b>R</b> ay <b>P</b> hoto <b>e</b> mission <b>S</b> pectroscopy
<b>XMCD</b>	<b>X</b> - <b>R</b> ay <b>M</b> agnetic <b>C</b> ircular <b>D</b> ichroism
<b>LC-AFM</b>	<b>L</b> ocally <b>C</b> onductive <b>A</b> tom <b>F</b> orce <b>M</b> icroscopy
<b>XPEEM</b>	<b>X</b> -ray <b>P</b> hoto <b>e</b> mission <b>E</b> lectron <b>M</b> icroscopy
<b>TMO</b>	<b>T</b> ransition <b>M</b> etal <b>O</b> xide
<b>TEM</b>	<b>T</b> ransmission <b>E</b> lectron <b>M</b> icroscopy
<b>MR</b>	<b>M</b> agneto <b>r</b> esistance
<b>Fe</b>	<b>F</b> errum
<b>O</b>	<b>O</b> xygen
<b>PV</b>	<b>P</b> erovskite
<b>BM</b>	<b>B</b> rown <b>m</b> illerite
<b>Nb:STO</b>	<b>N</b> iobium: <b>SrTiO</b> <sub>3</sub>
<b>Mn</b>	<b>M</b> anganese
<b>RS</b>	<b>R</b> esistive <b>S</b> witching
<b>VCM</b>	<b>V</b> alence <b>C</b> hange <b>M</b> odel
<b>ReRAM</b>	<b>R</b> esistive switching <b>R</b> andom <b>A</b> ccess <b>M</b> emory
<b>HRS</b>	<b>H</b> igh <b>R</b> esistance <b>S</b> tate
<b>LRS</b>	<b>L</b> ow <b>R</b> esistance <b>S</b> tate
<b>BRS</b>	<b>B</b> ipolar <b>R</b> esistive <b>S</b> witching
<b>CC</b>	<b>C</b> urrent <b>C</b> ompliance
<b>MIM</b>	<b>M</b> etal- <b>I</b> nsulator- <b>M</b> etal
<b>CF</b>	<b>C</b> onducting <b>F</b> ilament
<b>TE</b>	<b>T</b> hermo <b>i</b> onic <b>E</b> mission

<b>FE</b>	<b>Field Emission</b>
<b>TFE</b>	<b>Thermoionic- Field Emission</b>
<b>MIT</b>	<b>Metal Insulator Transition</b>
<b>PM</b>	<b>Paramagnetic</b>
<b>FM</b>	<b>Ferromagnetic</b>
<b>CMR</b>	<b>Colossal Magneto Resistance</b>
<b>DE</b>	<b>Double Exchange interaction</b>
<b>JTE</b>	<b>Jahn-Teller-Effect</b>
<b>ESCA</b>	<b>Electron Spectroscopy for Chemical Analysis</b>
<b>ARPES</b>	<b>Angular Resolved Photoemission Spectroscopy</b>
<b>IMPF</b>	<b>Inelastic Mean Free Path</b>
<b>XPS</b>	<b>X-ray Photoemission Spectroscopy</b>
<b>XAS</b>	<b>X-ray Absorption Spectroscopy</b>
<b>VB</b>	<b>Valence Band</b>
<b>CL</b>	<b>Core Level</b>
<b>AE</b>	<b>Auger Electron</b>
<b>FY</b>	<b>Fluorescence Yield</b>
<b>TEY</b>	<b>Total Electron Yield</b>
<b>WL</b>	<b>White Line</b>
<b>XANES</b>	<b>X-ray Absorption Near Edge Spectroscopy</b>
<b>SOC</b>	<b>Spin Orbit Coupling</b>
<b>LEEM</b>	<b>Low Energy Electron Microscopy</b>
<b>OL</b>	<b>Objective Lens</b>
<b>ETL</b>	<b>Electrostatic Lens</b>
<b>MPA</b>	<b>Magnetic Prism Array</b>
<b>ROI</b>	<b>Region Of Interest</b>
<b>RMS</b>	<b>Root Mean Square</b>
<b>CVD</b>	<b>Chemical Vapour Deposition</b>
<b>MBE</b>	<b>Molecular Beam Epitaxy</b>
<b>ALS</b>	<b>Advanced Light Source</b>
<b>UNCD</b>	<b>Ultrananocrystalline Diamond</b>
<b>PCA</b>	<b>Principal Component Analysis</b>
<b>O-NMF</b>	<b>Ortho- Non-Negative Matrix Factorization</b>
<b>DOS</b>	<b>Density Of States</b>

---

## List of Symbols

---

$T_C$	Curie temperature
$T_N$	Néel temperature
$V$	Voltage
$V_O^{\bullet\bullet}$	Oxygen vacancy
$\Phi$	Work function
$F_E$	Fermi energy
$N_D$	Donor density
$\chi_s$	Electron affinity of the semiconductor
$e$	Electron charge
$k_B T$	Boltzmann's const.
$x$	Distance from the interface
$\epsilon$	Dielectric const. of the vacancy doped oxide
$x_D$	Width of the depletion region
$N_D$	Donor density
$T$	Absolute temperature
$m^*$	Effective mass
$\kappa$	Relative dielectric const. oxide layer
$t_{Ox,wq}$	Equivalent oxide thickness
$A^{**}$	Effective Richardson const.
$T$	Tolerance factor

$H$	Hamiltonian
$c_i$	Annihilation operator
$c_j^+$	Creation operator
$U$	Coulomb energy
$t$	Hopping integral
$\vec{x}$	Spatial coordinate vector
$\vec{k}$	Momentum vector
$\vec{s}$	Spin vector
$\lambda_{IMPF}$	Inelastic mean free path
$W$	Dipole transition probability
$\langle \Phi_f  ,   \Phi_i \rangle$	Final and initial state wave function
$H^{int}$	Perturbation from the incident light
$\sigma$	Photon polarization
$\mathbf{A}$	External electric field of incident photons
$\mathbf{p}$	Momentum operator
$  Y_{l,m_l}(\Theta, \phi) \rangle$	Spherical harmonics
$  X(s) \rangle$	Spin wave function
$c$	Speed of light
$m$	Invariant mass
$J$	Total angular momentum
$L$	Orbital angular momentum
$\mathbf{M}$	Magnetization direction
$m_{Orb,Spin}$	Orbital and spin magnetic moment
$\mu^{+/-}$	Magnetic polarization
$P_C$	Polarization factor
$\langle T_Z \rangle$	Magnetic dipole operator
$f$	Frequency
$\vec{M}$	Magnetic moment per volume
$\vec{B}$	Magnetic flux density
$\nu$	Poisson coefficient
$\mu_B$	Bohr's magneton
$M_{Sat}$	Saturation magnetization

# **Part I**

## **Theoretical Background**



# CHAPTER 1

---

## Introduction

---

The imminent end of Moore's law asks for alternative materials and technologies in order to overcome the physical limits of silicon-based memory and logic devices. A promising candidate, which might pave the way towards next-generation electronic devices, is the material class of *transition metal oxides* (TMO), exhibiting insulating and metallic states, piezoelectricity, superconductivity and different magnetic ordering [1–3]. Especially, the cross coupling of electric and magnetic properties like magnetoresistance, magnetocapacitance, and multiferroics offers a new potential for electronic devices. TMOs exhibit a great multitude of chemical, structural and physical properties, which can be altered by subtle distortions of the coordination environments, changes in composition, temperature and external electric fields. This is certainly the case for TMOs in a perovskite  $ABO_3$  structure. In particular, the application of an electric field has been reported to provide a reversible switching between two or multiple states [4], which has attracted enormous scientific and technological interest.

In TMOs, the variety of properties stems from the complex relation between the cationic  $d$ -electron configuration and their corresponding crystal structure [5]. At the same time the ionic and/or covalent metal-oxygen bond as well as the configuration of oxygen ions surrounding each metal ion has profound effects on the structure and stability of the respective TMO [1]. Typically, the metal cations are bound by four or six surrounding oxygen anions, which leads to tetrahedral or octahedral environments. Depending on the particular block-by-block stacking of the respective oxygen coordination either the perovskite or the brownmillerite  $ABO_{2.5}$  structure is formed. Due to the prevalent orbital anisotropy of the  $d$  shell spin states, the exchange interaction of electrons is considerably coupled to the lattice geometry and supports a

multitude of configurations with often rather small energy differences [6, 7]. Moreover, transition metals can appear in multiple oxidation states enabling an electron transfer between those different cationic valencies, which also stabilize a variety of magnetic states [8].

Among transition metal oxides, special attention is paid to the mixed-valence  $\text{La}_{0.7}\text{Sr}_{0.3}\text{MnO}_{3-\delta}$ , a half-metallic, complex magnetic oxide, which exhibits a large spin polarization ( $\sim 95\%$ ) and the highest Curie temperature of  $T_C = 370\text{ K}$  known for the group of manganites [9, 10]. Further, a *magnetoresistance* (MR) proportion of larger than  $\sim 1800\%$  has been reported [10, 11], and has been widely used in magnetic oxide tunnel junction-based devices with effective spin injection behavior. As an extensively investigated magnetoelectric material LSMO has been subject of numerous studies revealing ME coupling via strain [12, 13], charge carrier doping [14] and interfacial exchange processes [15].

The strong correlation of physical properties with the electronic- and atomic structure is accompanied by a considerable sensitivity for any kind of ionic crystal defects. Common ionic point defects in complex oxides are oxygen vacancies. In contrast to oxygen ions, oxygen vacancies are positively charged and do increase the volume of the crystal lattice [7]. In order to compensate the resulting charge disparity and the crystalline stress, the valence state of the respective transition metals as well as the bonding length and angle of the metal-oxygen bond adjust. By exceeding a certain concentration of oxygen vacancies also superstructures can be formed, exhibiting new physical properties. However, in order to bridge the gap towards future electronic devices, the formation and dynamics of oxygen vacancies within a TMO can be substantially controlled by strain [16], temperature [17] and external electric fields [18] providing an active manipulation of the prevalent physical states [19].

Recently, the field of magneto-ionics received increased attention as the voltage-driven chemical intercalation of ionic species opened a novel route towards the control of magnetism in bulk materials. One of the first studies reported about the migration of oxygen vacancies in magnetic Fe-O/Fe layers contacted with ionic liquid electrolytes, which profoundly modulated near-surface and bulk magnetism [20]. In the scope of magnetic oxides, electrolyte-gated LSMO devices showed a substantial formation and annihilation of oxygen vacancies affecting magnetic bulk properties (20 nm) [21] and providing switching capabilities for large sample areas with large spatial homogeneity and high switching speed [22].

Beyond ionic electrolyte gating also solid-solid devices exhibit promising magneto-ionic effects. It has been shown that the use of strongly reducing films as a capping layer on LSMO induces significant oxygen migration and enables the control of magnetic properties. A subsequent long-time exposure to atmospheric oxygen can restore the pristine state of LSMO and oxygen vacancies as induced by reducing capping layers are refilled with oxygen atoms [23].

Recently, a combined resistive switching experiment with a structural monitoring utilizing *in situ transmission electron microscopy* (TEM), revealed a reversible phase transition from a half-metallic and *perovskite* (PV) structure into an insulating and *brownmillerite* (BM) state [24]. Moreover, an annealing study in vacuum demonstrated a topotactic phase transition from BM to PV accompanied by a magnetic transition from antiferromagnetic- to a ferromagnetic ordering, and an insulator-to-metal transition [25].

The prevalent multi-phase transition capabilities in LSMO open up valuable potentials for future non-volatile memristive devices. Although, there are a vast of reports about electric field-induced chemical and physical changes in LSMO, the driving mechanism is not completely understood and asks for further investigations utilizing advanced combined probing techniques.

In this thesis, we employ local conductivity atomic force microscopy and X-ray photoemission electron microscopy to investigate the correlation of magnetic and chemical information of electrically modified areas of LSMO thin films on a niobium doped SrTiO<sub>3</sub> (001) (Nb:STO) substrate. Our data demonstrate a voltage-driven change of the Mn ion valency accompanied by a metal-to-insulator transition and a loss of magnetic ordering. The strength of the underlying microscale redox processes can be tuned by the voltage amplitude and is reflected by significant spectral variations of the Mn L<sub>3,2</sub> and the O K absorption edges.

The first part of the thesis deals with the fundamental background of resistive switching in complex oxides (**Ch. 2**), general properties of lanthanum manganites (**Ch. 3**) and the working principles of both PES and PEEM (**Ch. 4**).

The second part introduces the utilized sample fabrication process by PLD and accompanying monitoring tool, i.e. *in situ* high-pressure RHEED providing an epitaxial layer-by-layer growth of single crystalline thin films (**Ch. 5**). A brief description of subsequent morphological AFM, structural XRD and magnetic sample characterization methods VSM is given in **Ch. 6**.

This is followed by the discussion of the results in the third part.

In **Ch. 7** the growth and the subsequent characterization of La<sub>0.7</sub>Sr<sub>0.3</sub>MnO<sub>3</sub> thin films is presented. Here, special attention is paid to the investigation of the electronic structure by means of HAXPES and a detailed magnetic characterization combining bulk-sensitive VSM- and surface-sensitive and element-selective XMCD measurements.

As a next step, a modulation of the LSMO resistance is performed by the application of a voltage to the thin film surface in **Ch. 8**. In particular, the observations of the resulting electronic properties in ambient atmosphere and in vacuum are discussed in more detail. A subsequent PEEM study of electrically modulated microscale sized areas reveals spectroscopical fingerprints indicating a variety of chemical and physical changes of electronic and magnetic properties.

Conclusions and outlook are drawn in **Ch. 9**.



---

### Resistive Switching in Complex Oxides

---

In the following, a brief overview of *resistive switching* (RS) phenomena is presented, focusing on concepts relevant in this thesis. Basic definitions of nanoionic redox-based resistive switching elements and their main operation modes will be given. In particular, the formation of oxygen vacancies and the corresponding *valence change model* (VCM) will be discussed.

#### **2.1 Introduction and Resistive Switching Mechanisms**

Resistive switching describes a reversible and hysteretic modulation of the resistivity of a thin film device upon electrical stimuli. The application as memory requires a sufficiently long retention time after the electrical stimulus has been released (nonvolatility) [26]. Empirically, the change of the resistance comes along with a modulation of an internal state of the respective switching material. In the framework of this thesis, we discuss resistive switching mechanisms driven by nanoionic redox phenomena. This means a change of the internal state of a device by ion migration and diffusion, chemical reactions, and/or local temperature increase. Materials or devices showing this particular resistive switching behaviour are called *resistive switching random access memory* (ReRAM). A material class of great interest, which belongs to the investigation of ReRAMs concerns transition metal oxides. TMOs are binary or ternary oxide compounds of transition metals, which reveal partially filled valence bands resulting in interesting effects such as resistive switching [26]. The device operation of ReRAMs can be realized by periodic *voltage sweeps* (Fig. 2.1) or *voltage pulse* excitations. Although the pulse mode is the most

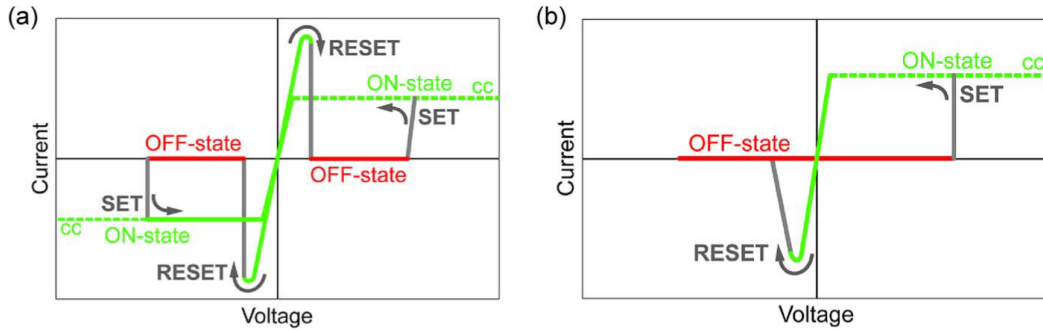


**Figure 2.1:** I-V curves of the most common types of nonvolatile ReRAM cells based on transition metal oxides. (a) Bipolar resistive switching (BRS) depends on the polarity of the applied voltage. (b) Unipolar resistive switching (URS) only depends on the amplitude of the applied voltage. Image taken from [27].

common one for device applications, the I-V sweep mode reveals characteristic information about the respective switching process such as the threshold voltage  $V_{th}$ , indicating the metal-to-insulator transition. A ReRAM cell can be resistively switched into a *high resistance state* (HRS) or *OFF state* and *low resistance state* (LRS) or *ON state*. The *write* process from the HRS to the LRS indicates the *SET* operation and the way back from LRS to HRS is known as *RESET*. The *read* voltage  $V_{rd}$  probes the respective resistive state after a switching event. Commonly, the magnitude of  $V_{rd}$  is significantly smaller than the writing voltage  $V_{wr}$  to avoid a measurable change of the state. Most of the devices known, need initially a high voltage pulse/cycle in order to bring the untreated samples into their first write/read operation. This process is called *electroforming* [26].

**Bipolar Resistive Switching** Most of the reported ReRAM devices are operated in the *bipolar resistive switching* (BRS) mode Fig. 2.1 (a). Here, the switching direction depends on the polarity of the write voltage. Consequently, the SET process is caused by one polarity, whereas the RESET occurs at the opposite polarity. Often, a *current compliance* (cc) during the SET process provides a protection against possible dielectric breakdowns [26].

**Unipolar Resistive Switching** *Unipolar resistive switching* (URS) describes a device operation in which the SET, RESET, and read operations can be performed with solely one voltage polarity (Fig. 2.1 (b)). Starting in a high resistance state a SET Voltage  $V_{SET}$ , which is larger than  $V_{th1}$ , brings the system into the LRS, which is preserved by a current compliance. Switching the device into the HRS again requires a RESET voltage  $V_{RES}$ , which overcomes  $V_{th2}$ . Here, the cc has to be released or sufficiently decreased to provide a switching into the HRS of the memory device [26].

In the scope of this work, so far, the relevant operation modes of typical TMO based ReRAM cells have been discussed. Now, we focus on the device geometry and the localization of the switching events within the cell. Commonly, oxide-based ReRAMs are realized in *metal-insulator-metal* (MIM) structures Fig. 2.2. Often these MIM structures define a vertically arranged stack of metal electrodes (M) and a functional/insulating layer (I) in between. In general, one can distinguish between two categories of the location, in which the resistive switching event occurs: the vertical and the lateral direction. The vertical direction describes the path between the two electrodes M-M through the sandwiched layer I. Here, the switching event can occur along the entire path between the electrode interfaces, at one of the interfaces, or at the center between the electrodes.

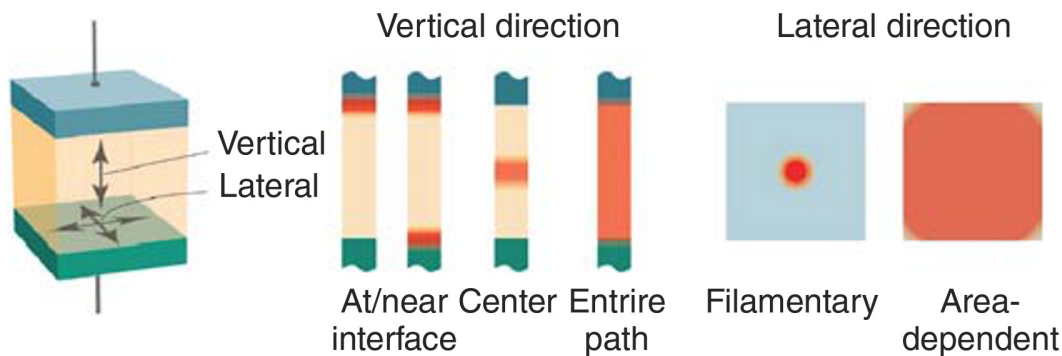


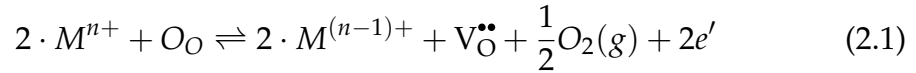
**Figure 2.2:** Geometrical localization of the switching mechanism in a MIM stack. In the vertical direction one can distinguish between switching events at the interface, in the center of the device, or along the entire path between the top and bottom electrode. The lateral direction is separated into a filamentary switching (single or multiple conducting filaments) and into an area-dependent switching mechanism. Image taken from [26].

The lateral direction switching is divided into the *filamentary switching* and the *area-proportional switching*. The aforementioned filamentary switching describes the formation or rupture of a single *conducting filament* (CF) in the nanometer scale present in many resistive switching devices [26]. Nevertheless, also the formation of multiple filament switching is known [28]. In the case of the area switching the entire cross section takes part in the switching event. Thus, the evolution of the current is proportional to the respective cross-sectional area. Intermediate cases have been reported, so that switching areas occur as extended spots instead of spreading over the entire cross section [29]. Due to the fact that this switching type is mostly situated close to the interface, it is also called *interface switching* [26]. The switching events in devices showing bipolar behaviour usually are localized near one of the interfaces (vertical) and also form CFs (lateral).

The following section addresses the underlying physics and chemistry of the resistive switching process. In particular, we concentrate on the VCM, which is the relevant model describing the resistive switching process in  $\text{La}_{0.7}\text{Sr}_{0.3}\text{MnO}_3$ .

## 2.2 Valence Change Model

The basic concept of the valence change mechanism comes along with a local redistribution of oxygen vacancies and the subsequent redox reaction in the cation sublattice [30–32]. Oxygen vacancies can be formed and moved under the application of large electric fields or elevated temperatures. Within the metal oxide matrix oxygen vacancies can be seen as crystallographic point defects, which can be described in the Kröger-Vink notation [33]  $M_S^C$ .  $M$  indicates the type of defect (e.g.  $V$  for vacancy),  $S$  denotes the respective lattice site, and the charge state is expressed by  $C$  ( $C, \bullet = +, ' = -$ ). Consequently, an oxygen vacancy follows the notation:  $V_{\text{O}}^{\bullet\bullet}$ . An increase of the oxygen vacancy concentration leads to n-doping of the respective material, resulting in an energy shift of the Fermi level  $E_F$  into the conduction band. Electrons which have been previously located at the oxygen site are now transferred to the metal atom in order to compensate the charge disparity. This charge transfer process results in a reduced valence state of the transition metal atom (e.g.  $\text{Mn}^{3+} \rightarrow \text{Mn}^{2+}$ ). Accordingly, the underlying redox process can be described as in Eq. 2.1:



Obviously, the redox reaction includes the formation of molecular oxygen as a byproduct. Actually, the formation of gas bubbles right under the metal electrodes of MIM structures have been reported several times [34–36]. Besides the evolution of oxygen gas it is also likely that the material of or nearby the anode may be oxidized [37].

The valence change model explains the relation between migration of oxygen vacancies and the resulting valence change of the cations, which influences the electronic states and leads to a local change in resistivity. The cationic valence change can have profound effects on the local conductivity and the electron transport properties. For instance, in materials, where the conductivity is mediated mostly by an exchange interaction like superexchange or double-exchange, the occupation of the outermost  $3d$  shell of the cation is essentially determining a metal or insulating phase [38]. Alternatively, a modulated oxygen concentration at the metal/insulator interface can alter the electrostatic barrier height (Schottky effect), which is the origin of the non-linear electronic I-V response commonly observed in bipolar switching materials [26, 31]. Here, also thermally accelerated diffusion of oxygen vacancies due to significant

Joule heating may play a significant role in selected materials [39].

In order to realize ReRAMs of the bipolar switching type, typically asymmetric electrode configurations (high and low work function materials) are used. In this context, it is worth mentioning that the oxygen affinity or permeability of the electrode material is highly relevant in this type of switching process: the oxygen can be blocked or gettered, stored within or passed through the electrode [40].

Moreover, lateral inhomogeneities often lead to highly localized filaments exhibiting low or high resistivity. Also along the vertical direction the switching events in the ReRAM cells are usually confined for instance to the functional layer/electrode interface [41].

## 2.3 Electronic Transport Across Metal/Insulator Interfaces

There are several mechanisms, which can be attributed to the electron transport in MIM devices. On the one hand, there are intrinsic properties of the functional layer, e.g. trap density, trap spacing, trap level, carrier drift mobility, dielectric relaxation time and the density of states in the conduction band [42, 43]. On the other hand, the electronic properties of the dielectric-electrode interfaces, like the barrier height or the charge carrier density, have a strong influence on the conductivity of the whole device. The Schottky effect describes the evolution of a contact potential between a metal and a semiconductor. The work function difference between the metal  $\Phi_M$  and the oxide layer, described by an n/p-type semiconductor  $\Phi_S$ , causes a potential barrier, which can be referred to the formation of a depletion region near the interface, in which the density of mobile electrons is decreased (Fig. 2.3).  $\Phi_M$  is the energy required to promote an electron from the Fermi level of the metal to the vacuum level. Furthermore, the work function of a metal consists of a bulk contribution due to the periodic potential of the crystal lattice and it contains also a surface contribution due to a possible dipole layer at the surface.  $\Phi_S$  is a variable quantity because the Fermi level varies with the doping [44]. An electron transfer between the metal and the semiconductor leads to a band bending  $E_{CB}(x)$  in the manner that both Fermi levels get aligned in order to balance uncompensated donor/acceptor ions in the semiconductor.

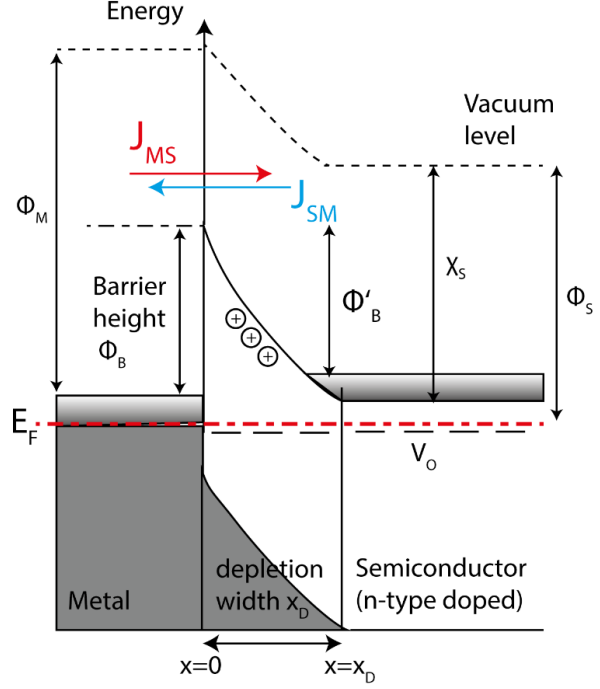
The barrier height  $\Phi_B$  can be deduced from the Schottky-Mott rule, which includes the vacuum work function of the metal  $\Phi_M$  and the electron affinity  $\chi_S$  of the semiconductor:

$$\Phi_B = \Phi_M + \chi_S, \quad (2.2)$$

while  $\chi_S$  is defined as the energy difference between the lower edge of the conduction band and the vacuum energy level.

Oxygen-deficient oxides can be described as n-type semiconductors. Here, the shape of the potential barrier is defined by the donor density  $N_D$  in

**Figure 2.3:** Energy band diagram of a metal/n-type oxide junction. Two electron currents, indicated by  $J_{MS}$  and  $J_{SM}$ , provide a compensation of an interfacial charge imbalance. Thus, the Fermi levels of both materials get aligned. If the barrier height  $\Phi_B$  is larger than the electron affinity  $\chi_S$ , electrons are transferred from the oxide to the metal. This process comes along with a formation of a depletion region  $x_D$ , which is determined by the respective oxygen vacancy concentration in the oxide. Image taken from [45].



the depletion region  $x_D$ . In order to find an approximated mathematical expression for both the depletion region and the conduction band offset  $E_{CB}(x)$  within the depletion region, several assumptions have to be implemented: space charge regions in the metal can be neglected, shallow donors within the depletion region are assumed to be fully ionized at room temperature, and a constant charge density  $N_D$  in the semiconductor is assumed. From this, a linear electric field  $E = \frac{e \cdot N_D \cdot x}{\epsilon_S}$  can be derived, where  $e$  denotes the electron charge,  $x$  is the distance from the interface and  $\epsilon_S$  indicates the dielectric constant of the vacancy-doped oxide. Consequently, the width of the depletion region  $x_d$  and the conduction band offset  $E_{CB}(x)$  can be calculated as follows:

$$x_d = \sqrt{\frac{2 \cdot \epsilon_S \cdot (\Phi_B - V_a)}{e \cdot N_D}} \quad (2.3)$$

$$E_{CB}(x) = \Phi_B - \frac{e \cdot N_D}{2\epsilon_S} \cdot x^2, \quad (2.4)$$

where  $V_a$  indicates an externally applied voltage. The compensating current flow between metal and semiconductor in both directions is described by a classical and a quantum mechanical transport process. In the following the *Thermionic Emission* (TE) and the *Field Emission* (FE) will be discussed, respectively.

**Thermionic Emission** The thermionic emission, also associated with *Schottky Emission*, represents the classical transport, in which thermally activated

electrons overcome the potential barrier into the conduction band of the respective oxide [46]. Here, the injected electrons have to have a kinetic energy above the barrier height  $E > E_F + \Phi_B$ . This thermally driven emission process is widely observed in oxides [47].

The analytical expression for the current density in the TE  $J_{SE}$  can be related to the electric field ( $E$ ) and the temperature ( $T$ ) [48]:

$$J_{TE} = A^{**} \cdot T^2 \cdot \exp\left[\frac{-e \cdot \Phi_B}{k_B T}\right] \cdot \left(\exp\left[\frac{-e \cdot V_F}{k_B T}\right] - 1\right). \quad (2.5)$$

Here,  $A^{**}$  indicates the effective Richardson constant,  $k_B$  denotes the Boltzmann's constant,  $T$  is the absolute temperature, and  $V_F$  is the applied forward bias. This model can be used if the linear dimension of the depletion layer  $x_d$  is much larger than the electrons' de Broglie-wavelength  $\lambda$ .

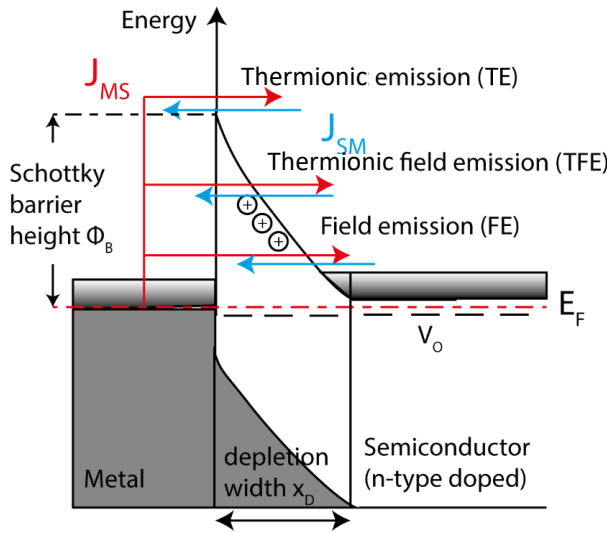


**Figure 2.4:** Energy band diagram showing qualitatively possible electron transport mechanisms over a metal-semiconductor (n-type) barrier. Thermionic emission describes a classical transport over the potential barrier of thermally activated electrons. Under the application of large electric fields, the field emission process, provides a tunneling transport channel through the space charge region near the Fermi level. The thermionic field emission combines both TE and FE. Image taken from [45].

**Field Emission** The quadratic band bending at the metal-semiconductor junction or space charge region leads to different tunneling probabilities for the respective electrons. For thermally excited electrons the tunneling probability is significantly enhanced due to the thinner space charge region at the top. At the bottom, near the Fermi level, the barrier width  $x_D$  is much thicker. Here, a probable tunneling channel can be established only by the application of large electric fields. The external electric field modifies both the barrier height  $\Phi_B$  and the barrier width  $x_D$ . The field emission is the dominant tunneling process observed in thicker oxides [47, 49]. Eq. 2.6 gives the mathematical expression of the current density under the application of an electric field [48]:

$$J_{FE} = \frac{A^{**} \cdot T \cdot \pi \cdot \exp[-e \cdot (\Phi_B - V_F)/E]}{c_1 \cdot k_B \cdot \sin(\pi \cdot c_1 \cdot k_B T)} \quad (2.6)$$

where

$$E = \frac{e \cdot h}{2} \cdot \sqrt{\frac{N_D}{m^* \cdot \epsilon}}$$

$$c_1 = \frac{1}{E} \log \left[ \frac{4(\Phi_B - V_F)}{\Phi_n} \right]$$

In case of thinner films  $d < 3$  nm the *direct* tunneling process is observed [50], which can be approximated to Eq. 2.7 [47]:

$$J_{DT} \approx \exp \left\{ \frac{-8\pi\sqrt{2}e}{3h} (m^* \Phi_B)^{1/2} \kappa \cdot t_{Ox,eq} \right\}, \quad (2.7)$$

while  $\kappa$  indicates the relative dielectric constant of the oxide layer and  $t_{Ox,eq}$  denotes the equivalent oxide thickness.

**Thermionic-Field Emission** While the FE describes a pure tunneling process, the *thermionic-field emission* (TFE) is determined by a tunneling process of thermally excited charge carriers facing a thinner potential barrier than in the FE case. Due to the combination of TE and FE, TFE is located at an energy between them (Fig. 2.4). If the thermal energy  $k_B T$  and  $E$  are roughly the same TFE becomes the dominant process. The respective current density, under forward bias, can be expressed as

$$J_{TFE} = \frac{A^{**} \cdot T \sqrt{\pi \cdot E \cdot e \cdot (\Phi_B - \Phi_n - V_F)}}{k \cdot \cosh(E/k_B \cdot T)} \cdot \exp \left[ \frac{-e \cdot \Phi_n}{k_B \cdot T} - \frac{e \cdot (\Phi_B - \Phi_n)}{E_0} \right] \exp \left( \frac{e \cdot V_F}{E_0} \right), \quad (2.8)$$

$$\text{with } E_0 = E \cdot \coth \left( \frac{E}{k_B \cdot T} \right).$$

Finally, there is a strong dependence of the respective transport process and the barrier thickness or space charge region  $x_D$ . In turn, the barrier width depends on the donor density  $N_D$ . Thus, it becomes clear that the oxygen distribution at the metal-oxide interface has a profound effect on the resistivity. Thin barriers can be realized by high doping concentrations (tunnel process), which result in the LRS. Low doping concentrations lead to a thick barrier width (classical drift) leading to the HRS.

---

## Properties of Lanthanum Manganites

---

The following chapter discusses the fundamental aspects of the most important mechanisms driving the properties of manganites, and in particular of  $\text{La}_{0.7}\text{Sr}_{0.3}\text{MnO}_3$ . After a brief historical background of manganites, a selection of essential topics relevant for this thesis will be given, i.e. crystal and electronic structure, magnetic structure, and electronic transport.

### 3.1 Introduction

Since several decades rare earth perovskite manganese oxides of the composition  $\text{A}_{1-x}\text{B}_x\text{MnO}_3$  are of great interest, where A and B denote trivalent (rare earth: e.g. La, Nd, Pr, Sm) and bivalent (alkaline earth: e.g. Sr, Ca, Ba, Pb) cations, respectively. Phenomena like the *paramagnetic* (PM) to *ferromagnetic* (FM) transition at the Curie temperature  $T_C$  and the concurrent metal-insulator transition (MIT) in manganites are well-known since several decades [51–54]. The renewed focus on the material class of manganites originates from the discovery of the *Colossal Magneto Resistance* (CMR) [55, 56], which describes a significant increase of the resistivity in the vicinity of the Curie temperature  $T_C$  within a strong external magnetic field. 35 years before the discovery, the CMR effect has been theoretically predicted on the basis of the *double exchange interaction* (DE) model [57–59]. The DE mechanism is driven by an electron hopping process between  $\text{Mn}^{3+}$  and  $\text{Mn}^{4+}$  cations via an oxygen anion and gives good explanation for the physical behaviour of manganites with a stoichiometry of  $\text{La}_{1-x}\text{Sr}_x\text{MnO}_3$  within a doping range of  $0.17 \leq x \leq 0.3$ . Apart from CMR, perovskite manganites such as LSMO exhibit a rich phase

diagram, which consists of a wide range of magnetic properties and phenomena like charge and orbital ordering, and electronic phase separation [55, 60]. This originates from a sensitive interplay of charge, spin, lattice, and orbital degrees of freedom, which results in a tunability of the respective electronic transport and magnetic properties. The interesting physical and chemical behaviour of transition metal oxides can be referred to the unique nature of the outer d-electrons and the intermixing of ionic and covalent metal-oxygen bonds. Multifunctional materials have attracted increasing attention due to their application potential in data storage devices [61, 62]. There is only a rare selection of naturally existing oxides, which show both ferromagnetic and ferroelectric behaviour. A prominent representative multiferroic material is BaTiO<sub>3</sub> [63].

In recent years, also La<sub>0.7</sub>Sr<sub>0.3</sub>MnO<sub>3</sub> has been attracted increasing interest, not only due to its resistive switching properties [64], but also due to its relevance as a model system in fundamental physics [65]. In the following, the crystal and electronic structure of La<sub>1-x</sub>Sr<sub>x</sub>MnO<sub>3</sub> are presented. Moreover, the magnetic structure and the respective interaction mechanisms will be discussed in more detail.

## 3.2 Crystal- and Electronic Structure

Manganites like La<sub>0.7</sub>Sr<sub>0.3</sub>MnO<sub>3</sub> crystallize in modifications of the perovskite structure as it is depicted in Fig. 3.3. An essential feature of the ABO<sub>3</sub> structure is the oxygen octahedron located around the centered B site Mn cation. The A sites are occupied by the trivalent rare earth atoms La<sup>3+</sup> and the bivalent alkaline earth metal Sr<sup>2+</sup>. In order to preserve the perovskite structure, the

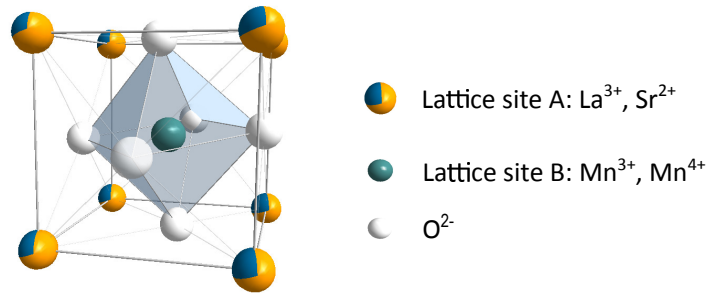


**Figure 3.1:** La<sub>1-x</sub>Sr<sub>x</sub>MnO<sub>3</sub>: Schematic description of the perovskite structure.

ratio of the bond lengths between the A site lattice point and the oxygen,  $d_{A,O}$ , and the B site and the oxygen,  $d_{B,O}$ , has to amount to  $\frac{d_{A,O}}{d_{B,O}} = \sqrt{2}$ . Actually, slight deviations already lead to a strain of the crystal lattice. A simplified quantity of the strain is given by the *Goldschmidt tolerance factor*  $T$  [66]:

$$T = \frac{1}{\sqrt{2}} \cdot \frac{d_{A,O}}{d_{B,O}} \approx \frac{1}{\sqrt{2}} \cdot \frac{\langle r_A \rangle + r_O}{\langle r_B \rangle + r_O}. \quad (3.1)$$

Here,  $\langle r_{A,B} \rangle$  and  $r_O$  denote the radii of the A site cation and the oxygen anion, respectively. An ideal perovskite structure reveals a tolerance factor of  $T=1$ . Further, values in the range of  $0.75 < T < 1$  describe stable states [67]. Arising tensions of the crystal lattice can be compensated or at least reduced by a tilt or torsion of the  $\text{MnO}_6$  octahedron. This comes along with a change of the Mn-O bond angle, which can have profound effects on the magnetic and electronic transport properties. The decrease of the Mn-O bond length can provoke a transition from a ferromagnetic and conductive state into a ferromagnetic and insulating phase (Fig. 3.2). The diagram in Fig. 3.2 illustrates the magnetic ordering temperature as the function of the tolerance factor [68]. It seems that the tolerance factor determines both the

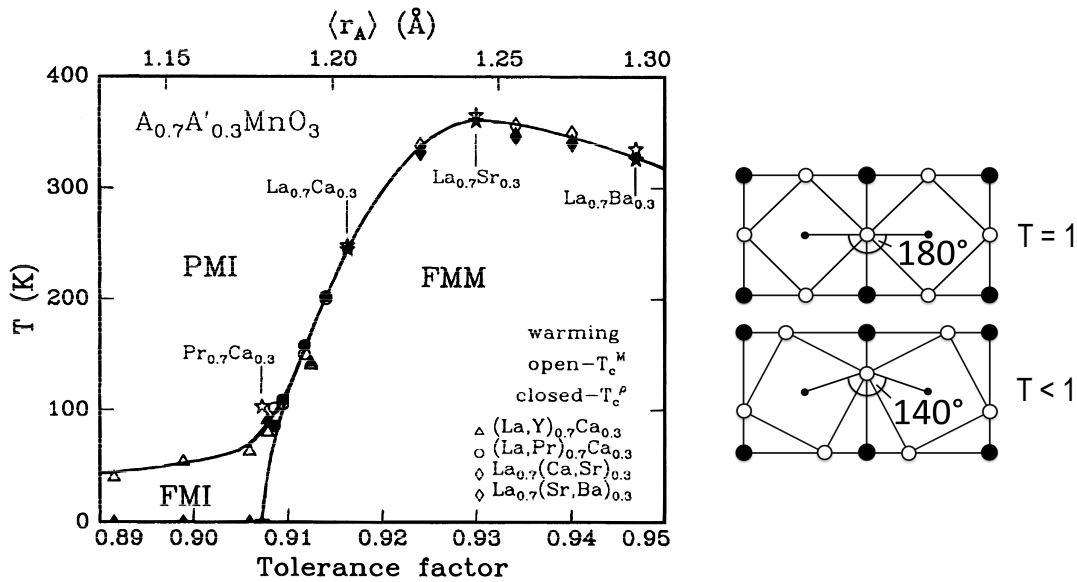


**Figure 3.2:** As a result of the interplay between the temperature and the tolerance factor there is a rich phase diagram consisting of paramagnetic and insulating (PMI)-, ferromagnetic and insulating (FMI)-, and ferromagnetic and metallic (FMM) phases. The symbols label the phase transition temperature as a function of the tolerance factor (Image taken from [68]). The right sketch illustrates a comparison of a tilted oxygen octahedron with a tolerance factor  $T < 1$  and a non distorted structure. Here, the filled circles indicate the A site cations, whereas the non-filled circles denote the oxygen anions. The small filled circles can be identified with the manganese cations. The Mn-O-Mn bond angle decreases with a decreasing tolerance factor. Image taken from [69].

transition temperature of the magnetic ordering and the electronic ground state (metal or semiconductor). But in fact, there are experimental studies on  $\text{La}_{0.7}\text{Ca}_{0.11}\text{Sr}_{0.19}\text{MnO}_3$  and  $\text{La}_{0.32}\text{Pr}_{0.38}\text{Sr}_{0.30}\text{MnO}_3$  showing that also the varying occupation and varying distribution of the cationic sites may modify the Curie temperature up to 100 K [70, 71], as well as the metal-to-insulator transition [71]. Moreover, there are indications that the physical properties are also correlated to the disorder of the cationic lattice sites, which can be

expressed by Eq. 3.2

$$\sigma^2 = \langle r_A^2 \rangle - \langle r_A \rangle^2. \quad (3.2)$$

In case of  $\text{La}_{0.7}\text{Sr}_{0.3}\text{MnO}_3$  the doping concentration  $x$  also modifies the bond length due to the fact that  $\text{Mn}^{4+}$  cations are smaller than  $\text{Mn}^{3+}$  cations [13, 72].

### 3.2.1 Jahn-Teller-Effect

In the parental compound  $\text{LaMnO}_3$  the Mn cation exhibits the electronic configuration  $[\text{Ar}] 3d^4$ , where the  $3d$  spin states are degenerated. In the picture of a free ion, each electron has the same free energy. In the surrounding of a crystal field these degenerated states split up into two different energy levels. Basically, the crystal field is determined by the Coulomb repulsion of the oxygen ions within the oxygen octahedron.

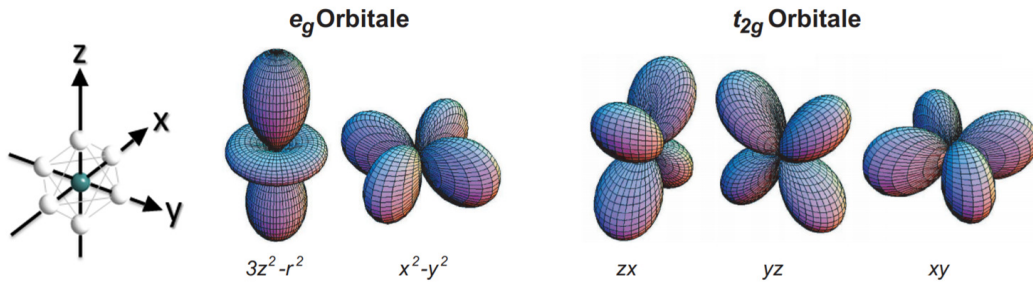
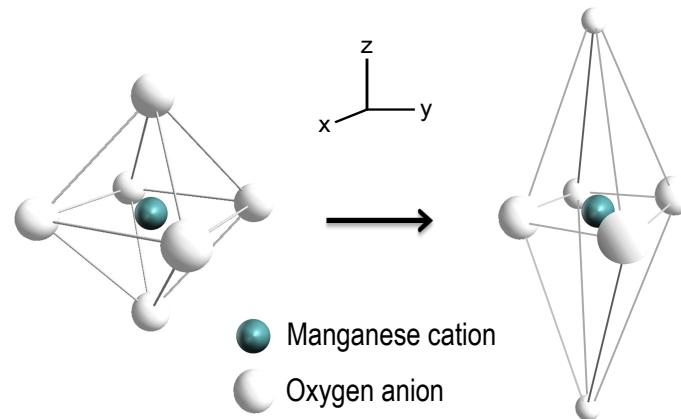


Figure 3.3: Schematic description of crystal field split  $3d$  orbitals [73].

In the sketch of Fig. 3.3 the positions of the  $\text{O}^{2-}$  anions are aligned with the coordinate axes. A Mn  $3d$  electron pointing towards the direction of an oxygen anion exhibits a larger energy (due to Coulomb repulsion) with respect to an electron, which is located in between the ligands. From this consideration, it is apparent that the  $d_{x^2-y^2}$  and  $d_{x^2}$  orbitals represent the high energy levels. In an octahedral coordination both orbitals are equivalent and contribute to the *e<sub>g</sub>* orbital. Electrons located in  $d_{xy}$ ,  $d_{xz}$ , and  $d_{yz}$  orbitals show a lower probability density in the vicinity of the O  $2p$  orbitals, which leads to a lower energy level. Again, these electron spin states are energetically degenerate and form the *t<sub>2g</sub>*-orbitals [74]. In an octahedral environment, first the *t<sub>2g</sub>*-orbitals and then the *e<sub>g</sub>* orbitals will be occupied by electrons, according to Hund's rules. A distortion of the crystal lattice, for instance, due to an interfacial strain effect, causes a further splitting of the degenerated states forming the *t<sub>2g</sub>* and *e<sub>g</sub>* orbitals. The lifting of the degeneracy of these electron spin states is called *Jahn-Teller-Effect* (JTE) [75]. A possible distortion of the crystal lattice could be an elongation of the oxygen octahedron along the  $z$ -axis of about  $2\delta$ , which at the same time describes a compression of  $\delta$  along the  $x$ - and  $y$ -axis, as it can be seen in Fig. 3.4. The gain of electrostatic energy is linear with  $\delta$ , while the



**Figure 3.4:** Distortion of the octahedral crystal lattice due to the Jahn-Teller-Effect.

energy loss due to restoring elastic forces in the crystal increases with  $\delta^2$  [76]. Essentially, this results in several energy minima leading to thermal and quantum mechanical transitions, which is also summarized in the *dynamic Jahn-Teller-Effect*. For a large enough number of JT-ions they sum up to a cumulative effect, in which the lattice distortion effectively leads to remarkable phase transitions [76].

Figure 3.5 represents the electronic structure of an JT energy split  $\text{Mn}^{3+}$  cation in the  $\text{LaMnO}_3$  compound, which shows an elongation of the  $\text{MnO}_6$  octahedron. Here, the  $e_g$  electron occupies the  $3d_{z^2}$  orbital. The explanation of the JT energy splitting is analog to the crystal field splitting. An elongation along the  $z$  direction reduces the repulsive Coulomb interaction force between the  $\text{O}^{2-}$  and the  $d_{z^2}$  orbital leading to a lowering of the respective energy level. Conversely, a compression of the octahedron in the  $x$ - $y$ -level increases the energy of an electron located in the  $d_{x^2-y^2}$  due to an increased Coulomb repulsion.

The diagram in Figure 3.5 displays a simplified model of the energy splitting.

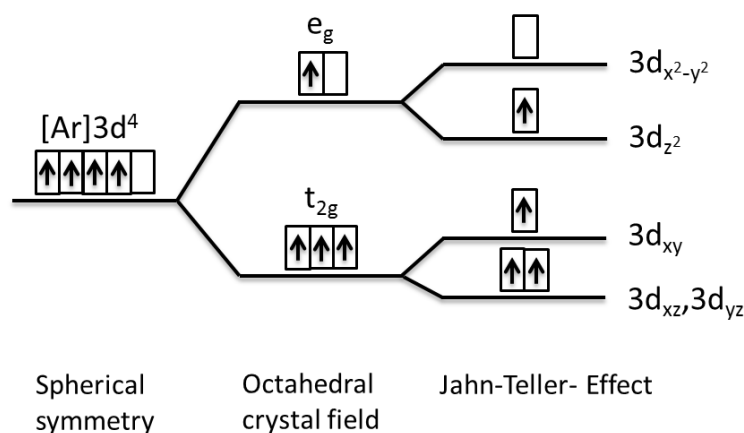


**Figure 3.5:** Orbital energy splitting caused by the crystal field and the Jahn-Teller-Effect.

It considers the crystal field and the JT-splitting, but not the energy gain resulting from the covalent bonding, which in fact, shows a remarkable effect and cannot be neglected [77]. In particular, it finds its relevance in the magnetic exchange interaction (Sect. 3.3).

An interesting question arises, when  $\text{LaMnO}_3$  gets hole doped for instance with  $\text{Sr}^{2+}$  cations. Due to the missing orbital degeneracy,  $\text{Mn}^{4+}$  does not belong to the group of JT-ions. However, the cooperative distortion of the surrounding forces the oxygen octahedron around the  $\text{Mn}^{4+}$  to adopt the distortion. Thus, an according energy splitting of the  $d$  orbitals is expected.

### 3.3 Magnetic Structure

As it is already mentioned in Sect. 3.2 manganites of the composition  $\text{A}_{1-x}\text{B}_x\text{MnO}_3$  feature a rich phase diagram, which also shows varying magnetic phases in dependence of doping concentration and temperature. For instance,  $\text{LaMnO}_3$  is an antiferromagnet. Its magnetic structure comprises an alternating sequence of ferromagnetic layers, which are antiferromagnetically coupled (Fig. 3.6). The magnetic structure has been verified by neutron scattering experiments [78–80]. A Sr doping of  $\text{LaMnO}_3$  between  $x \approx 0.15$  and  $x \approx 0.4$  results in ferromagnetic ordering [81]. Pure  $\text{SrMnO}_3$ , in turn shows an antiferromagnetic ordering, in which the neighbouring magnetic moments are aligned antiparallel to each other. Finally, in complex manganites there is the tendency to assemble in a magnetic ground state.

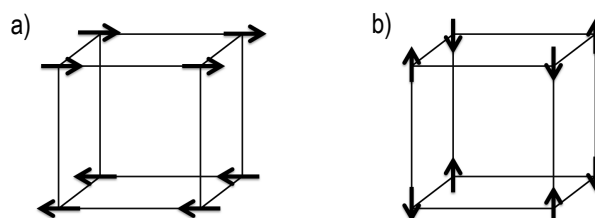


**Figure 3.6:** Antiferromagnetic ordering of (a)  $\text{LaMnO}_3$  and (b)  $\text{SrMnO}_3$ . Adapted from [69].

#### 3.3.1 Magnetic Moment in $\text{La}_{1-x}\text{Sr}_x\text{MnO}_3$

The resulting magnetic moment of  $\text{La}^{3+}$ ,  $\text{Sr}^{2+}$  and  $\text{O}^{2-}$  ions amounts to zero (except of small diamagnetic contributions), due to their electronic configuration of a noble gas [82]. The magnetization of the here discussed and investigated lanthanum manganites arises from the partially filled  $3d$  orbitals of  $\text{Mn}^{3+}$  and  $\text{Mn}^{4+}$ . In a cubic crystal symmetry,  $3d$  transition metals like manganese have a quenched angular momentum [83]. As manganites crystallize in a cubic-like symmetry the magnetic moment originates solely from the uncompensated spin of the manganese  $3d$  electrons [84].

Now, it is important to answer the question about the distribution of the electron spin states within the  $3d$  subshells. The occupation of the spin states follows from energy minimization principles. In case of a free ion the occupation process follows Hund's rules. However, the manganese cations are not free, and as we have seen in case of the quenching of the angular momentum caused by the cubic crystal symmetry, the structural environment of the Mn cations play a crucial role. Nevertheless, the first and second Hund's rules still are relevant in case of  $3d$  ions [84].

In summary, the magnetism in  $\text{La}_{1-x}\text{Sr}_x\text{MnO}_3$  is determined only by the spin of the manganese  $3d$  electrons, as long as there are no  $4f$  moments.  $\text{Mn}^{3+}$  exhibits 4 valence electrons with a total spin moment of  $S(\text{Mn}^{3+}) = 2$ ;  $\text{Mn}^{4+}$  has three valence electrons resulting in a total spin moment of  $S(\text{Mn}^{4+}) = \frac{3}{2}$ .

### 3.3.2 Superexchange Interaction

In manganites the magnetic dipole-dipole interactions between neighbouring electron spin states are weak. Thus, exchange interaction processes are considered to drive long-range-ordered magnetic ground states [84]. These exchange interactions describe a hopping process of electrons between neighbouring crystal lattice sites in order to minimize the total energy.

In the following discussion we consider a crystal lattice, in which each lattice point is occupied by an electron spin of  $S = \frac{1}{2}$ . The present physical problem can be described by the following Hamiltonian:

$$H = H_t + H_U \quad (3.3)$$

The first part of the term denotes the kinetic energy  $H_t$ :

$$H_t = -t \sum_{\langle ij \rangle; \sigma} (c_{i\sigma}^+ c_{j\sigma} + c_{j\sigma}^+ c_{i\sigma}) \quad (3.4)$$

$c_{i\sigma}$  indicates the annihilation operator and annihilates a spin state  $\sigma$  sitting on a lattice point  $i$ , while  $c_{j\sigma}^+$  is the creation operator and, hence, creates a respective spin at a lattice point  $j$ .  $H_t$  does not change the sign of the spin. All nearest neighbours or spins will be added up  $\langle ij \rangle$ . The hopping integral  $t > 0$  measures the energy, which is gained by an electron due to its delocalization. The second part of the Hamiltonian  $H_U$  describes the energy cost  $U > 0$  (Coulomb energy) by the occupation of one lattice site by two electrons.

$$H = U \sum_i n_{i\uparrow} n_{i\downarrow} \quad (3.5)$$

The operator  $n_{i\sigma}$  counts the electrons with spin  $\sigma$  at the lattice point  $i$ . Here, the energetically most favoured situation is achieved by a single occupation of each lattice site. This state is not metallic, because for each charge transfer the energy  $U$  has to be spent.  $H_U$  also does not interlink the respective lattice points with each other. But, together with the hopping mechanism the spin

alignment is described and with that also the magnetism. Now, the electrons can gain kinetic energy, but, concurrently, potential energy has to be paid. If the hopping process can overcome the potential barrier, then the total energy can be minimized (*covalent bonding*). The total energy gain can be assumed to  $t^2/U$  [85]. Moreover, an antiferromagnetic alignment of the spin states is

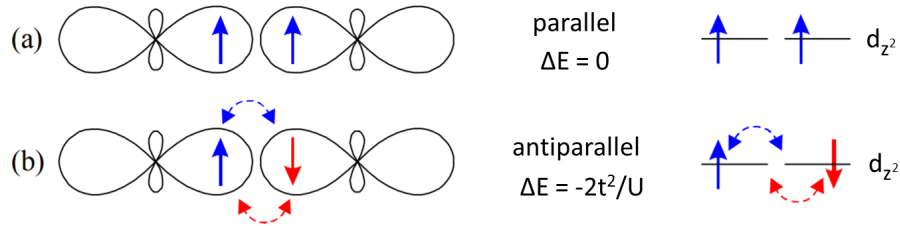


**Figure 3.7:** Sketch of a one-level-superexchange interaction of two facing  $d_{z^2}$  orbitals. The antiparallel alignment is energetically preferred. Adapted from [86].

preferred. Having the same spin orientation of two electrons at neighbouring lattice sites, a hopping is suppressed due to the Pauli exclusion principle (Fig. 3.7 (a)), while antiparallel alignment allows the hopping mechanism (Fig. 3.7 (b)). This process needs a certain overlap of the respective orbitals, in order to support the *virtual* hopping process. The described exchange interaction is also known as *superexchange*. In fact, the terminology of superexchange more often refers to an exchange interaction of a magnetic ion via an linking diamagnet [69].

In the following, two degenerate energy states for each lattice site are assumed. As a consequence two electrons with the same spin direction can occupy one lattice point without violating the Pauli principle. Fig. 3.8 sketches the four possible ground configurations of two neighbouring lattice points with two degenerated energy levels  $d_{z^2}$  and  $d_{x^2-y^2}$ , respectively. In the ongoing discussion the electron hopping process (from left to right) is constrained in the manner that the electron is not allowed to hop into the shadowed area. In case of Fig. 3.8 (a) the electron transfer is forbidden due to the Pauli principle. The situation sketched in Fig. 3.8 (b) and (c) can also be explained in analogy to the scenario shown above. Here, the reduction of the energy amounts to  $t^2/U$ . A new interesting effect can be seen in Fig. 3.8 (d). The electron hops from left to right, while the electrons exhibit the same spin orientation. Although the hopping electron has to pay the Coulomb energy  $U$ , concurrently, it also gains energy  $J_H$ , which denotes the Hund's coupling. It follows the first Hund's rule, in which a parallel spin orientation within an ion leads to a gain in energy. Therefore, this particular configuration reveals the energetically preferred state. Further, the parallel orientation of the two electron spin states is the reason for both a ferromagnetic correlation between neighbouring Mn ions and for an orbital anisotropy [86].

Next, the interaction between two  $\text{Mn}^{3+}$  cations will be shown, which are linked by an oxygen ion. As we already know, a certain orbital overlap is needed in order to enable a hopping process. Thus, only the Mn  $3d$  and O

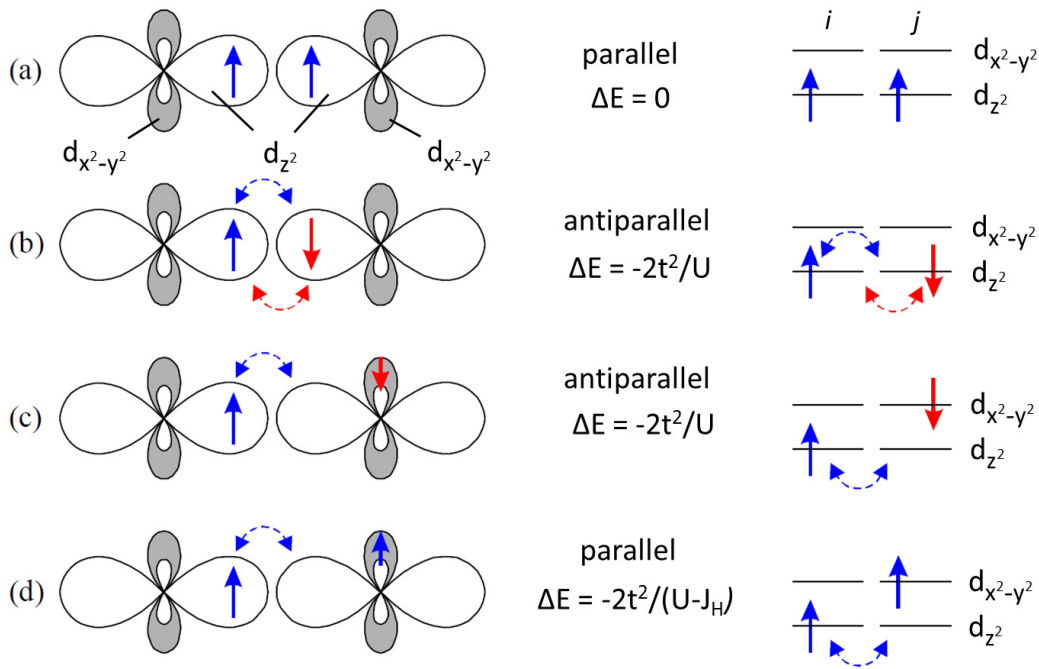


**Figure 3.8:** Superexchange interaction in case of two possible energy levels for the  $e_g$  orbital. Here, the Hund's coupling is taken into account. The  $d_{z^2}$  orbital and the  $d_{x^2-y^2}$ -orbital (shaded) are in an orthogonal alignment. The most favoured state goes along with a ferromagnetic ordering. Adapted from [86].

$2p$  orbitals have to be considered, because the overlap of the inner orbitals is significantly smaller and thus negligible.

The sketch in Fig. 3.9 illustrates the hopping mechanism within a Mn-O-Mn bond for three different configurations of the Mn spin orientation. In that picture, the O  $2p$  orbitals are filled with two electrons. The  $3d$  orbital configuration of the manganese cation, as discussed in Sect. 3.2.1, is more complex. The three located  $t_{2g}$  (large arrows) electrons spin states occupy the  $d_{xy}$ ,  $d_{xy}$  and  $d_{xy}$  orbitals, each having a spin  $S = \frac{1}{2}$ . The fourth itinerant electron (small arrow) occupies one of the two possible orbitals of the  $e_g$  level. In the present example, the  $d_{z^2}$ -orbital is directed towards the O  $2p$  states.

In Fig. 3.9 (a) and (b) the  $d_{z^2}$  orbitals of the Mn cations are either filled or empty. In these cases the electrons only hop between the O  $2p$  and the respective  $d_{z^2}$  states. This leads to an opposite spin orientation of the Mn  $3d$  electrons. Due to the strong intraatomic Hund's coupling the located  $t_{2g}$  spins have to align parallel to their according  $e_g$  states. This results in an antiferromagnetic exchange interaction.

In the next case (Fig. 3.9 (c)) the itinerant electron of the right Mn cation does not occupy the  $d_{z^2}$ -orbital, but the  $d_{x^2-y^2}$ -orbital. The energetically most favoured configuration is the one in which the respective electron follows the Hund's rules. The p-electron spin state of the oxygen ion prefers a parallel alignment with respect to the right Mn cation, while the left p-electron favours an antiparallel alignment with respect to the left spin moment of the Mn cation.

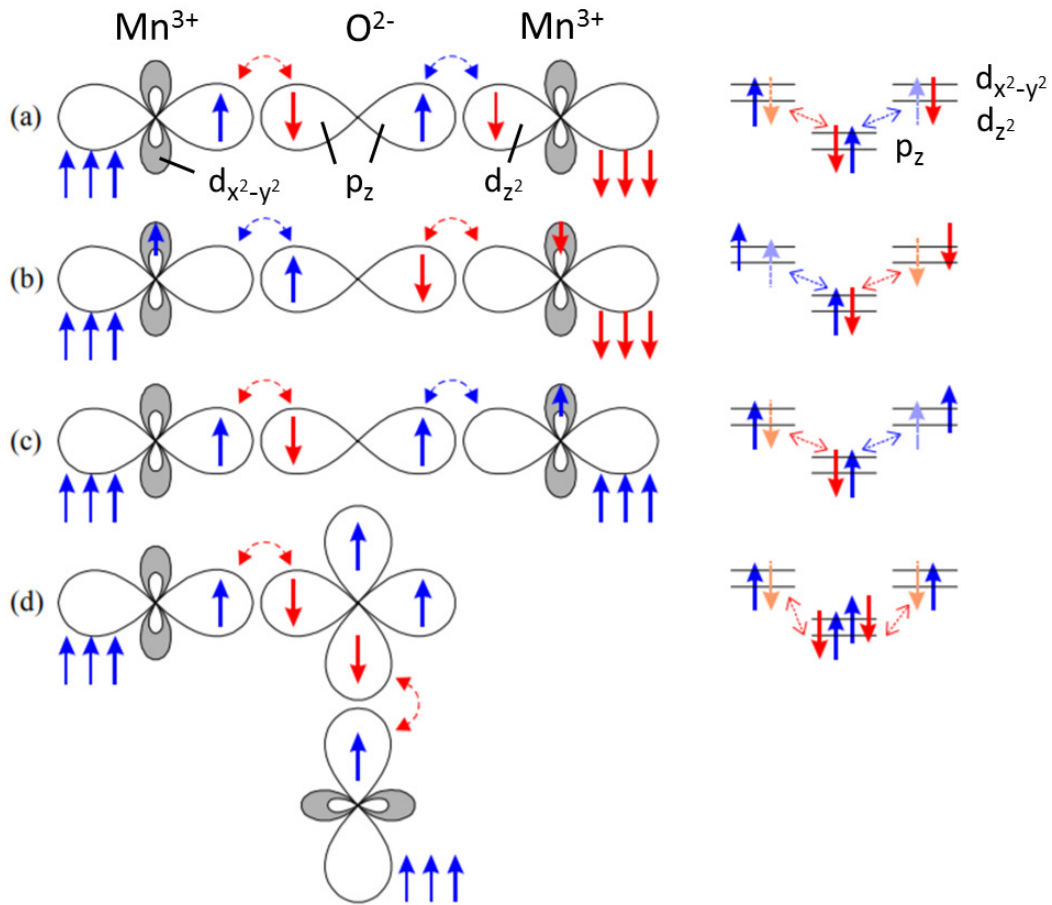


**Figure 3.9:** In order to illustrate the Goodenough-Kanamori-Anderson-rules the  $d_{x^2-y^2}$ -orbitals (shaded), the  $d_{z^2}$ -orbitals (left and right) and the  $p_z$ -orbitals (center) of a Mn-O-Mn bond are shown. The three-fold arrow group indicates the localized  $t_{2g}$  electron spin states with a spin of  $S=3/2$ . According to the occupation of the respective orbitals there are antiferromagnetic (a, b) and ferromagnetic correlations (c, d). Adapted from [86].

Consequently, this exchange interaction mediates a ferromagnetic coupling. Fig. 3.9 (d) shows the exchange interaction under an angle of  $90^\circ$  between partially filled  $d$  shell orbitals. The virtual hopping processes take place between the  $p_z$ -orbital and the right handed Mn ion. This results in a virtual intermediate state which exhibits two holes situated at the oxygen. Depending on the alignment of the manganese spin states, the two electrons left at the oxygen can be encountered in a parallel or in an antiparallel spin orientation. Here, the energy minimum of the intermediate state again will be gained by a parallel spin alignment of the electrons (or holes) situated at the oxygen. Therefore, the spins of the manganese ions are parallel as well [86].

In summary, the superexchange mechanism is a coupling phenomenon, which occurs between two nearest-neighbor  $\text{Mn}^{3+}$  cations through a shared diamagnetic oxygen ion, enabled by the hybridization between Mn  $3d$  and O  $2p$  orbitals. Virtual hopping of O  $2p$  electrons to the overlapping Mn orbitals

leads to excited states, which can result in a reduction of the total energy of the system. The sign and strength of the superexchange interaction depend on the occupancy and orbital degeneracy of the  $3d$  states. These aspects can lead to antiferromagnetic or ferromagnetic behaviour.

The results discussed above have been developed by John B. Goodenough, Junjiro Kanamori, and Phillip Anderson. They have established a set of empirically driven rules, which have proven to predict the exchange interaction for many TMOs. These rules are known as the Goodenough-Kanamori-Anderson-rules:

- 1) The exchange interaction between partially filled or empty  $d$  shell orbitals under an cation-ligand-cation angle of  $180^\circ$  is strong and antiferromagnetic.
- 2) The exchange interaction between a partially filled and an empty  $d$  shell orbital under an cation-ligand-cation angle of  $180^\circ$  is ferromagnetic but weak.
- 3) The exchange interaction between a partially filled  $d$  shell orbitals under an cation-ligand-cation angle of  $90^\circ$  is ferromagnetic but weak.

Subsequently, with all these considerations above, the magnetic configuration of  $\text{LaMnO}_3$  can be explained. Fig. 3.10 shows the assumed orbital ordering of  $\text{LaMnO}_3$ . For the sake of clarity the oxygen orbitals and the unoccupied  $d_{x^2-y^2}$

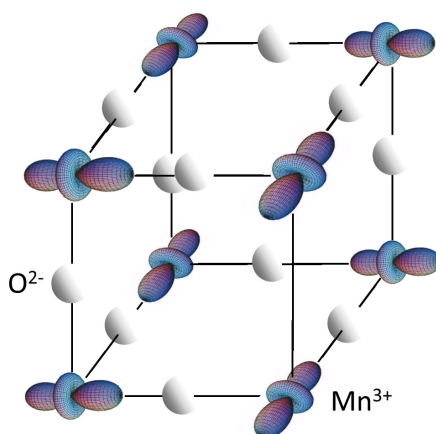


**Figure 3.10:** Cooperative Jahn-Teller-effect in  $\text{LaMnO}_3$ . As a result an orbital ordering is formed.

orbitals are not sketched. Regarding the horizontal intralayer there is always a half-filled orbital pointing towards an unoccupied orbital, which leads to an ferromagnetic ordering of these respective planes. In contrary, the interlayers reveal an antiferromagnetic coupling, which stems from an overlap of solely empty orbitals. In total, the net magnetization sums up to zero. However, one can see that this material shows a tendency to be ferromagnetic. This has been experimentally proven for samples, which showed a slight off-stoichiometry accompanied with a ferromagnetic ordering [87–89].

### 3.3.3 Double-Exchange Interaction

The previous Sect. describes insulators, due to the virtual hopping in the superexchange mechanism, where the hopping integral  $t$  has to be significantly smaller than the Coulomb repulsion ( $t \ll U$ ). In the following,  $\text{La}^{3+}$  will be partially substituted by  $\text{Sr}^{2+}$ , so that one electron is removed from an occupied manganese orbital. One can already assume, that the change in the orbital occupation is also accompanied with a change of the magnetic properties. Zener, Anderson, Hasegawa, and Gennes have shown that hole doping of  $\text{LaMnO}_3$  will lead to a ferromagnetic and metallic phase [57–59]. The underlying exchange mechanism is known as double-exchange interaction.

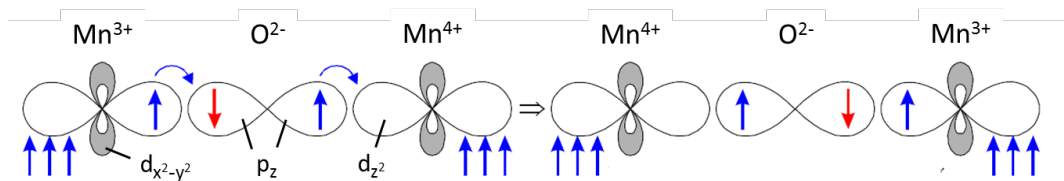


**Figure 3.11:** Double exchange mechanism between  $\text{Mn}^{3+}$  and  $\text{Mn}^{4+}$  via an oxygen anion. The three-fold arrow group indicates the localized  $t_{2g}$  spin states. A parallel alignment of the  $t_{2g}$  electrons allows the itinerant  $e_g$  electron to do a *real* hopping from  $\text{Mn}^{3+}$  to  $\text{Mn}^{4+}$ , which provides an electrical transport. Adapted from [84].

The DE interaction is sketched in Fig. 3.11. The left handed  $\text{Mn}^{3+}$  cation contains three localized  $t_{2g}$  electrons with  $S = \frac{3}{2}$ , and an itinerant  $e_g$  electron with  $S = \frac{1}{2}$ , which is situated at the  $d_{z^2}$  orbital. The right handed  $\text{Mn}^{4+}$  cation exhibits an empty  $e_g$  orbital and three  $t_{2g}$  electrons. Both Mn cations are linked by a  $p_z$  orbital of an oxygen anion. The empty  $e_g$  orbital of the  $\text{Mn}^{4+}$  cation is the crucial point, which separates the double-exchange from the superexchange interaction. By hopping into the empty  $e_g$  orbital the electron coming from  $\text{Mn}^{3+}$  does not have to overcome a repulsive Coulomb energy. Further, since the  $t_{2g}$  spin states of both Mn cations show a parallel orientation the  $e_g$  electron energetically prefers a parallel alignment to the respective  $t_{2g}$  spin states due to the strong Hund's coupling. From this, the electron shows a delocalization (*real hopping*) over the Mn-O-Mn bond, which explains the conductivity in the material. Furthermore, the parallel spin alignment is the reason for the ferromagnetic exchange. In case of an antiparallel orientation of the  $t_{2g}$  spin states of the  $\text{Mn}^{3+}$  and  $\text{Mn}^{4+}$  cations the itinerant electron would have to overcome the Hund's coupling energy. Therefore, the charge transfer would be constrained, which is accompanied by a reduced conductivity.

---

## Photoelectron Emission Spectroscopy & Microscopy

---

*Photoemission spectroscopy* (PES) is a powerful technique to investigate the electronic and chemical structure of a material in an element-selective manner. The underlying physical background of this analysis tool is the photoelectric effect, which was explained by Albert Einstein in 1905 [90]. The photoemission process describes the interaction between light and matter. The energy transfer of a photon to an electron, bound in a solid, results in an emission of *photoelectrons*. In comparison to the electron momentum, low energy photons (ultraviolet up to soft X-ray) exhibit a small momentum transfer to the respective matter, which can be neglected. Thus, the energy relation of the photoelectric effect can be simplified as in Eq. 4.1:

$$h\nu = E_{Bin} + E_{Kin} + \Phi. \quad (4.1)$$

The incident photon energy  $h\nu$  transferred to the electron can be reconstructed by the kinetic energy  $E_{Kin}$  of the emitted electron, the respective binding energy  $E_{Bin}$ , and the material's work function  $\Phi$ , which denotes the potential barrier of a solid. The binding energy of an electron is related to the chemical bonding in the crystal and provides valuable information in the chemical analysis. By measuring the kinetic energy under a defined work function of the relevant material the binding energy can be indirectly determined. Over the last decades binding energies of all elements have been measured and can be obtained from public data bases. Therefore, the measured emission peaks can be directly compared to these respective binding energies, which leads to the capability to chemically distinguish different materials. According to that the term *Electron Spectroscopy for Chemical Analysis* (ESCA) has been established.

The state of an electron in a crystal lattice can be expressed by (i) a spatial coordinate  $\vec{x}$  (point of emission), (ii) the momentum  $\vec{k}$ , which defines the direction and the velocity of the electron, (iii) a spin orientation  $\vec{s}$ , (iv) and a kinetic energy  $E_{Kin}$ . All these values can be extracted out of the analysis of emitted electrons. The photoemission electron microscope can provide information about the spatial origin of the electrons  $I(\vec{x}, E_{Bin})$ . Also, the momentum distribution  $I(\vec{k}, E_{Bin})$  can be worked out by means of *angular resolved photoemission spectroscopy* (ARPES). Additionally, the respective spin component can be probed by a spin-resolved photoemission experiment (spin-PES/ARPES). In this work, a spectromicroscope (see Sect. 4.6) is used, which is able to measure all four components ( $\vec{x}, \vec{k}, \vec{s}, E_{Kin}$ ) conserving the phase space information.

## 4.1 Photoemission Process

The photoemission process itself can be described in a simplified manner by separating it into three steps: (i) excitation, (ii) transport, and (iii) transmission [91]. The *three-step-model* gives a qualitative and intuitive explanation for the most important features of the measured photoemission spectra. There is also a quantum mechanical description, where all three steps are condensed into a *one-step-model* [92]. This single quantum mechanical process provides also a quantitative picture of the emitted photoelectrons. But, in the scope of this work the description in terms of the three-step-model is sufficient.

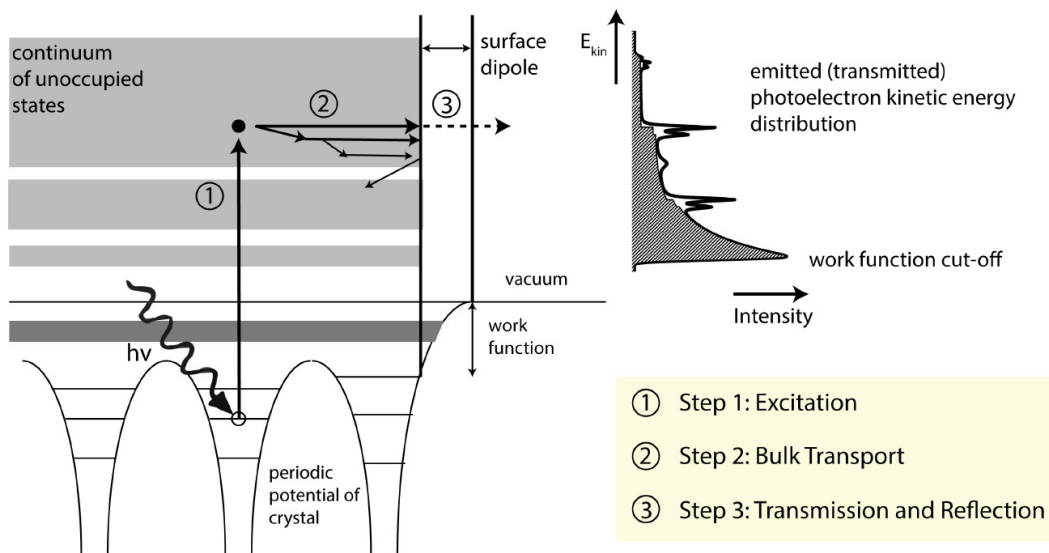


**Figure 4.1:** Illustration of the three-step-model: (1) photo-excitation of a bound electron in the solid. (2) Propagation of the photoelectron through the solid, which comes along with elastic and inelastic scattering events. (3) In order to leave the material, the electron has to overcome the surface potential barrier (work function  $\Phi$ ), which is described by the transmission process. Image taken from [45].

**Excitation** As a first step, there is the interaction of the incident light with the solid (Fig. 4.1 (1)). This leads to an excitation of an photoelectron due to the photoelectric effect, which is described in more detail in Sect. 4.2. The photoexcitation is a function of the polarization of the incident light, the photoionization cross section, and the photon energy.

**Transport** The second step describes the propagation of the excited photoelectron through the solid (Fig. 4.1 (2)). As a prerequisite for the propagation the electron has to get excited into an unoccupied state above the Fermi level. The movement of the photoelectron is impeded by elastic and inelastic scattering events with other electrons, phonons or crystal defects. The average distance between two successive impacts or scattering events can be described by the *electron inelastic mean free path*  $\lambda_{IMPF}$ . An inelastic scattering event leads to a loss of the electrons' kinetic energy, which is accompanied by a loss of the intensity  $I$ . The intensity is damped as a function of  $x$ , the distance from the point of the photoexcitation:

$$I(x) = I_0 \cdot e^{-x/\lambda_{IMPF}} \quad (4.2)$$

The *universal curve* in Fig. 4.2 shows calculated IMPFs for 41 different materials as a function of the electron energy, which ranges between 10 and 2000 eV. The term universal curve is related to the very similar shape of all curves. An explanation for that universal behaviour is given in [91]: excited electrons with a kinetic energy  $E_{kin}$  above 10 eV can be described in the picture of a *free electron gas* due to an almost free bonding state within the crystal. As a result, the electron energy loss function follows the plasma frequency, which in turn is determined by the electron density. The magnitude of this density is similar in magnitude of the respective elements.

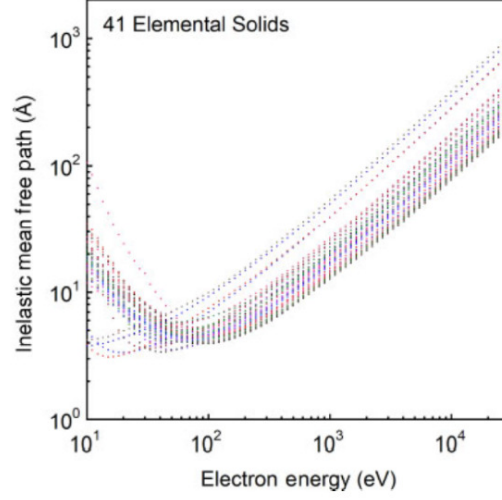
Evaluating the probing depth by using Eq. 4.2 works good for primary electrons, which only undergo elastic scattering events. Utilizing secondary electrons leads to a larger probing depth in the order of several tens of nanometers [93].

By means of hard X-ray photoemission electron spectroscopy, spectral information from the bulk material can be extracted because of its  $\lambda_{IMPF}$  of up to ten nanometers. Even though this technique gives important and exciting insights of the investigated material, there is a trade off due to the very low photoionization cross section compared to soft X-rays. Hence, HAXPES experiments require a high-brilliance X-ray light source, e.g. a synchrotron facility, in order to achieve reasonable photoelectron counting rates.

**Transmission** In the third step the photoelectrons escape from the solid into the vacuum (Fig. 4.1 (3)). The electron has to overcome the surface potential barrier, e.g. the work function  $\Phi$ .

Electrons with energies not exceeding the work function are supposed to be reflected at the crystal/vacuum interface and do not leave the material. This gives rise to the *cut-off* defining the sharp emission onset.

**Figure 4.2:** IMPFs of different elemental solids as a function of the electron energy. The resulting universal curve shows that the IMPF increases up to several tens of nanometers, with increasing kinetic energy of the electrons. Image taken from [94].



## 4.2 The Photoexcitation Process - Fermi's Golden Rule

A quantum mechanical description of the three-step model is based on the many body Hamiltonian  $H$ . The solution of the Hamiltonian results in the ground state  $\Phi_i$  and all possible excited states  $\Phi_n$  of the electron system. Neglecting the inter-atomic as well as electron-electron interactions the problem is simplified to a single-particle picture, which can be solved by means of perturbation theory. A detailed derivation of this assumption is given in [91]. Finally, the treatment results in a mathematical expression for the transition probabilities  $W$  of the ground state  $\Phi_i$  into an allowed final state  $\Phi_f$ , which is known as *Fermi's Golden Rule*:

$$W \sim |\langle \Phi_f | H^{int} | \Phi_i \rangle|^2 \delta(E_f - E_i - h\nu) \quad (4.3)$$

The strength of a transition from an initial state to a final state is determined by the transition matrix element:

$$M_{fi} = \langle \Phi_f | H^{int} | \Phi_i \rangle. \quad (4.4)$$

Here,  $H^{int}$  denotes a perturbation originating from the incident photons.  $E_f - E_i$  (from Eq. 4.3) describes the energy difference between the states  $\langle \Phi_f |$  and  $| \Phi_i \rangle$  and the energy conservation is expressed by the  $\delta$ -function. In particular, the perturbation  $H^{int}$  is expressed by a vector potential  $\mathbf{A}$  describing the external electric field due to the incident photons, the momentum operator  $\mathbf{p}$ , the speed of light  $c$ , the electrons' charge  $e$  and the invariant mass  $m$ , which denotes the mass of a stationary electron:

$$H^{int} = \frac{e}{mc} \mathbf{A} \cdot \mathbf{p}, \quad (4.5)$$

where  $\mathbf{A}$  can be mathematically expressed as a plane wave:

$$\mathbf{A}(\omega t) = A_0 \sigma e^{i(\omega t - \mathbf{q} \cdot \mathbf{r})}. \quad (4.6)$$

$\sigma$  denotes the photon polarization,  $\mathbf{q}$  indicates the photon momentum and  $\mathbf{r}$  is the coordinate. In case that the wavelength of the electromagnetic radiation  $\lambda$  inducing the photoemission process is large compared to the atomic distance, the incident light can be treated in the *electric dipole approximation* [95]. This means, that the electric field  $\mathbf{A}$  at the position of the respective atom is assumed to be constant during the photoexcitation process. From this,  $e^{i(\omega t - \mathbf{q} \cdot \mathbf{r})}$  amounts to  $\sim 1$  and the transition matrix element can be simplified as in Eq. 4.7:

$$M_{fi} \propto \langle \Phi_f | \sigma \cdot \mathbf{q} | \Phi_i \rangle. \quad (4.7)$$

Based on the symmetry properties of initial  $|\Phi_i\rangle$  and final state  $\langle \Phi_f|$ , as well as the perturbation operator  $H^{int}$ , it can be derived that  $M_{fi}$  is nonzero only in certain cases, which can be summarized as dipole selection rules. The transition probability is evaluated on the basis of the quantum numbers  $|n, l, m_l, s, m_s\rangle$ . The wave function  $|\Phi\rangle$  of atomic core levels consists of a radial part, spherical harmonics and a spin part [27]:

$$|\phi\rangle = |R(r)\rangle |Y_{l,m_l}(\Theta, \phi)\rangle |X(s)\rangle \quad (4.8)$$

Only for particular values of  $l$  and  $m_l$  the transition matrix element  $M_{fi}$  deviates from zero, which results in the dipole selection defined in Eq. 4.9-4.11. The angular momentum  $l$  has to change by 1 ( $\Delta l = 0 \pm 1$ ) and there is no deviation allowed in the total spin  $s$  ( $\Delta s = 0$ ).

$$\Delta l = l_2 - l_1 = \pm 1 \quad (4.9)$$

$$\Delta m = m_2 - m_1 = 0, \pm 1 \quad (4.10)$$

$$\Delta s = s_2 - s_1 = 0 \quad (4.11)$$

### 4.3 Electron Spectroscopy for Chemical Analysis (ESCA)

So far, the fundamental aspects of the photoemission process have been discussed. The following sections are concerned with the analysis of the emitted electrons utilizing *X-ray photoemission spectroscopy* (XPS) and *X-ray absorption spectroscopy* (XAS). XPS is a technique, which probes the occupied electronic states of a material. The incident photon energy is kept constant, while the analyzer unit measures the kinetic energy distribution of the emitted electrons. In XAS mode the photon energy is tuned. Here, monitoring the absorption characteristics leads to information about the unoccupied states.

These complementary photoelectron spectroscopic modes provide an element-selective analysis and will be discussed in the following in more detail.

### 4.3.1 X-Ray Photoemission Spectroscopy (XPS)

Experimentally, X-ray photoemission spectroscopy is based on monochromatic light impinging on a specimen and the energy resolved detection of the outgoing photoelectrons  $I(E_{kin})$  Fig. 4.3 (a). A fixed photon energy and a known work function of the material enable a determination of the respective binding energy. The binding energy spectrum  $I(E_B)$  with its characteristic emission lines reflects the occupied states of the solid, which is a result of the electronic structure. Emission lines occur whenever the condition  $E_{Kin} = h\nu - E_{Bin} - \Phi$  (Eq. 4.1) is fulfilled. Since calculated and experimental reference values for binding energies are listed in databases [96], the energy position of the emission peaks can be used for chemical analysis.

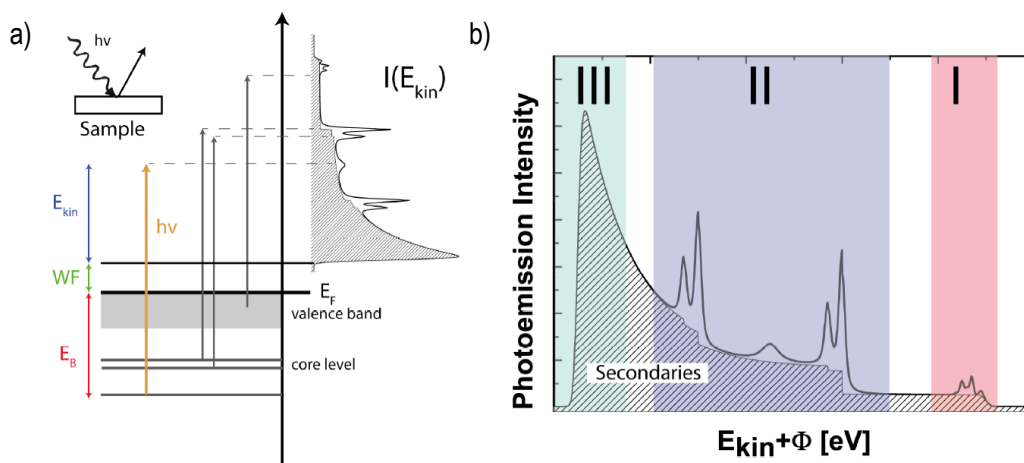


**Figure 4.3:** (a) Energy diagram of the photoemission process. Bound electrons absorb the photon energy  $h\nu$  of the incident light. One part of the energy is used to overcome the work function  $\Phi$ . The remaining energy accounts to the kinetic energy  $E_{kin}$ . (b) Illustrative photoemission spectrum separated into three section: (I) valence band (VB), core level (CL), and secondary electrons. Image taken from [45].

In Fig. 4.3 (b) such an XPS spectrum is shown and typically it can be separated into three parts. First, there is the *valence band* (VB) region (I) characterized by electrons, which are close to the Fermi level (0-20 eV). Here, the overlap of neighbouring electronic wave functions and the concurrent delocalization of the electrons lead to a formation of energy-dispersive bands. The electrons defining the VB originate from all elements of the respective material, which results in entangled and strongly modulated spectral fingerprints. This results in a challenging analysis of the VB, but the information density is high and reveals details about the chemical bonding, electronic and optical properties.

The second spectral section is the *core level (CL)* region (II). In comparison to the VB, here, the region is mainly determined by sharp emission lines and well defined binding energies. This is due to the localized wave function of the electrons with respect to the atomic core, resulting in smaller probabilities of a direct interatomic interaction. Thus, the spectral features are directly related to the respective elements. This, for instance, can be used for evaluating the stoichiometry of a composition.

Section three (III) shows an exponential increase of the emission intensity due to low-kinetic photoelectrons created by multiple, elastic and inelastic scattering events. These electrons are also known as *secondary electrons*. Thus, at some point the kinetic energy of the electrons is not large enough to leave the crystal. The material specific potential surface barrier, reflected by the work function  $\Phi$ , causes a hard cut-off for the low kinetic energy range.

### 4.3.2 X-Ray Absorption Spectroscopy (XAS)

In an XAS experiment the photon energy is varied, while the emitted photoelectrons are detected. As already mentioned the X-ray absorption is also based on the photoelectric effect and follows Fermi's Golden rule. The energy of the photon is transferred to a bound core electron situated in an atom. Subsequently, the electron is excited to an unoccupied state below the vacuum level (Fig. 4.4). A necessary condition is that the energy of the incident photon is larger than the energy of the bound atomic state of interest. A relaxation of the atom is realized by filling the created core hole with an electron from an upper shell followed by emission of a photon or an *Auger electron (AE)*.

In the first case of emitting a photon, the intensity of the fluorescence can be detected utilizing a photon detector and is directly related to the absorption coefficient, which depends on the samples' density, the atomic number  $Z$ , the atomic mass of the probed atom, and the incident photon energy  $E_{ph}$ . In the *fluorescence yield (FY)* detection mode the *attenuation length* of the fluorescence radiation is of the same order as the attenuation length of the incident X-ray beam. This results in a probing depth of several  $\mu m$ .

In the Auger excitation process the electron propagates through the material towards the surface and escapes from the sample. During the propagation the Auger electron excites secondary electrons creating an electron cascade. All escaping electrons are summarized to the *total electron yield (TEY)*. Moreover, the absorption profile of the TEY contains a background signal originating from elastic and inelastic scattering processes, which gives rise to more bulk sensitive information. The TEY can be measured by a sample current, as an electron current is needed in order to replace the emitted electrons. For this, a conductive sample is required. Further, the probing depth is constrained by the mean free path of the Auger electrons (2-5 nm). The advantage of the TEY detection is the amplification of the absorption signal caused by the electron cascade, which enables a detection of also small absorption deviations.

The absorption resonance increases abruptly, when the incident photon energy

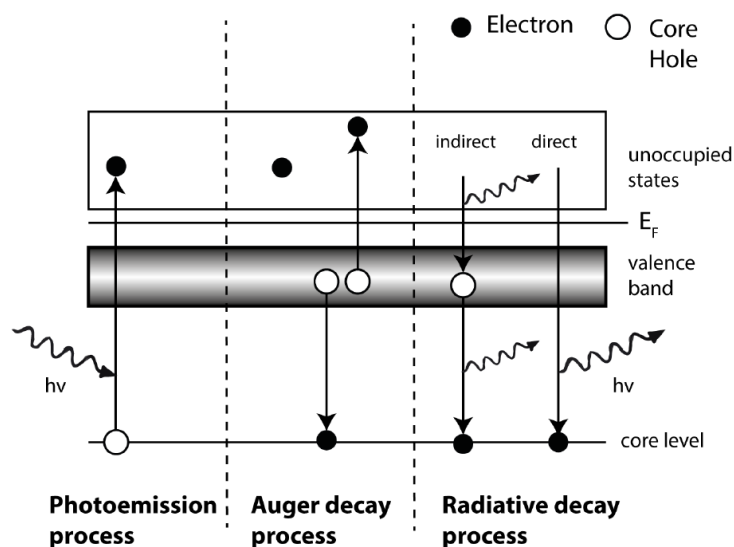


**Figure 4.4:** Core hole relaxation and photoexcitation processes: (left) An incoming photon  $h\nu$  can be absorbed, if it equals to the atomic binding energy  $E_B$ . Thus, the core level electron can be emitted to the unoccupied states. (middle) Auger excitation process: A core hole can be refilled by an electron from an higher energy level. The according release of energy can be transferred to adjacent electrons electrons. (right) The relaxation of the electron into the core hole can be accompanied by the emission of photons. Image taken from [45].

is just below the binding energy of a core electron. This "jump" in absorption is called *absorption edge* and mainly represents transitions to the lowest unoccupied states governed by the dipole selection rule. Here, it is worth to mention, that the white line intensity is proportional to the number of valence holes in the ground state [97]. The absorption spectrum is broadened by the life times of the core-hole and the excited photoelectron, as well as the experiments' energy resolution.

In this work, only *X-ray absorption near edge spectroscopy* (XANES) has been performed, which reflects the electronic structure and therefore the atomic environment of the investigated sample. The interpretation of XAS spectra is often very complicated and not straightforward. So the analysis is mainly based on qualitative and empirical methods. Simulation codes based on theoretical models exist, which have shown reasonable agreement with experimental data in some cases [98, 99].

## 4.4 Spin-Orbit-Coupling (SOC)

The photoexcitation of an electron creates a core hole in the respective atom, which exhibits a spin moment  $S = 1/2$  and an orbital angular momentum  $L = 0, 1, 2, \dots$  (familiar notation:  $s, p, d, \dots$ ). These moments are coupled by the spin-orbit interaction and cause a splitting of the so far degenerated energy

levels of the core hole. This results in a total angular momentum  $\mathbf{J} = \mathbf{L} + \mathbf{S}$ . Thus, the total momentum amounts to  $J_{\pm} = |L \pm 1/2|$  and leads to two distinct energy levels for  $L \neq 0$ . The ratio of the degeneracy  $J(J+1)$  of these two states determines the relative intensity of the spin-split peaks:

$$\frac{J_+(J_+ + 1)}{J_-(J_- + 1)} = \frac{2(L + 1/2) + 1}{2(L - 1/2) - 1} = \frac{L}{L + 1} \quad (4.12)$$

Thus, the following peak ratios can be derived: 1:2 for  $p$ , 2:3 for  $d$ , and 3:4 for  $f$ -shells.

## 4.5 X-Ray Magnetic Circular Dichroism (XMCD)

X-ray magnetic circular dichroism is a technique, which probes the magnetic properties of a ferromagnetic material in an element-selective manner. It is based on the X-ray absorption process and utilizes circularly polarized light. XMCD is a spin-dependent absorption process measuring an intensity difference, which corresponds to the difference of the number of spin-up and spin-down holes reflecting the magnetic moment.

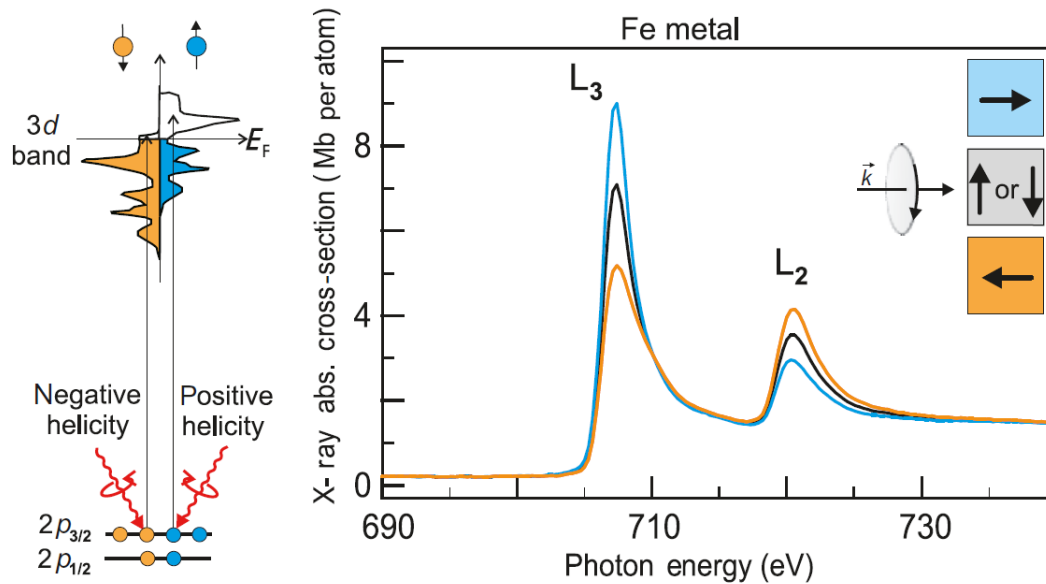


**Figure 4.5:** Illustration of the XMCD effect on the example for the Fe  $L$ -edge. (left) XMCD process can be described by a two-step model, in which the polarized X-rays create spin-polarized photoelectrons which are, in a second step, detected by the exchange-split valence shell. (right) XAS signal of the  $L_{3,2}$ -edge for a circularly polarized light with positive angular momentum, and the colour-coded spectra correspond to the sample magnetization directions. Image taken from [97].

In order to understand the XMCD process a Stoner spin-split material is assumed, as it is shown in Fig. 4.5 (left). The dichroism effect stems from the difference of the  $p \rightarrow d$  transition intensities for incident photons with positive angular momentum ( $\mathbf{L}_{ph}$  points towards  $\mathbf{k}$ ) and negative angular momentum ( $\mathbf{L}_{ph}$  points towards  $-\mathbf{k}$ ) aligned along the fixed magnetization direction  $\mathbf{M}$  of the sample. Another equivalent approach is to fix the photon spin direction, while switching the magnetization directions [97].

A parallel and antiparallel alignment of the polarized X-rays and the photon spin lead to a maximum and minimum of the XMCD signal, respectively. With a perpendicular orientation of the photon spin and the magnetization direction "up" and "down" spins cannot be distinguished (Fig. 4.5(right)). According to these relations the XMCD signal is defined as:

$$\Delta I = I^{\uparrow\downarrow} - I^{\uparrow\uparrow}, \quad (4.13)$$

while the arrows denote the orientation between the photon spin and the magnetization direction.

The magnetic circular dichroism can be explained in the picture of a two-step model. The first step is a consequence of the conservation of the angular momentum. The angular momentum of the incident circularly polarized light is transferred to the excited photoelectrons. Excited photoelectrons originating from a spin-orbit split level, for instance, the  $2p_{3/2}$  level ( $L_3$ -edge) become spin-polarized by a (partial) transfer of the angular momentum to the spin through the spin-orbit coupling. The spin quantization axis is aligned with the direction of the incident X-rays. Due to the opposite sign of the spin-orbit coupling ( $l + s$  and  $l - s$ ) of the  $2p_{3/2}$  ( $L_3$ ) and  $2p_{1/2}$  ( $L_2$ ) levels, accordingly, the spin polarization at the two edges will be opposite.

In the second step, the spin-polarized photoelectron is transferred to an unoccupied state in the conduction band above the Fermi level. Thus, the exchange-split valence band acts as a spin-detector for the respective electrons. For perfect detection the detection axis, which is the valence shell spin quantization axis, has to be aligned with the photoelectron spin. According to the Fermi rule the transition probability  $W$  is spin-dependent and thus can describe the differences in a dichroic spectrum. A detailed description of the transition probabilities can be found in [97].

### Magneto-Optical Sum Rules

XMCD spectra provide element-specific magnetic information, which can be extracted by a quantitative analysis. For this purpose, the magneto-optical sum rules can be employed in order to estimate the orbital and spin magnetic moment of  $3d$  transition metals [100, 101]. The sum rules were derived within a localized picture in which the electric dipole transitions of a single ion are considered to occur in an arbitrary crystal field. On the basis of the XMCD data and the corresponding XAS spectrum the orbital and spin magnetic

moments,  $m_{Orb}$  and  $m_{Spin}$ , can be calculated by the following equations:

$$p = \int_{L_3} (\mu^+ - \mu^-) d\mu \quad q = \int_{L_{3,2}} (\mu^+ - \mu^-) d\omega \quad r = \frac{1}{2} \int_{L_{3,2}} (\mu^+ + \mu^-) d\omega \quad (4.14)$$

$$m_{Orb} = -\frac{2q}{P_c \cos\vartheta} N_h \quad (4.15)$$

$$m_{Spin} = \frac{-3p + 2q}{P_c \cos\vartheta} N_h \left( 1 + \frac{7\langle T_Z \rangle}{2\langle S_Z \rangle} \right)^{-1}, \quad (4.16)$$

where  $p$  and  $q$  indicate the integrals of the XMCD spectrum over the  $L_3$ -edge and both  $L_{3,2}$ -edges, respectively. The integral over the whole XAS spectrum ( $L_{3,2}$ -edge) is described by  $r$ . The absorption spectra recorded under inverse magnetization or polarization are represented by  $\mu^+$  and  $\mu^-$ .  $N_h$  denotes the number of  $3d$  holes per formula unit of the respective metal cation. The magnetic dipole operator  $\langle T_Z \rangle$  is a measure of the anisotropy of the spin density and can be neglected for cubic symmetry and thus for LSMO [102]. The factor  $1/(P_c \cos\vartheta)$  accounts for the fact that the XMCD signal scales with the degree of circular polarization and the angle  $\vartheta$  between the incident beam and the direction of the magnetization of the sample.

## 4.6 Photoemission Electron Microscopy (PEEM)

In the material system investigated in this work, the resistive switching processes take place on a sub-micron scale. In order to study these microscale redox processes one needs a measurement technique, which offers an appropriate spatial resolution. The extraction of micro-structural information can be combined with an XAS or XPS experiment resulting in an advanced measuring tool called *spectromicroscopy*. Here, apart from the chemical fingerprint, also a spatial information is given, and can map where the photoelectron comes from with a high accuracy. This concept is realized in the photoemission electron microscope, where the lateral intensity distribution  $I(\vec{x})$  is imaged.

All spectromicroscopical experiments presented in this work were performed with the AC FE-LEEM P90 instrument (SPECS GmbH), an aberration corrected *low energy electron microscope* (LEEM) and PEEM. This experimental end-station finds its application at the FZ Jülich beamline UE56/ 1-SGM at the synchrotron light source BESSY II in Berlin. Since the requirements of the electron optics are similar for LEEM and PEEM, both can be implemented in the same instrument. However, we solely focused on the PEEM mode and thus the LEEM mode will not be discussed in further detail.

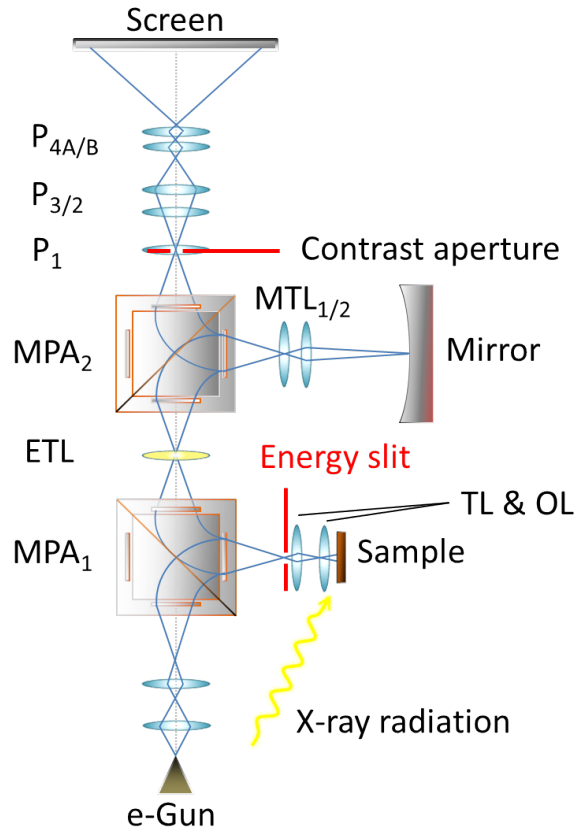


**Figure 4.6:** Schematic description of the electrons' trajectory through the LEEM/PEEM facility. An aberration correction unit comprising an electrostatic electron mirror compensates the imaging errors mainly originating from the objective lens, adapted from [95].

The working principle and the electron beam path through the microscope are described in Fig. 4.6. Starting with the illumination of the sample, there are two possible photon sources, with an incident angle of  $25^\circ$ , that can be used for the PEEM measurements: synchrotron X-ray radiation (X-PEEM) and a mercury discharge UV-lamp (UV-PEEM). Spectra and images are recorded in the TEY mode, which is dominated by secondary electrons. The sample stage is supported on an XYZ translation table driven by linear piezomotors. From this, the distance between sample and objective lens can be adjusted to the right focus position. In order to correct further imaging errors, the sample tilt can also be adapted to align the samples surface normal with the optical axis of the *objective lens* (OL).

The sample (cathode) is set to a potential of  $-15$  kV, which results in an acceleration of the emitted photoelectrons towards the grounded OL (extractor). The photoelectrons reaching the OL can be described by the drift energy:

$$E = E_0 + eU, \quad (4.17)$$

while  $E_0$  indicates the energy of the emitted photoelectrons. The resulting electrostatic field is also known as *immersion field* and finds its detailed discussion in the frame of the electronic immersion microscopy concept [103, 104]. The lateral spatial resolution of the microscope is limited to spherical and chromatic aberrations. However, realizing as large as possible sample potentials reduces the electrons' relative energy spread  $\Delta E/E$  and improves the resolution, due to a reduction of imperfections in the electron optics along the electron path.

The image made of the emitted photoelectrons is magnified by the objective lens and the adjacent transfer lens. A magnetic prism array  $MPA_1$ , comprising four rectangular field segments, deflects the electrons by 90 degrees. The image passed through the only *electrostatic lens* (ETL) in the setup, enters the  $MPA_2$ , where it gets deflected into the aberration correction unit. Here, the electrostatic electron mirror corrects chromatic and spherical aberrations originating from the objective lens. Apart from the electrons energy spread  $\Delta E/E$  and diffraction errors this is the most crucial factor limiting the resolution. Four electrodes of particular potential arrangement forming the electrostatic mirror cause aberrations directly opposite to the aberrations of the objective lens and compensate the initial imaging errors. In case of the microscope described, a best lateral resolution of 34 nm was achieved [105].

After the aberration correction unit the electrons pass the  $MPA_2$  the second time and are directed through the projective lenses P1 to P4, where the resulting image gets magnified and projected to the multi-channel plate with an adjacent phosphor screen. The image is then finally recorded by a CCD camera.

A real space image of the photoelectron intensity  $I(x, y)$  can be acquired for varied kinetic energies of the electrons  $E_{kin}$  or for different photon excitation energies  $E_{ph}$ . The output is a three dimensional stack of images  $I(x, y, E_{ph})$ , while the pixel matrix of the CCD camera determines both the image size and the point resolution (Fig. 4.7). A particular *region of interest* (ROI)  $P(x, y)$  can be integrated of the selected area and then plotted, for instance, as a function of the photon energy  $E_{ph}$ , which results in an intensity profile for this specific region. In conclusion, chemical variations within defined areas

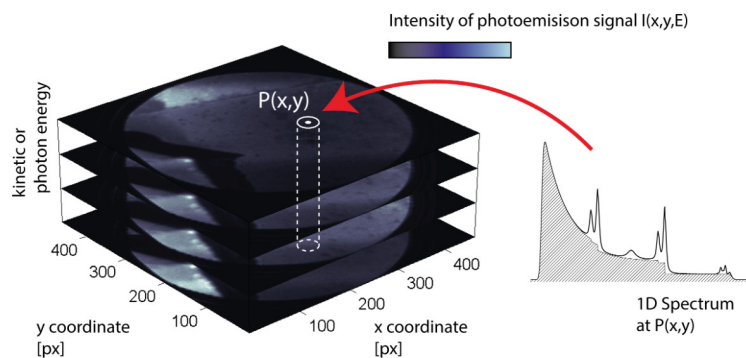


**Figure 4.7:** Acquisition of real space images at different photon energies. The 3D data set can be reduced to one dimension by defining  $P(x, y)$  and extracting data along the energy axis. Image taken from [45].

of an image can be distinguished due to appearing contrasts. Furthermore, the extraction of a spectrum at these ROIs give an insight into the respective chemical fingerprint.

## 4.7 Synchrotron Radiation Photon Source

A crucial prerequisite realizing a successful PEEM experiment is a high quality photon source with appropriate properties fitting to the requested information needed. First, a tunability of the photon energy enables varying the probing depth and is mandatory to realize absorption studies. The experimental resolution can be significantly influenced by the monochromaticity with a well-defined polarization, while a high photon flux shall provide a good signal-to-noise ratio in the detected photoelectrons. All these requirements can be provided by a synchrotron radiation facility. The working principle is based on electromagnetic radiation emitted by relativistic electrons or positrons forced on curved trajectories. In particular, these curved trajectories are realized by bending magnets or undulators.

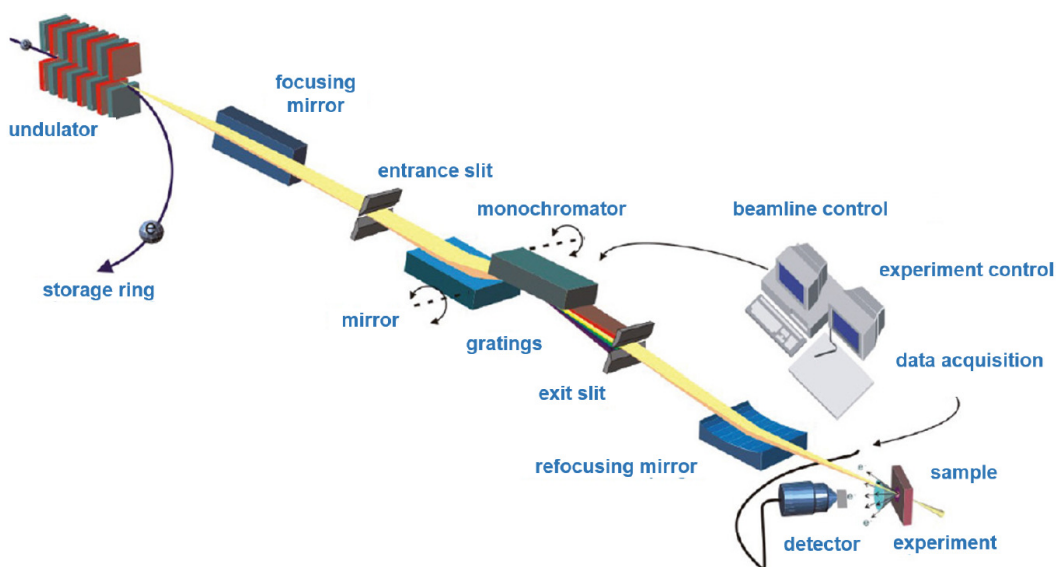


**Figure 4.8:** Scheme of a typical synchrotron beamline setup. Image taken from [95].

An undulator consists of periodical arrays of magnet pairs with alternating magnetic field directions, which force the electrons into oscillations perpendicular to the direction of their movement, due to the *Lorentz force*. The resulting radiation undergoes constructive and destructive interference, generating monochromatic light with a narrow energy width and a high photon intensity [106]. The magnitude of the emitted photon energy is a function of the magnetic field  $\vec{B}$  in the undulator and the square of the kinetic energy of the accelerated electrons  $\sim E^2$ . The radiation's wavelength generated by the

undulator can be tuned by altering the magnetic field, which is realized by opening or closing the gap between the magnetic rows. The polarization of the synchrotron radiation can be changed by a lateral shift of the magnets' position.

In the next step, the radiation is directed into a monochromator, which consists of Si gratings, and will be finally refocused onto the sample by curved mirrors (Fig. 4.8). More details about the working principle of a synchrotron radiation facility can be found elsewhere [12, 107].

The technical specifications of the BESSY UE56-1 SGM beamline are listed below in Table 4.1:

Type	Ring current	Photon energy range	Resolving power $E/\Delta E$	Photon flux	Polarization	Spot size source	Spot size sample
Soft X-ray	300 mA @ 1.7 GeV	55-1500 eV	> 10000	$2 \times 10^{13}$ Ph/s	Linear (horizontal, vertical), elliptical	40 $\mu\text{m}$ x 40 $\mu\text{m}$	15 $\mu\text{m}$ x 30 $\mu\text{m}$

**Table 4.1:** Specifications of the BESSY UE56-1 SGM beamline.



## **Part II**

# **Experimental Methods**



---

## Sample Preparation

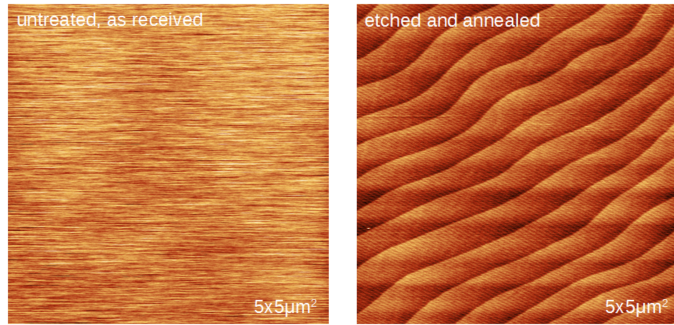
---

In the following the most relevant experimental methods, applied in this work, will be briefly introduced. Beginning with the substrate preparation and the subsequent thin film growth process, performed with the pulsed laser deposition technique, also structural analysis tools will be introduced. Afterwards, the characterization of the magnetic thin film properties via vibrating sample magnetometry will be discussed. Finally, we focus on the working principle of an aberration corrected X-ray photoelectron emission microscope.

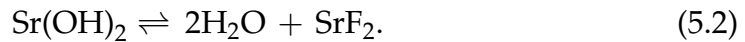
### 5.1 Substrate Termination

As a prerequisite for epitaxially grown thin films of high quality and repeatable enhanced performance also high-quality substrates are required. In the context of our purposes this includes a  $\text{TiO}_2$ -termination of niobium-doped  $\text{SrTiO}_3$  and an atomically flat surface, which can be achieved by an etching process and a subsequent annealing step, respectively [108]. The Nb:SrTiO<sub>3</sub> substrate in (001) orientation consists of an alternating arrangement of non-polar SrO and TiO<sub>2</sub> planes along the c-axis. Thus, the surface-terminating plane of Nb:STO determines the atomic layer sequence of epitaxially deposited thin films. Since a TiO<sub>2</sub> termination of the Nb:STO substrate is predicted to be energetically more stable than for SrO termination [14], we used TiO<sub>2</sub>-terminated substrates in order to obtain well-controlled interfaces. The as-received substrates, obtained from the crystal manufacturer *Crystec GmbH*, are chemically and mechanically polished, and exhibit a mixture of SrO and TiO<sub>2</sub> terminations. This results in a disordered step terrace structure. The following

**Figure 5.1:** (left) Untreated as-received substrate shows no defined surface structure. (right) After an etching procedure with buffered hydrofluoric acid (BHF) and subsequent annealing. The surface exhibits a regular terrace structure.



chemical treatment provides the  $\text{TiO}_2$  termination. Firstly, the as-received substrates were put into an ultrasonic bath with deionized water to enhance etch selectivity of  $\text{SrO}$  over  $\text{TiO}_2$  by the formation of  $\text{Sr}(\text{OH})_2$  (hydroxylation). Afterwards, the formed  $\text{Sr}(\text{OH})_2$  can be easily dissociated by a buffered hydrofluoric acid (BHF) in 30 seconds, which finally results in a  $\text{TiO}_2$ -terminated surface:



After this treatment the terminated substrate passes through some cleaning steps using acetone and isopropanol. In order to achieve a smooth terrace structure, the substrate has to be annealed for two hours at  $950^\circ\text{C}$ . AFM images in Fig. 5.1 show an annealed, but not etch-treated substrate (left side), as well as a  $\text{TiO}_2$ -terminated substrate after an additional post annealing procedure (right side). In contrast to the untreated substrate the terrace structure is very smooth and exhibits no kinks. The height of one terrace step corresponds to that of one unit cell (0.3905 nm).

## 5.2 Pulsed Laser Deposition

Pulsed laser deposition is a versatile thin film deposition technique in which a pulsed laser beam of a wavelength in the UV range, is employed to ablate a target composed of the desired thin film material. In particular, PLD is a suitable method to transfer the complex stoichiometry of multicomponent target materials into thin films at high ambient pressure [109, 110].

High-energetic nanosecond laser pulses are projected through a small aperture onto a rotating solid target (Fig. 5.2). The resulting laser target interaction comprises a complex thermodynamical non-equilibrium plasma process [111, 112]. It is determined by the laser characteristics, as well as optical and thermodynamic properties of the target [113]. During the absorption process, the energy of the laser beam first is converted into electronic excitation and subsequently in thermal, chemical and mechanical energy resulting in an ablation of the target material [114], which takes place in a time interval short enough to suppress the dissipation of excitation energy beyond the actually ablated

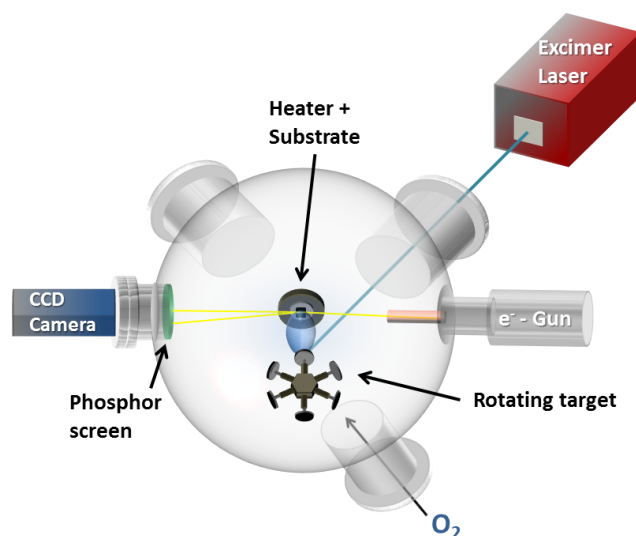


**Figure 5.2:** Illustration of a RHEED-assisted PLD setup. Laser pulses directed on the target create a plasma *plume*. The substrate mounted at the heater is located in the center of the plume. The growth process is monitored by a high-pressure RHEED system, in which an electron beam impinges the surface of the substrate by grazing incident, while the phosphor screen shows the resulting diffraction pattern. Characteristic intensity fluctuations of diffracted spots, due to particular growth modes, are monitored by a CCD camera.

volume. Thus, the destruction of the remaining target is minimized and segregation of the different components is largely avoided. Component-dependent melting temperatures of the individual ion species are negligible, and the stoichiometry of the target material is basically conserved in the plasma phase. The evaporated species consist of energetic evaporants congruent with the target (atoms, molecules, ions, clusters and electrons). All together form a plasma *plume*. After irradiation the plume, which is orthogonally oriented to the target surface, rapidly expands towards the substrate. In the presence of a particular background pressure the kinetic energies of the respective target constituents can vary from 0.1 meV up to several electron volts. A deposition temperature of the substrate between 600 °C and 850 °C provides the required surface mobility of the adatoms in order to self-arrange to the energetically favoured surface positions, resulting in a well-ordered growth mode [115, 116]. Due to the high complexity of this ablation process, it is a prerequisite to find the right deposition parameters to ensure an epitaxial and stoichiometric thin film growth. The laser fluence  $J$  determines the ablation process, the background pressure  $\rho$  influences the kinetic energy of the plume constituents as well as their oxidation state [117], and the deposition temperature of the substrate ensures a sufficient surface mobility of the adatoms. In the present setup, a 50 W KrF excimer laser (*Twente Solid State Technology (TSST), B.V., The Netherlands*) with a wavelength of  $\lambda = 248$  nm is used, which commonly exhibits a large absorption coefficient for complex oxides.

Laser pulses in the nanosecond regime and adjustable repetition rates between  $f = 1$  Hz and 50 Hz, and laser fluences from  $1 \text{ J/cm}^2$  to  $3.2 \text{ J/cm}^2$  can be achieved. Oxygen background pressures between  $10^{-5}$  mbar and 0.5 mbar are typically used and the substrate can be heated to deposition temperatures of up to  $950^\circ\text{C}$ . Further details of the PLD process can be found in Ref. [118]

### 5.3 Reflection High Energy Electron Diffraction

The thin film growth process performed with PLD is monitored *in situ* by a RHEED system (*TorrRHEED<sup>TM</sup>*, STAIB Instruments GmbH, Germany), which can be utilized at high pressure. A differential pumping system enables an operation at oxygen background pressures of up to 0.5 mbar. Due to the diffraction of electrons by surface atoms, this technique provides information about the surface structure and morphology.

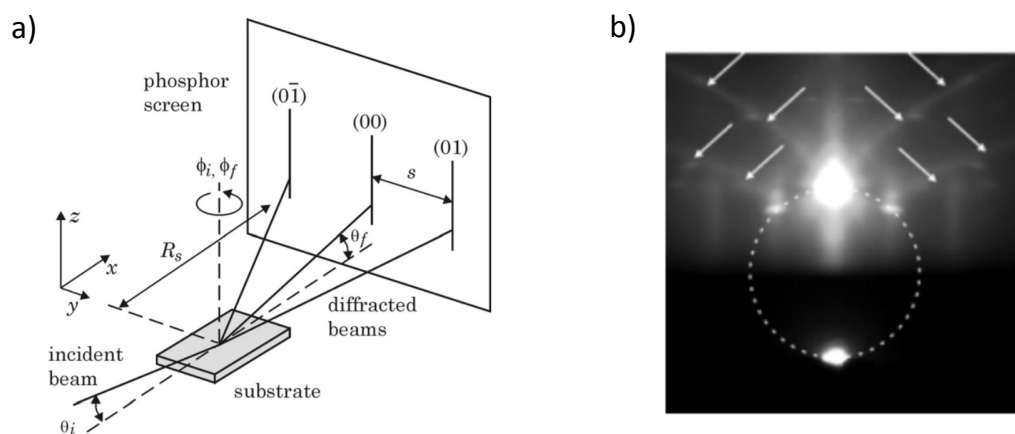


**Figure 5.3:** (a) Illustration of the RHEED geometry. (b) Diffraction pattern of an atomically flat  $\text{SrTiO}_3$  surface. The dashed circle indicates the Laue circle and the white arrows show the Kikuchi-lines Image taken from [119].

In order to confine the penetration depth of the electrons to the topmost atomic layers, an electron beam with a kinetic energy of  $E = 25 \text{ keV}$  is focused onto the substrate's surface under grazing incident angle  $\alpha < 0.3^\circ$ . Additionally, the horizontally broadened beam spot enables the integration of information across the entire sample. In Fig. 5.3 (a), a sketch of the RHEED working principle is shown. The interaction of incident electrons with the periodic potential of the crystal surface results in a diffraction pattern, which is visualized by a phosphor screen. Most of the electrons scattered at an atomically flat surface are directly reflected, forming the *specular spot*. Moreover, the in-plane symmetry of the crystal lattice causes diffraction maxima. By fulfilling the Bragg condition, the specular spot and the diffraction patterns lie on the Laue circle.

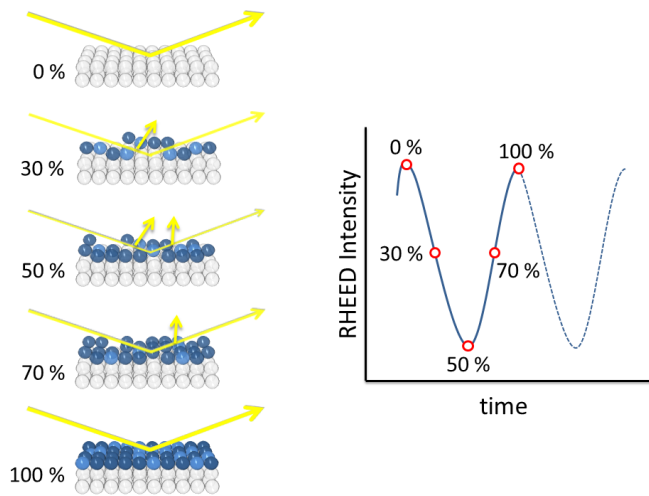


**Figure 5.4:** Intensity evolution of a specular spot for an ideal layer-by-layer growth. With incoming particles up to 50% coverage, the RHEED intensity decreases due to additional scatter centers. Beyond a coverage of 50%, the intensity increases again. Thus, oscillations occur, whereas each maximum corresponds to the growth of a single unit cell. Adapted from [117].

Multiple scattering effects, which consist of elastic and inelastic scattering, lead to the so-called Kikuchi-lines (Fig. 5.3 (b)). More precisely these lines come along with divergent secondary waves produced by inelastic scattering, which are then reflected by the lattice planes of a crystal.

On the basis of the RHEED pattern one can get information about the crystal structure. The analysis of the reflected electron intensity yields information on the roughness of the surface, caused by additional adatom scattering centers. A CCD camera records and digitizes the information coming from the phosphor screen. The integrated intensity of the specular spot is monitored as a function of deposition time. Fig. 5.4 shows the intensity evolution of a specular spot for an ideal layer-by-layer growth, which is relevant for the present work. Considering an atomically flat substrate (no adatoms), the RHEED intensity leads to a maximum. During the growth process of a monolayer, the amount of covering adatoms increases. Due to the increasing number of scattering centers the RHEED intensity decreases until a coverage of 50% is reached. A further increase of the coverage lowers the number of scattering centers, which results in an increased intensity of the reflected electron beam. After the completion of one unit cell, the maximum RHEED intensity is recovered due to the flat surface. Hence, the layer-by-layer growth mode leads to an oscillatory RHEED signal, where each oscillation corresponds to one layer with a thickness of one unit cell. Especially, in the regime of only a few unit cells, RHEED is a well-suited technique to control the thickness of thin films.



## 6.1 Atomic Force Microscopy (AFM)

Atomic force microscopy is a technique used to characterize the surface roughness and the morphology of a sample with high resolution, i.e. a spatial resolution below 100 nm and a vertical resolution down to 1 Å. All surface scans in this work were performed with an Asylum Research Cypher AFM.

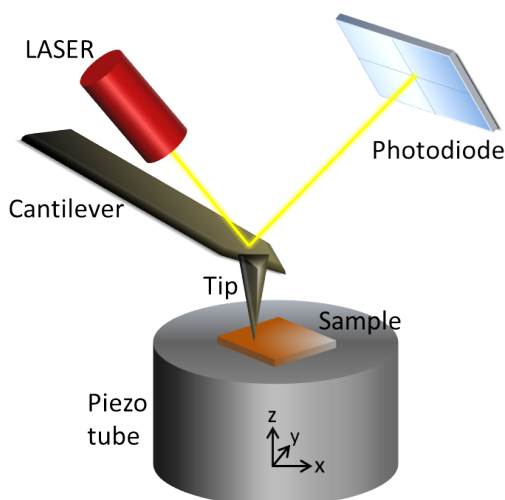


**Figure 6.1:** Schematic description of the atomic force microscopy (AFM) setup. The interaction forces between the tip and the sample cause a bending of the cantilever, which depends on the surface morphology. The respective modulation of the oscillation frequency is measured by a laser focused onto the backside of the cantilever and reflected into a segmented photodiode.

AFM provides a nanoscaled 3D profile of the sample's surface morphology, by measuring Van der Waals forces, dipole-dipole interactions and electrostatic forces between a sharp probe and surface at very short distances (0.2-10 nm). In this work, the AFM images were recorded in tapping mode, where the cantilever is driven to oscillate with a characteristic frequency by a small

piezoelectric element mounted in the AFM tip holder. This frequency is measured by a laser focused onto the backside of the cantilever and reflected onto a segmented photodiode (Fig. 6.1). The interaction between the tip and the sample cause a bending of the cantilever, which depends on the surface morphology. This results in a shift of the cantilever's oscillation frequency. The piezo motor compensates the modulation of the frequency by moving the z-coordinate of the cantilever. By scanning the cantilever across a certain sample region one gets a topographic map of the surface.

As a main quantity for the surface roughness we use the *root mean square* (RMS)  $\sigma_{RMS}$  value

$$\sigma_{RMS} = \sqrt{\sum_i \frac{1}{N} (z_i - \bar{z})^2}, \quad (6.1)$$

where  $z_i$  and  $\bar{z}$  indicate the standard deviation and the average of the surface heights, respectively.

## 6.2 X-Ray Diffraction (XRD)

X-ray diffraction is a widely used tool in order to extract information about the lattice constant and the crystallinity of an epitaxially grown thin film. The analysis of the crystal structure was performed by using a *Philips PW 3020 diffractometer* (Cu-K $_{\alpha}$  X-ray tube,  $\lambda_{K_{\alpha,1}} = 1.540$  ) in Bragg-Brentano geometry. Depending on the incident angle the X-rays are diffracted by the periodic crystal lattice and lead to a characteristic intensity profile as a function of  $2\theta$ . Assuming an ideal infinite periodic crystal structure, we consider two atomic planes P<sub>1</sub> and P<sub>2</sub> separated by a constant distance d Fig. 6.2. Two X-ray beams of wavelength  $\lambda$  and an incident angle of  $\theta$  arrive in phase onto P<sub>1</sub> and P<sub>2</sub> and irradiate the atomic "mirror" planes. The surrounding electrons start to oscillate with the same frequency of the two incident beams and create new wave fronts. While most of the outgoing waves are out of phase, only distinct directions provide constructive interferences. The difference in path length between incoming EF and outgoing EH wave fronts must then be an integer number of wavelengths. This relationship mathematically results in Bragg's law:

$$2d_{hkl} \sin \theta = n\lambda, \quad (6.2)$$

where  $d_{hkl}$  denotes the lattice spacing of the crystal planes with Miller indices (hkl) and n is an integer number. Reflections occur from planes set at angle  $\Theta$  with respect to the incident beam and generate a reflected beam at an angle  $2\Theta$  from the incident beam. The possible d-spacing, defined by the reciprocal indices h, k and l, are determined by the shape of the unit cell. Rewriting Bragg's law results in

$$\sin \theta = \frac{\lambda}{2d}. \quad (6.3)$$

Thus, possible  $\Theta$  values providing reflections are defined by the unit cell dimensions. The intensity of the diffraction pattern depends on the atoms

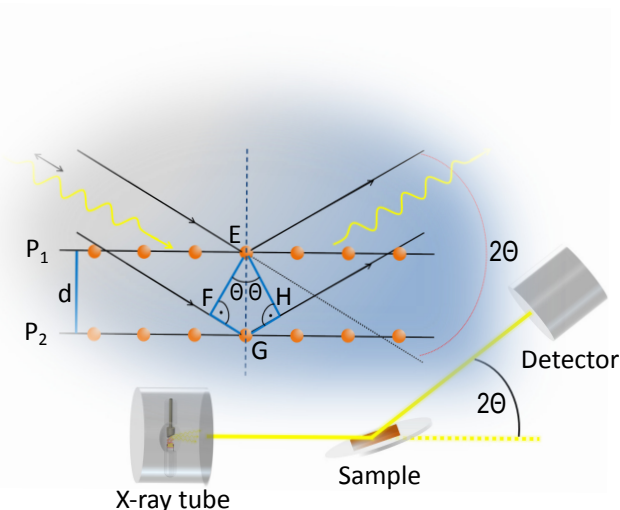


**Figure 6.2:** Scattering geometry of an XRD experiment in Bragg-Brentano geometry. X-rays with a wavelength of  $\lambda$  and an incident angle of  $\theta$  arrive in phase onto the atomic mirror planes. Incoming and outgoing wave fronts must be in phase in order to interfere constructively and to fulfill the Bragg condition.

species and their distribution.

Typically, the lattice constants of the substrate and the respective thin film do not match. Deviations of the out-of-plane lattice constant  $c$  from its bulk-value indicate the incorporation of strain effects, whereas no deviations lead to a fully relaxed film. The finite size of the functional layer causes a broadening of the characteristic intensity peak, which provides, in case of nearly perfect matched lattice constants, the only possibility to distinguish between the thin film and the substrate.

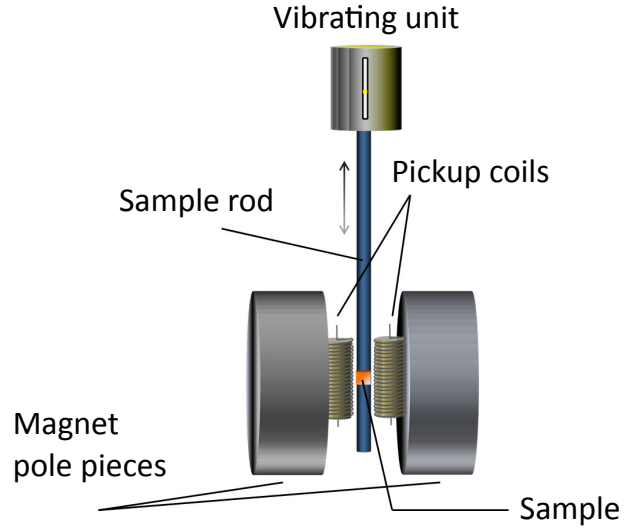
The investigation of parasitic phases can be realized by a full range  $\theta$ - $2\theta$  scan, showing up additional diffraction peaks. From this, XRD is a suitable characterization method in order to check also for a proper growth mode.

### 6.3 Vibrating Sample Magnetometry (VSM)

In order to determine bulk magnetic properties of the samples vibrating sample magnetometry is used. This high precision measurement device from Dynacool, which allows us to resolve magnetic signals down to  $10^{-6}$  emu, exhibits a high temperature oven (300-900 K) and a low-temperature (down to 2 K) cryostat attachment. The operation principle is based on Faraday's law, stating that an electromagnetic force is induced in a coil if there is a change in flux through the coil [15].

The experimental setup is shown in Fig. 6.3. A vibrating unit causes an sinusoidally vertical movement of a connected sample holder rod at a small fixed amplitude. Accordingly, the mounted sample vibrates with the corresponding frequency and amplitude, centered in between of two poles of an electromagnet generating a homogeneous magnetic field  $\vec{H}$ . The poles of the electromagnet are equipped with stationary pickup coils, whereby the

**Figure 6.3:** Schematic description of a vibrating sample magnetometer (VSM). A sample magnetized by a homogeneous magnetic field oscillates between stationary pickup coils. The resulting change in the magnetic flux induces a voltage in the coils, which is proportional to the magnetic moment of the respective sample.



magnetic center of the sample concurs with the symmetry center of the poles. Consequently, the movement of the sample leads to a changing magnetic flux and induces a voltage  $U_{\text{ind}}$  in the coils. Due to Faraday's law, the voltage  $U_{\text{ind}}$  of pickup coils with a flat surface  $A$  and  $n_w$  windings can be written as

$$U_{\text{ind}} = -n_w A \frac{\partial H}{\partial t}. \quad (6.4)$$

In order to magnetize the sample, it has to be brought into the magnetic field  $\vec{H}$ .  $\vec{M}$  is defined as the magnetic moment  $\vec{m}$  per volume unit

$$\vec{M} = \int \frac{d\vec{m}}{dV} dV. \quad (6.5)$$

The magnetic flux density  $\vec{B}$  is determined as

$$\vec{B} = \mu_0(\vec{H} + \vec{M}). \quad (6.6)$$

Applying a constant magnetic field gives

$$\frac{\partial \vec{B}}{\partial t} = \frac{\partial \vec{M}}{\partial t}, \quad (6.7)$$

where the time-dependent magnetic flux originates from the oscillation of the sample relative to the coils. The detected flux change is proportional to the magnetic moment of the sample  $\vec{M}$ , the vibration frequency  $\omega$  and its amplitude  $Z$  and the distance between the sample and pickup coils  $y_0$ . Additionally, the sample geometry influences the induction, which is described by a geometric factor  $G$ . With an increasing number of pickup coils  $n_c$  and windings  $n_w$  the induced voltage increases. All these proportional relations

can be summarized as

$$U_{\text{ind}}(t) \propto -\frac{\vec{M}\omega n_w n_c G \cos(\omega t)}{Y_0}. \quad (6.8)$$

In the present work, this setup is used to measure the in-plane magnetization of the epitaxially grown LSMO thin film with its magnetic easy axis along the (011) direction .



## **Part III**

# **Experimental Results**



---

## Growth and Characterization of $\text{La}_{0.7}\text{Sr}_{0.3}\text{MnO}_3$ Thin Films

---

In the last decades several growth techniques have been developed and optimized in order to produce high quality heteroepitaxial LSMO thin films [120–125], e.g. *RF magnetron sputtering*, *chemical vapour deposition (CVD)*, *molecular beam epitaxy (MBE)*, and pulsed laser deposition. In this thesis, we used the well-established PLD technique providing a reproducible fabrication of single crystalline and epitaxial thin films with a smooth surface. The following chapter gives an insight to the respective growth parameters and covers the structural (AFM, XRD, TEM), electronic (HAXPES) and magnetic characterization (VSM and XMCD) of the LSMO thin films.

### 7.1 PLD Growth Recipe for LSMO

The heteroepitaxial growth of a  $\text{La}_{0.7}\text{Sr}_{0.3}\text{MnO}_3$  thin film on a  $\text{TiO}_2$ -terminated  $\text{Nb(0.5%):SrTiO}_3$  (001) substrate by means of PLD requires a well-adjusted set of growth parameters, such as the substrate temperature  $T_s$ , the distance between target and substrate  $d$ , the laser pulse frequency  $\nu$ , the oxygen background pressure  $\rho$ , and the laser fluence  $J$ . In order to evaluate the correct deposition parameters, we performed both a fluence- and a pressure series, while the remaining parameters were kept constant with  $d = 5.5$  cm,  $T_s = 700^\circ\text{C}$ , and  $\nu = 5$  Hz. The film thickness was set to 20 nm, which should reveal bulk-like properties in case of a stoichiometric composition. After a systematic investigation of the laser fluence and the oxygen background pressure, it turned out that  $J = 3.3$  J/cm<sup>2</sup> and  $\rho = 0.233$  mbar are the optimum deposition parameters, respectively. More details can be found elsewhere [126].

In order to remove surface contamination, the LSMO target was pre-ablated

with 1800 pulses at a laser pulse repetition rate of 10 Hz. The post-annealing was done under an oxygen atmosphere of  $p_{\text{O}_2} = 500$  mbar in the deposition chamber. This process step ensures a saturation of the oxygen content in the LSMO film, which provides the desired stoichiometry.

After switching off the heater power, the specimens were cooled down to room temperature within 1.5 hours. The growth process was recorded by an *in-situ* high-pressure RHEED system, which can be utilized for the determination of the samples' thickness and for the monitoring of the growth mode.

A brief characterization of the high-quality LSMO thin film will be presented in the following.

## 7.2 Structure and Morphology

Fig. 7.1 (a) shows the RHEED specular intensities, recorded during the growth of a 53 unit cells ( $\sim 20$  nm) thick  $\text{La}_{0.7}\text{Sr}_{0.3}\text{MnO}_3$  thin film under perfect deposition parameters (see Sect. 7.1). We observe clear RHEED oscillations indicating a layer-by-layer growth. Further, as each oscillation equals to a complete layer of one unit cell, the film thickness can be controlled precisely.

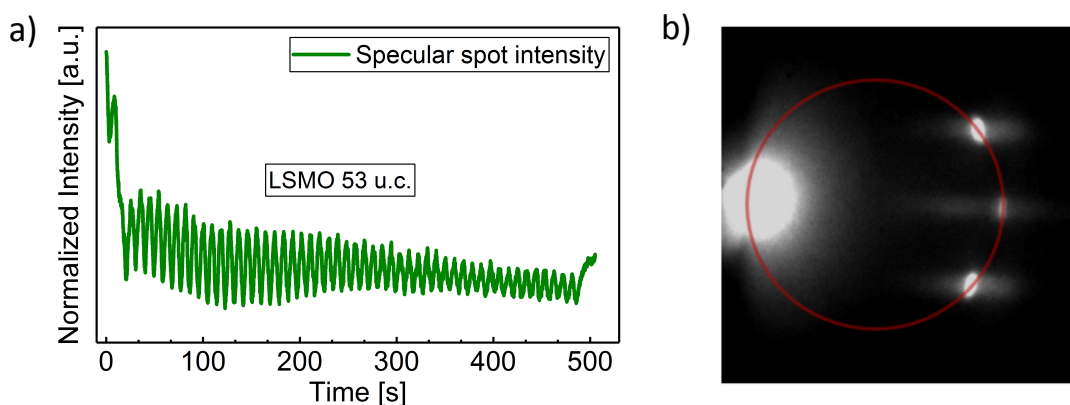


**Figure 7.1:** Monitoring of the thin film deposition performed with a high-pressure RHEED system. (a) Clear RHEED oscillations and (b) sharp first order diffraction peaks lying on the *Laue*-circle (red circle), indicate a layer-by-layer growth and a smooth thin film surface.

The diffraction pattern in Fig. 7.1 (b) shows sharp diffraction spots lying on the *Laue*-circle (red circle), which confirms a two-dimensional layer-by-layer growth and also indicates a smooth surface.

Furthermore, an investigation of the surface morphology, by means of AFM, supports the picture of an atomically flat surface with a roughness of  $\sigma_{\text{RMS}} \sim 0.1$  nm (Fig. 7.2 (a)). A topographical line scan reveals a regular terrace structure with a step height of one unit cell, which is illustrated in Fig. 7.2 (b). The crystal lattice structure of the  $\text{La}_{0.7}\text{Sr}_{0.3}\text{MnO}_3$  thin films was evaluated

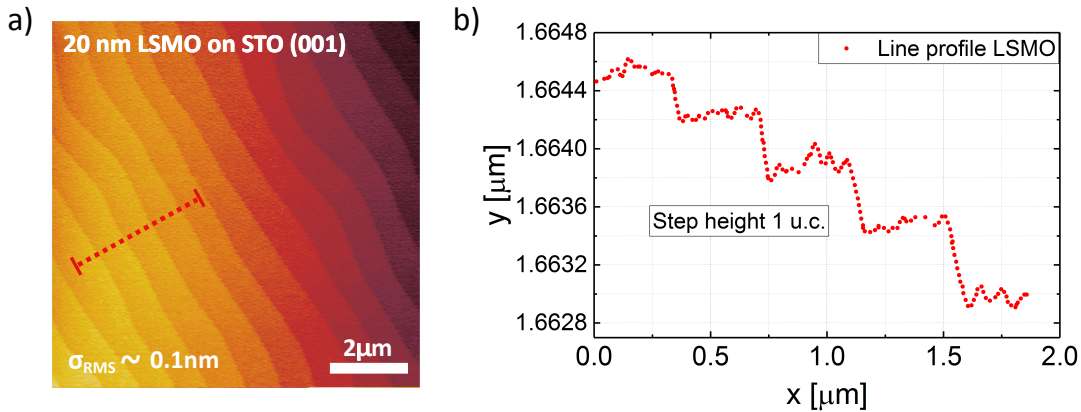


**Figure 7.2:** (a) AFM image of an epitaxially grown LSMO thin film with a thickness of 20 nm, revealing a smooth surface. (b) Height profile shows regular stepped terraces with a step height of one unit cell.

by XRD. Fig. 7.3 shows a  $\theta$ - $2\theta$  scan from  $72^\circ$ -  $75^\circ$ , which shows both the LSMO Bragg peak around the (003) reflection and the STO (003) substrate peaks according to the Cu  $K_{\alpha_1}$  and  $K_{\alpha_2}$  lines. In this scan range we observe a large diffraction intensity and clearly separated LSMO peak, which ensures a proper determination of the Bragg angle and thus the out-of-plane crystal lattice constant. The STO substrate reveals a lattice constant of  $3.905 \text{ \AA}$ , which

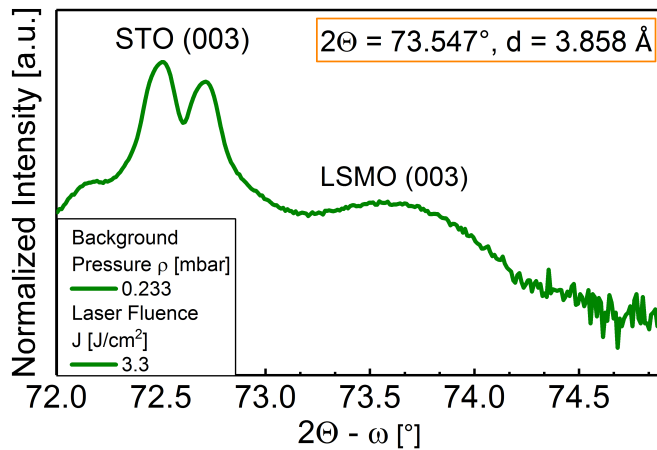


**Figure 7.3:**  $2\theta$ - $\omega$  scan from  $72^\circ$ - $75^\circ$ , which reveals both the LSMO Bragg peak around the (003) reflection and the STO (003) substrate peaks according to the  $K_1$  and  $K_2$  lines. The LSMO peak is located at  $73.547^\circ$ . This leads to an out-of-plane constant of  $3.858 \pm 0.0027 \text{ \AA}$ .

leads to an in-plane crystal lattice mismatch of 0.93% for a relaxed bulk thin film with an out-of-plane constant of  $3.869 \text{ \AA}$ . The LSMO peak is found at  $2\theta = 73.54^\circ$ . Assuming a rhombohedral *pseudo*-cubic structure and applying Eq. 6.2, the out-of-plane lattice constant amounts to  $c_{oop} = 3.858 \pm 0.0027 \text{ \AA}$ . Thus we conclude on a partially strained crystal lattice structure, which exhibits an in-plane tensile strain of -0.28%.

It is worth noting at this point, that these values are a good approximation, but not exact. We assumed a cubic unit cell and a proportional dependence between the out-of-plane and the in-plane crystal lattice constant. However, due to the limit of the elastic modulus of the respective material, the unit cell

volume generally is not conserved in a strained film. A quantity of the elastic property of a material is the *Poisson* coefficient  $\nu$ , as it is defined in Eq. 7.1:

$$\nu = \frac{\epsilon_c}{\epsilon_c - 2\epsilon_{a,b}}. \quad (7.1)$$

Here,  $\epsilon_{a,b}$  and  $\epsilon_c$  denote the in-plane and out-of-plane ratios, respectively. For most materials,  $\nu$  ranges between 0 and 0.5. For the LSMO thin film we calculate a value of  $\nu = 0.34$ . The behaviour of the unit cell volume can be described by the following expression

$$\frac{\Delta V}{V_0} = \epsilon_a + \epsilon_b + \epsilon_c + \mathcal{O}(\epsilon_i^2) = 2\left(1 - \frac{\nu}{1 - \nu}\right)\epsilon_{a,b}, \quad (7.2)$$

where  $\Delta V = V - V_0$  indicates the change of the unit cell volume ( $V$ ) with respect to the bulk value  $V_0$  [127]. Conservation of the unit cell is only achieved for  $\nu = 1/2$ . For all other values of  $\nu$ , a reduced or enlarged unit cell volume is expected for compressive or tensile strain, respectively. More detailed information about the elastic deformation of heteroepitaxial thin films can be found elsewhere [128].

### 7.3 Electronic Structure

In order to investigate the chemical and electronic properties of  $\text{La}_{0.7}\text{Sr}_{0.3}\text{MnO}_3$  thin films, hard X-ray photoelectron spectroscopy has been performed at PE-TRA III in Hamburg. HAXPES offers a large information depth, which allows us to probe the electronic structure of a sample with true bulk sensitivity.

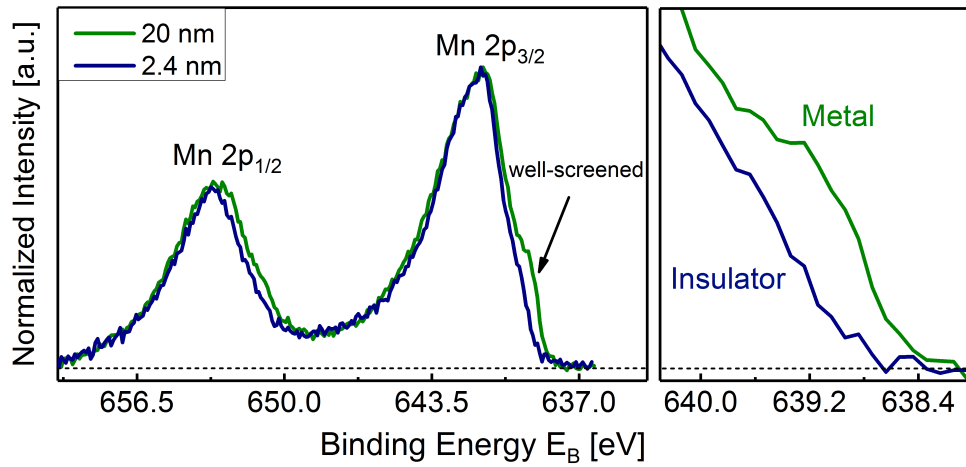
Since the Mn  $2p$  and Mn  $3s$  core levels show characteristic spectral features, which provide information about the conductivity and the valence state of the manganese, they will be discussed in further detail. All HAXPES measurements were performed at room temperature and a photon energy of  $h\nu = 4$  keV.

The Mn  $2p$  core level is plotted in Fig. 7.4 and reveals two distinct peak intensities at  $E_{Bin} = 641$  eV (Mn  $2p_{3/2}$ ) and at  $E_{Bin} = 653$  eV (Mn  $2p_{1/2}$ ). The distinct intensities of the core levels are a consequence of the spin-orbit splitting.

The Mn  $2p_{3/2}$  peak exhibits a low-binding energy shoulder at  $h\nu \sim 639$  eV. This feature is explained by the screening of the Mn  $2p$  core hole by the itinerant  $e_g$  valence electrons from neighbouring Mn  $3d$  states [129, 130]. This structure has been termed "well-screened" feature by S. Schlüter *et al.* [131].

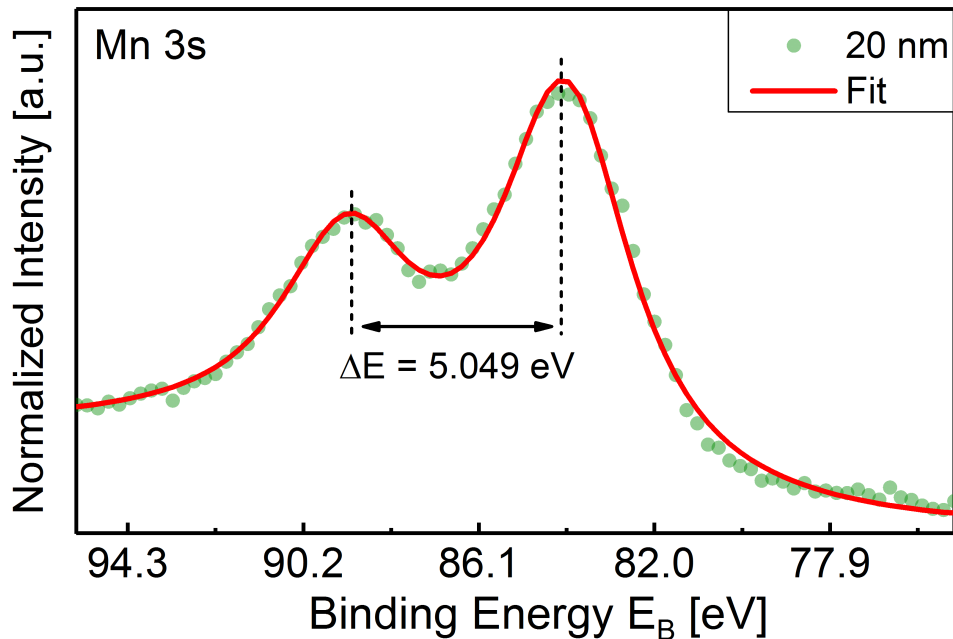
As it can only be observed for the metallic phase, it is an alternative probe of the existence of conduction electrons. Subsequently, the samples showing a well-developed screening feature are supposed to have a perfect stoichiometry, providing an enhanced conductivity due to a well-established double exchange mechanism.

Fig. 7.5 shows the Mn  $3s$  core level displaying two main peak intensities at



**Figure 7.4:** Mn 2p core level spectra of  $\text{La}_{0.7}\text{Sr}_{0.3}\text{MnO}_3$  thin films with a thickness of 2.4 nm and 20 nm. The measurements were performed at room temperature and a photon energy of 4 keV. Right: Zoom into the well-screened feature indicating a conducting state.

$E_{Bin} = 84.25$  eV and  $E_{Bin} = 89.3$  eV. Since the orbital angular momentum of s electron states amounts to  $l = 0$  here, the split core level cannot be explained by the spin-orbit coupling. The spectral splitting of the Mn 3s core level is rather caused by the exchange coupling between the 3s hole and the 3d electrons. After photoionization, two states arise due to the  $3d - 3s$  exchange interaction:



**Figure 7.5:** Mn 3s core level spectra of  $\text{La}_{0.7}\text{Sr}_{0.3}\text{MnO}_3$  thin films showing spectral splitting due to an exchange coupling between the 3s hole and the 3d electrons. The measurements were performed at room temperature and a photon energy of 4 keV.

one high-spin state at a lower binding energy with the spins of the 3s and the 3d electrons parallel, and a low-spin state at a higher binding energy with antiparallel spin alignment. There is a linear correlation between the spectral splitting and the oxidation state of Mn, as it is described in the following equation:

$$\Delta E = (2S + 1)J_{3s-3d}^{eff} \quad (7.3)$$

where S denotes the total spin momentum and  $J_{3s-3d}^{eff}$  the effective exchange integral between the Mn 3s and Mn 3d states.

Galakhov *et al.* performed a spectral analysis on several manganese oxides showing the Mn 3s fingerprints for a series of different manganese valencies [132]. These results were used to deduce a linear relationship between the valency  $\nu_{Mn3s}$  and the exchange splitting  $\Delta E$ :

$$\nu_{Mn3s} = 9.67 - 1.27 \cdot \Delta E. \quad (7.4)$$

The peak positions were determined by fitting a doublet function after background subtraction, which results in an exchange splitting of  $\Delta E = 5.049$  eV. This value corresponds to a valency of  $\nu_{Mn3s} = 3.257 \pm 0.018$ . According to our expectations of a formal valency of 3.3 this result fits very well.

## 7.4 Magnetic Properties

The magnetic behaviour of LSMO thin films has been widely studied on the basis of their rich phase diagram and promising properties like the magnetoresistive effect were reported [133, 134]. Moreover, we extensively investigated the magnetic and electronic properties as a function of the film thickness and determined both the ferromagnetic-to-antiferromagnetic and the metal-to-insulator phase transition. However, in the scope of this work, the thickness dependent properties will not be discussed in further detail as they can be found elsewhere [126]. A brief overview of the magnetic characterization is presented in the following.

### 7.4.1 Vibrating Sample Magnetometry (VSM)

**Hysteresis Loop** The magnetic properties of the 20 nm thick  $\text{La}_{0.7}\text{Sr}_{0.3}\text{MnO}_3$  thin film were measured by a vibrating sample magnetometer (VSM). The sample was probed along the in-plane magnetic easy axis, which goes along the (011) direction, due to its magneto-crystalline anisotropy. The sample was cooled down to a temperature of 10 K in order to exploit a sufficiently large magnetic moment. Since the ionic composition of the investigated samples ( $\text{La}_{0.7}^{3+}\text{Sr}_{0.3}^{2+}(\text{Mn}_{0.7}^{3+}\text{Mn}_{0.3}^{2+})\text{O}_3$ ) reveals a mixed valency of the manganese, which consists of 70 % of  $\text{Mn}^{3+}$  ( $4 \mu_B$ ) and 30 % of  $\text{Mn}^{4+}$  ( $3 \mu_B$ ), the total magnetic moment in an ideal unit cell amounts to  $3.7 \mu_B$ .

Fig. 7.6 shows a magnetic hysteresis loop, which describes the response of

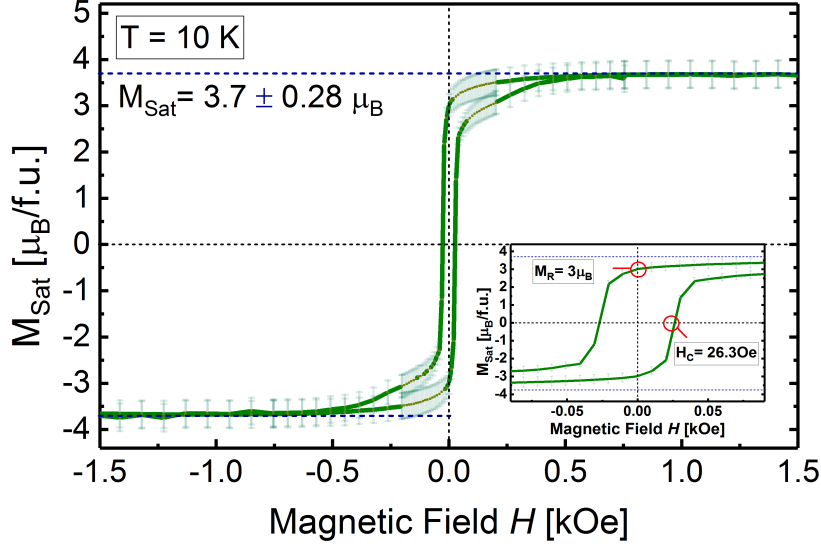


**Figure 7.6:** VSM hysteresis loop of a 20 nm thick  $\text{La}_{0.7}\text{Sr}_{0.3}\text{MnO}_3$  thin film measured at 10 K. The external magnetic field  $H$  was applied along the (011) easy-axis. The inset shows a detailed view of the magnetic remanence  $M_R$  and the coercive field  $H_C$ .

the samples' magnetic moment  $M$  to the applied magnetic field  $H = \pm 1.5$  kOe (0.15 T). The measured sample shows a saturation magnetization of  $M_{\text{Sat}} = 3.7 \pm 0.37 \mu_B$ . Further, the coercive field  $H_C$  and the magnetic remanence amount to 26.3 Oe and  $1.4 \mu_B$ . These results are consistent with the values reported in previous studies [135].

**Temperature dependence** Another method to investigate the magnetic properties is to measure the saturation magnetization as a function of temperature, while the Curie temperature  $T_C$  marks the phase transition between the ferromagnetic- and the paramagnetic (FM-PM) state (Fig. 7.7). The largest  $T_C$  for  $\text{La}_{0.7}\text{Sr}_{0.3}\text{MnO}_3$  was reported for a LSMO single crystal, which reveals a value of 370 K [136]. Typical values obtained for LSMO thin films ( $\sim 20$  nm) range between 340 K and 350 K [137, 138].

Our sample was field-cooled from 300 K to 10 K under the application of an external magnetic field  $H$  of 1 kOe. The  $M(T)$  curve was measured at  $H = 500$  Oe and exhibits a Curie temperature of  $T_C = 347$  K with a sharp FM-PM phase transition.

The  $T_C$  value obtained here and in literature for thin films considerably differs from the bulk value of 370 K. The reduction of the Curie temperature is related to the partially in-plane tensile strained crystal structure of the epitaxially grown LSMO thin film. The tetragonal lattice distortion induced by the lattice mismatch between the LSMO thin film and the STO substrate separates the  $e_g$  state into two energy levels  $d_{x^2-y^2}$  and  $d_{3z^2-r^2}$ , according to the Jahn-Teller-effect (see Sect. 3.2.1). In the present case of an in-plane tensile strain the  $d_{3z^2-r^2}$  orbital is lifted to a higher energy level. The double exchange

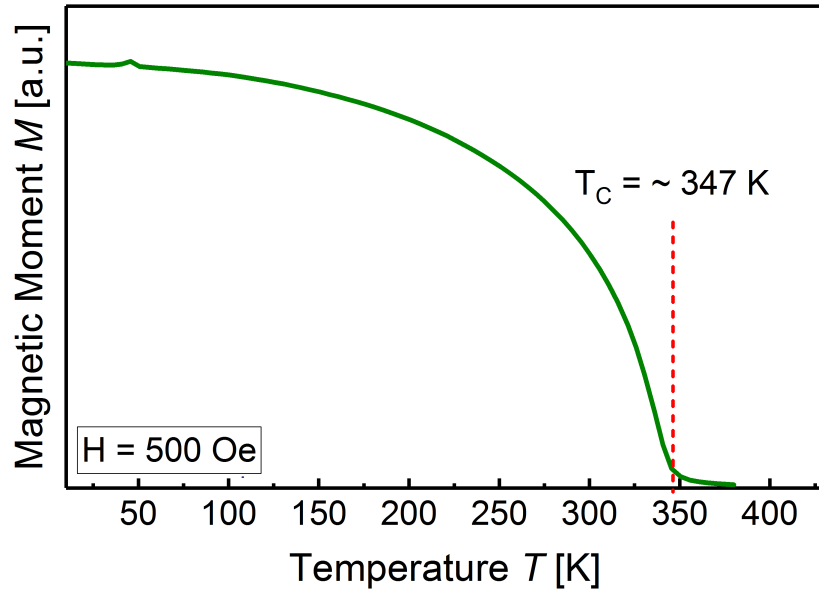


**Figure 7.7:** Magnetic moment  $M$  of a 20 nm thick  $\text{La}_{0.7}\text{Sr}_{0.3}\text{MnO}_3$  thin film as a function of the temperature  $T$  measured at  $H = 500$  Oe. The sample was field cooled at  $H_C = 1$  kOe from 300 K to 10 K along the (011) direction before the measurement was performed.

mechanism, which is responsible for the ferromagnetism in LSMO, occurs between the  $d_{3z^2-r^2}$  orbitals of the  $\text{Mn}^{3+/4+}$  cations and the  $p_z$  orbitals of the oxygen ions (see Sect. 3.3.3). Thus, it becomes apparent that the system has to overcome a certain energy barrier to interact with the  $e_g$  energy level, which finally leads to a reduction of the Curie temperature. A further reason is the natural occurrence of defects and the broken symmetry at the interface and the surface, which might lead to compositional inhomogeneities.

So far, the results presented confirm an atomically flat surface and a single crystalline thin film, which was analyzed by AFM and XRD. Further, the investigation of the electronic structure by means of HAXPES indicates a conductive state due to the appearance of the "well-screened" feature at the Mn  $2p$  core level. From the Mn  $3s$  exchange splitting we estimate a valency of  $\text{Mn}^{3.257+}$ . Finally, the magnetic characterization by VSM results in a saturation magnetization of  $M_{Sat} = 3.7 \pm 0.37 \mu_B$  and a Curie temperature of  $T_C = 347$  K. In line with literature these values confirm that we have determined the right deposition parameters providing a high quality and stoichiometric LSMO thin film growth.

The following experimental results presented in this thesis are based on a 10 nm thick LSMO thin film. Whereas a 20 nm thick LSMO film leads to a partially strained crystal lattice, for a thickness of 10 nm we observe a fully strained structure, which entirely adapts the in-plane constant of the Nb:STO substrate ( $c_{ip} = 4.905$ ). Due to the strong correlation between localized transition metal valence electrons, the electronic and magnetic properties are

sensitive to defects like strain [139, 140]. Hence, the saturation magnetization decreases from  $M_{Sat} = 3.7 \pm 0.37 \mu_B$  (partially strained) to  $M_{Sat} = 3.4 \pm 0.34 \mu_B$  (fully strained). Both a structural characterization of a 10 nm thick LSMO thin film by reciprocal space mapping and a brief summary of the magnetic behaviour as a function of the film thickness can be found in App. A and B. Subsequently, a further characterization technique is used in order to determine the magnetic properties. The XMCD analysis provides an element-selective measure of the magnetic properties and particularly reveals local information of the surface state, which is discussed in the following.

### 7.4.2 X-Ray Magnetic Circular Dichroism

In a last step of the pre-characterization, we analyze the XMCD signal across the Mn  $L_{3,2}$ -edge to do both a quantitative investigation of the magnetic spin and orbital moment and an identification of the magnetic spectral fingerprint of a 10 nm thick  $\text{La}_{0.7}\text{Sr}_{0.3}\text{MnO}_3$  thin film at low temperatures. Since the following data set was the only one measured at the beamline endstation 6.3.1 of the Advanced Light Source (ALS), a short description of the respective experimental setup will be given in the next paragraph. Subsequently, the individual analysis steps of the XMCD measurement are discussed in detail.

#### Experimental Setup

The XMCD measurement presented in this section was recorded at the bending magnet beamline endstation 6.3.1 at the ALS in Berkeley, USA, which provides elliptically polarized radiation with degrees of polarization of  $60 \pm 5 \%$ . The  $\text{La}_{0.7}\text{Sr}_{0.3}\text{MnO}_3$  sample was attached to a cryostat and was cooled down to a temperature of 20 K. The XMCD spectrum was obtained by applying a magnetic field of 0.5 T along the incident beam direction, which was realized by a liquid helium cooled superconducting magnet in a Helmholtz coil geometry, as depicted in Fig. 7.8. The Mn  $L_{3,2}$ -edge was investigated by surface sensitive total electron yield at a fixed angle of  $30^\circ$  between the beam axis and the surface plane of the sample. The incoming photon beam intensity  $I_0$  has been used to normalize the measured absorption spectra.  $I_0$  was determined by a gold grid, which was placed in the X-ray beam path generating a photo-current that is proportional to the intensity of the beam and the energy dependent photoionization cross section of the gold mesh.

#### XMCD Analysis Step-by-Step

In order to investigate the spin-averaged XAS and the XMCD, the absorption is measured as a function of the photon energy both for parallel and antiparallel alignment of the photon spin and the magnetization of the sample. The absorption spectra of the Mn  $L_{3,2}$ -edge shown in Fig. 7.9 are already normalized to the incoming photon beam intensity  $I_0$ . The remaining linear background, which is assigned to the energy-dependent photoionization cross section, is

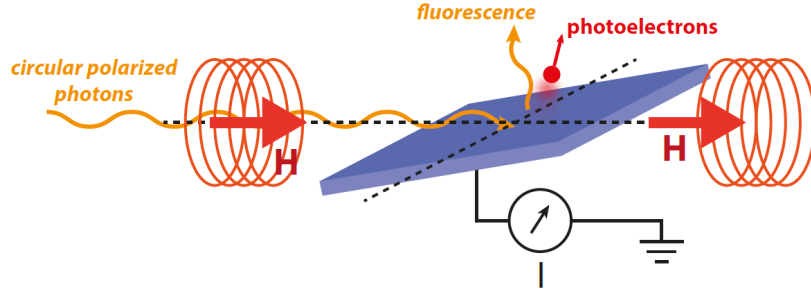


**Figure 7.8:** Experimental geometry of the XMCD measurement: The magnetic field was applied along the incident beam direction. The XAS was measured in TEY mode. Taken from [141].

fitted by a linear function in the pre-edge region and subsequently removed by subtraction. Worth mentioning here, the choice of the right pre-edge range for background subtraction is crucial for a proper analysis. Particularly, in case of low XMCD signals the determination of the background is not trivial, since the linear regression is significantly influenced by noise. This topic will be discussed in more detail in Ch. 8.2.3. However, the signal-to-noise-ratio of the here presented absorption spectrum is large and the resulting deviations in the XMCD signal by choosing different pre-edge ranges can be neglected. After the background subtraction the absorption spectra are normalized to a point of the linear regression of the post-edge region ( $h\nu = 671$  eV). From here, the isotropic XAS, the "white line", can be determined by

$$\mu(E) = \frac{1}{2}(\mu^+(E) + \mu^-(E)) \quad (7.5)$$

According to the definition in Eq. 4.13 the XMCD is then given by

$$\Delta\mu(E) = \mu^+(E) - \mu^-(E). \quad (7.6)$$

The spectra consist of  $2p \rightarrow d$  (resonance-like peaks),  $2p \rightarrow s$  and  $2p \rightarrow$  continuum (step-like increase) dipole transition contributions. In order to employ the sum rules the transitions into  $s$  and  $p$  states ( $\sim 2\%$ ) and into the continuum have to be removed. The latter can be approximated by an *ad hoc* step function of the Fermi-type [142]:

$$\mu_{step} = \frac{3}{2} \left( 1 - \frac{2}{3} \frac{1}{1 + e^{(E-E_{L_3})/\delta}} - \frac{1}{3} \frac{1}{1 + e^{(E-E_{L_2})/\delta}} \right) \quad (7.7)$$

where  $E_{L_3}$  and  $E_{L_2}$  are the energy positions of the edge jumps with respect to the edge positions, while  $\delta$  indicates the step width. The height of each individual step is set to  $2/3$  ( $L_3$ -edge) and  $1/3$  ( $L_2$ -edge) of the height of the XAS spectrum. The step positions are  $E_{step,L_3} = 641.1$  eV and  $E_{step,L_2} = 651.7$  eV, as depicted in Fig. 7.10. After the subtraction of the step function from the isotropic absorption spectrum we integrate over the whole L-edge in order to

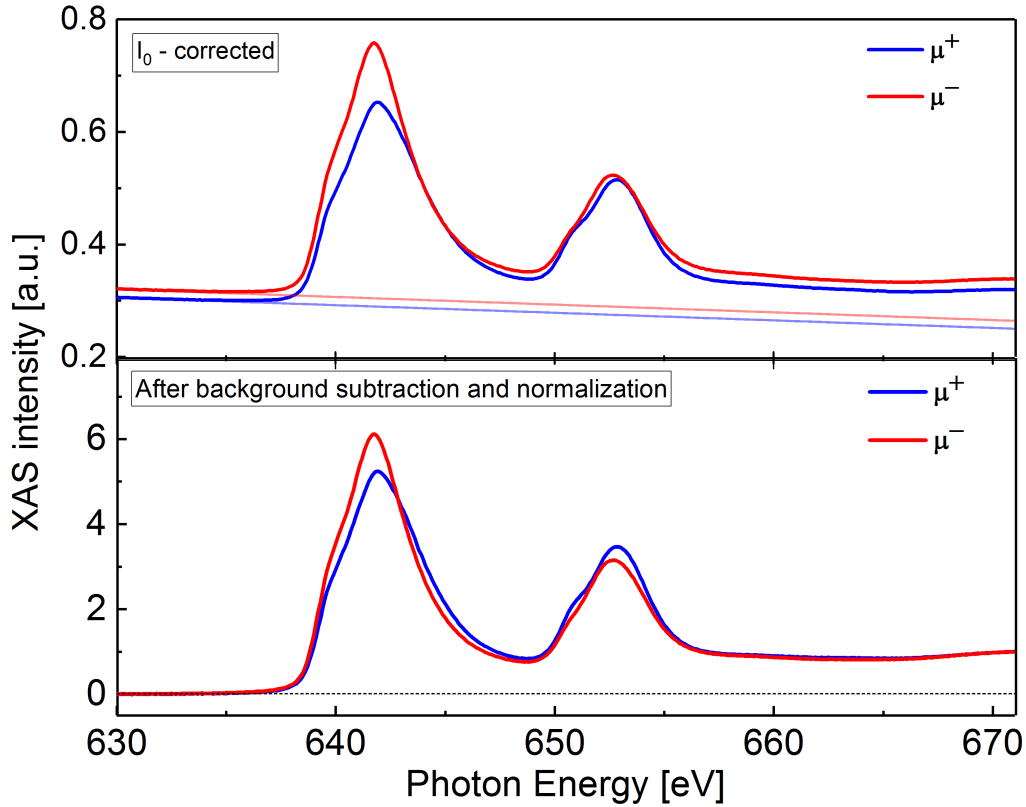


**Figure 7.9:** Data treatment of X-ray absorption spectra  $\mu^+$  and  $\mu^-$  for XMCD analysis. (top) Raw XAS data are normalized to the incoming photon beam intensity  $I_0$ . The linear background of each XAS is shown (transparent line). (bottom) Absorption spectra after linear background subtraction and normalization to the pre-edge region.

determine the value  $r$  referring to Eq. 4.14. Subsequently, the values  $p$  and  $q$  are calculated by integrating over the  $L_3$ -edge and  $L_{3,2}$ -edge areas of the XMCD curve, respectively (Eq. 4.14). The  $L_3$  and  $L_2$ -edges are considered to be between  $h\nu(L_3) = 630 \text{ eV} - 648.7 \text{ eV}$  and  $h\nu(L_2) = 648.7 \text{ eV} - 671 \text{ eV}$ . All input parameter and according results of the quantitative analysis are presented in Table 7.1.

The calculated total magnetic moment  $m_{l+s} = 3.490 \pm 1.047 \mu_B$  corresponds to the measured saturation magnetization value  $M_{Sat} = 3.4 \pm 0.34 \mu_B$  determined by VSM. The number of unoccupied final states in the valence shells  $n_h$  (3d electron holes), which consists of  $n$  electrons is given by  $(4l + 2 - n)$ . Thus, considering a Mn valence state of 3.3 per formula unit one gets  $n_h = 6.7$ .

Besides the orbital and spin magnetic moment there is a further quantity, namely, the ratio of orbital to spin moment  $m_l/m_s$ . Here, uncertainties of the number of holes  $n_h$  and the degree of polarization  $P_c$  cancel out.

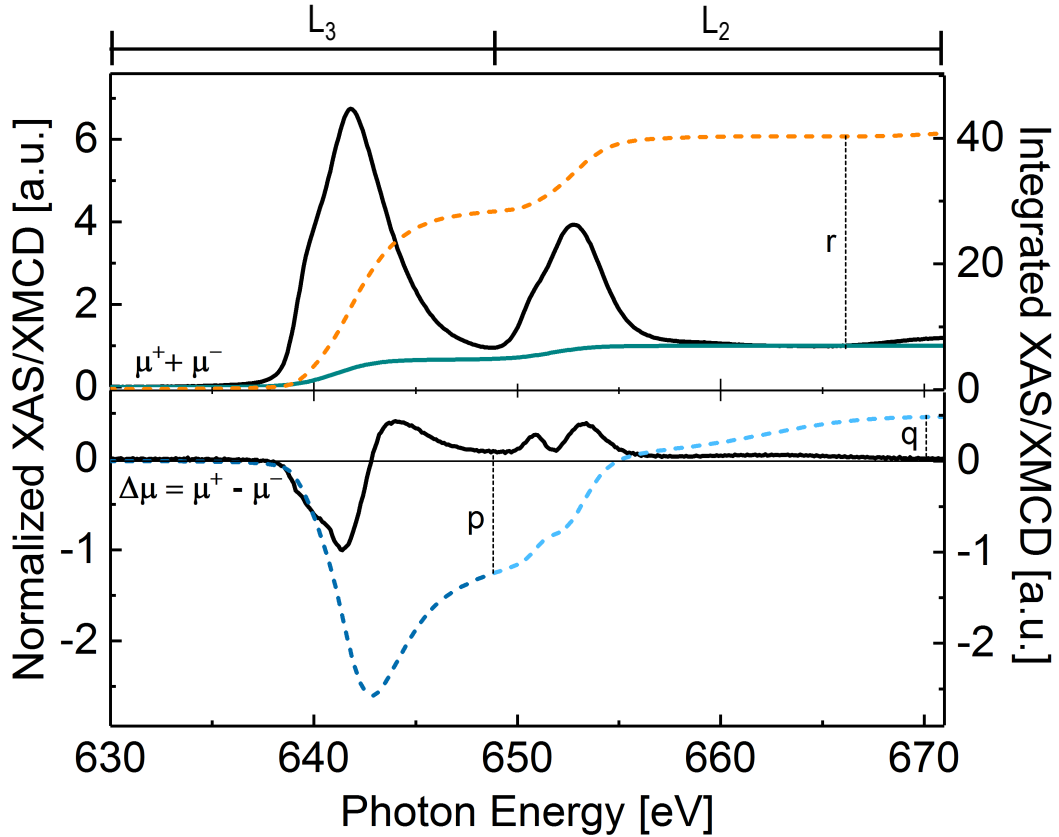


**Figure 7.10:** Illustration of the application of the sum rules to the measured XMCD data of the Mn  $L_{3,2}$ -edge. (top) Isotropic absorption spectrum (black solid curve) with the respective integration  $r$  (dashed orange curve) and the step function according to the continuum background contribution (solid petrol curve). (bottom) The XMCD curve (black solid line) and the integrals  $p$  and  $q$  (blue dashed lines).

$p$	$q$	$r$	$\vartheta$ [°]	$P_C$	$m_l$ [ $\mu_B$ ]	$m_s$ [ $\mu_B$ ]	$m_{l+s}$ [ $\mu_B$ ]	$m_l/m_s$
-1.241	0.485	40.791	30	0.6	$0.523 \pm 0.156$	$2.967 \pm 0.890$	$3.490 \pm 1.047$	0.176

**Table 7.1:** Input parameters for the quantitative XMCD analysis and the resulting orbital, spin and total magnetic moment  $m_l$ ,  $m_s$  and  $m_{l+s}$ . The ratio of orbital to spin moment  $m_l/m_s$  gives a quantity, which is dependent from  $n_h$  and  $P_C$ .

### 7.4.3 Conclusion

In summary, this chapter shows that we have established a well-working growth procedure for LSMO thin films utilizing the pulsed laser deposition. The growth process was monitored by an *in situ* RHEED system, which enables a precise control of the film thickness. Moreover, it was used to confirm

a two dimensional layer-by-layer growth. Subsequently, the morphology and the crystal structure were characterized by AFM and XRD revealing an epitaxial, single crystalline film and an atomically flat surface. The investigation of the electronic structure were performed with HAXPES. The appearance of the well-screened feature at the Mn  $2p$  core level indicates a conductive state and from the Mn  $3s$  exchange splitting we deduce a Mn valence state of  $\nu_{Mn3s} = 3.257 \pm 0.018$ . The VSM was used to investigate both the Curie temperature and the saturation magnetization moment along the magnetic (011) easy axis, which amounts to  $T_C = 347$  K and  $3.7 \pm 0.37 \mu_B/\text{f.u.}$  ( $3.4 \pm 0.34 \mu_B/\text{f.u.}$ ) for a 20 nm (10 nm) thick LSMO thin film. Finally, a qualitative and quantitative element-selective XMCD analysis of a 10 nm thick film reveals a typical XMCD fingerprint of LSMO and a total magnetic moment of  $m_{l+s} = 3.490 \pm 1.047 \mu_B$ , which reproduces the result obtained by VSM.



---

## Voltage-Driven Modification of Chemical and Physical Properties in $\text{La}_{0.7}\text{Sr}_{0.3}\text{MnO}_3$ Thin Films

---

This chapter starts with an electrical characterization of the grown LSMO thin film, which is essential for the further use as resistive memory (Sect. 8.1). The macroscopic investigation of the switching characteristics serves as a pre-study for the following microscopic investigation by LC-AFM and PEEM, presented in Sect. 8.2. An accurate nanoscale analysis of the correlation between electronic structure, chemistry and magnetism is required to establish a solid understanding and controlling the physical properties at the nanoscale and thus to realize a new generation of magneto-ionic nano-devices.

### 8.1 Resistive Switching in $\text{La}_{0.7}\text{Sr}_{0.3}\text{MnO}_3$

The switching experiment performed on  $\text{La}_{0.7}\text{Sr}_{0.3}\text{MnO}_3$  thin films is realized in a vertical geometry and in ambient atmosphere. The voltage was applied to the surface using a tungsten tip (tip radius  $r_{tip} \approx 6 \mu\text{m}$ ) while the Nb:STO substrate was set to ground, as illustrated in Fig. 8.1. The voltage-sweep measurements were performed by a Keithley 4200-SCS measurement unit, which allows one to detect currents down to the nA regime.

#### 8.1.1 Voltage Sweep Measurements

The I-V cycles presented here were performed by increasing the voltage with a constant rate up to a previously defined maximum voltage. The value of the voltage increase is set to 20 mV per step. Further, the respective voltages are

held for 5 ms before voltage and current are measured. All resistances shown in this section are measured at a read voltage  $V_{rd} = 0.5$  V.

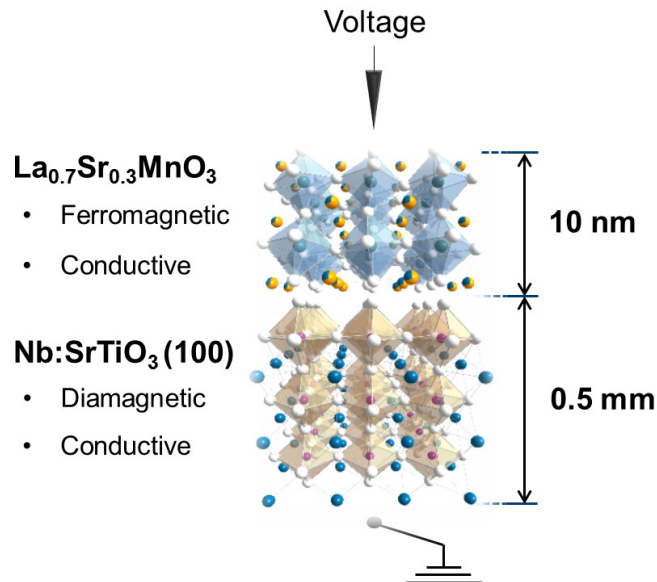


**Figure 8.1:** Sketch of the vertical geometry of the resistive switching experiment. A voltage is applied perpendicular to the LSMO surface normal utilizing a tungsten tip. The Nb:STO substrate is set to ground.

**Determination of Switching Voltage** Before discussing the switching characteristics and underlying physics, first, one has to determine the optimal switching parameters. Here, optimal parameters means reproducible resistance values for the HRS and the LRS for at least 10 cycles. Further, we want to evaluate the maximum resistance ratio of the LRS and the HRS, which is also called ON/OFF ratio. Therefore, different SET and RESET voltages were investigated. Exemplary resistive switching curves and their resistance changes for different voltage sets are illustrated in Fig. 8.2. The adaption of the voltage amplitudes within the positive and negative branches was performed between 1 V and 6 V, and -1 V and -6 V. Voltage amplitudes beyond +6 and -6 V cause an electrical breakdown, which leads to the destruction of the device at the position of the tip electrode.

Fig. 8.2 (a)-(c) show representative cases for non-perfect voltage sets, which is indicated by a drift of the respective HRS and LRS resistance values over 10 cycles. A quite stable behaviour of the resistive states can be obtained in Fig. 8.2 (d) due to a well-adapted voltage set of +5 V/-5 V. A summary of both the resistance values for the HRS and the LRS, and of the ON/OFF ratio for the right switching parameters is given in Table 8.1.

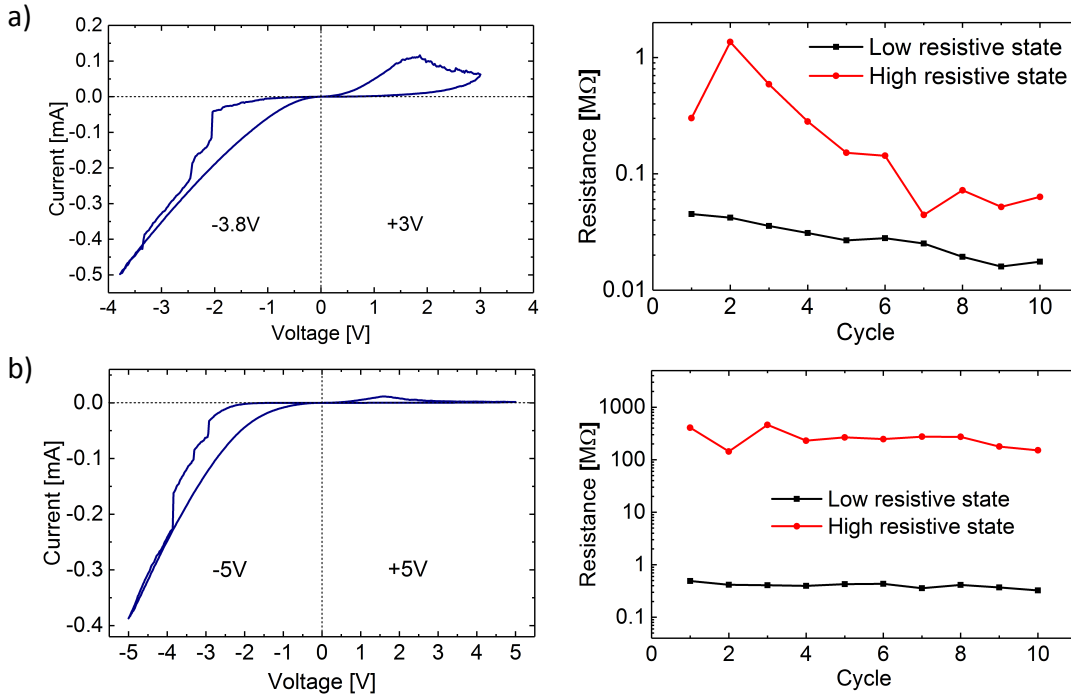


**Figure 8.2:** Evaluation of the optimal switching voltages. (a) shows a drift of the resistivities for the HRS and the LRS, which indicates a non-optimal adaption of the respective voltage-set. (b) shows stable ON and OFF states over 10 cycles.

Parameter	Value
LRS / $\text{M}\Omega$	$0.41 \pm 0.04$
HRS / $\text{M}\Omega$	$257.41 \pm 55$
ON/OFF ratio	602.16

**Table 8.1:** Median values of both the LRS and the HRS, and the ON/OFF ratio for the right switching amplitudes +5 V / -5 V.

**Bipolar Resistive Switching** After the evaluation of the correct switching voltages we focus on the description and the interpretation of the I-V curve. Fig. 8.3 shows the resistive switching behaviour of a LSMO thin film plotted in a linear (a) and a semi-logarithmic scale (b). Since the switching direction depends on the polarity of the write voltage  $V_{wr}$ , the plotted curves describe a bipolar resistive switching mode. Further, following the arrows of the switching direction, we obtain a counter-eightwise hysteresis [26].

Pristine LSMO reveals a conductive state. Sweeping towards positive voltages leads to a metal-to-insulator phase transition reaching the high resistive state (HRS). The gradual RESET begins at +2.3 V. Sweeping back to negative voltages recovers the conductive behaviour and leads to a low resistive state (LRS). The sharp SET point, which indicates the transition from HRS to LRS

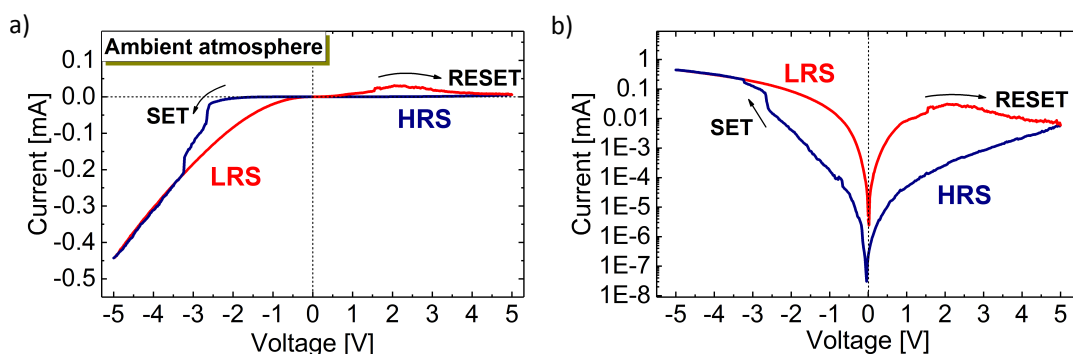


**Figure 8.3:** The same bipolar resistive switching curves in a linear (a) and a semi-logarithmic (b) scale.

is found at -2.6 V. In order to understand the SET and RESET transitions in LSMO, the driving mechanisms will be discussed in more detail.

As a valence change material LSMO has been the object of several studies. There is a broad consensus on the dependence of the local resistivity on the concentration of oxygen vacancies (VO) [24, 25, 143]. In Fig. 8.4 there is a sketch, which illustrates the voltage-directed migration of VO. Applying a positive voltage induces a migration of the negatively charged oxygen ions to the surface, due to the attractive force. Thereby, positively charged VO are repelled into the bulk. Subsequently, a surface exchange process leads to a release of the oxygen, which is driven by the gradient of the chemical potential of oxygen across the LSMO/ambient atmosphere interface [144]. Since the oxygen anions mediate the exchange interaction of the itinerant electrons between the  $\text{Mn}^{3+}$  and the  $\text{Mn}^{4+}$  cation, a missing oxygen between them leads to a disturbed double-exchange mechanism. Consequently, the resistivity decreases. By exceeding a certain VO concentration one enters the metal-to-insulator transition and the HRS (RESET). Subsequently, an application of a negative voltage provides an incorporation of oxygen anions into the thin film from the ambient atmosphere, while VO are released. The conductivity increases with oxygen concentration and reaches the LRS (SET).

Next, it has to be clarified, why there is a "sharp" SET and a "gradual" RESET. Often, a sharp transition is related to a filamentary resistive switching type [26], which we also assume here. Now, applying a negative voltage leads to a decrease of the VO concentration within the filament and an increase of its conductivity. This is accompanied with an enhanced electric field and Joule heating, which induces a self-accelerating migration of VO, which supports a sharp phase transition from insulator to metal.

Sweeping back towards positive voltages leads to an incorporation of VO and an increase of the resistivity. Thus, the decreasing current causes a reduction of joule heating and hampers the self-accelerating effect [145]. In relation to the sharp SET, which is assigned to the fast release of VO, the RESET reveals a slow increase of VO and therefore describes a gradual transition to the HRS.

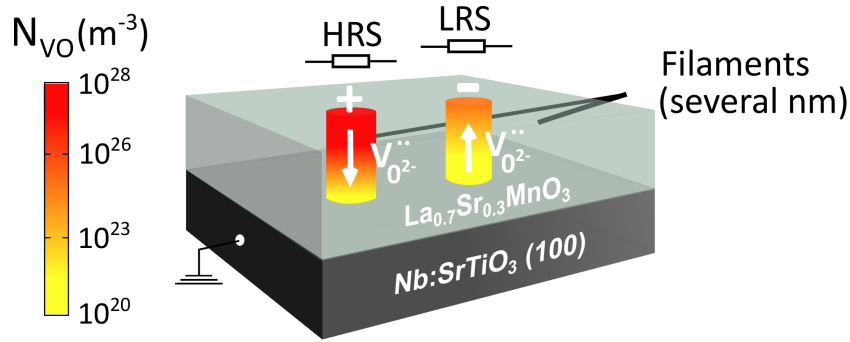


**Figure 8.4:** Sketch of the voltage-directed oxygen migration within filaments of several nanometers in a LSMO thin film. A positive voltage applied to the surface attracts oxygen anions from the bulk and repels VO into the bulk. The resulting large VO concentration leads to a transition from metal to insulator and thus to the HRS. A negative voltage provides an incorporation of oxygen anions and thereby a release of VO, resulting in a LRS.

Besides the bipolar resistive switching behaviour and its characteristic SET and RESET points the switching cycle contains further information. The semi-logarithmic plot reveals a wide opening of the I-V hysteresis. At a read voltage  $V_{rd} = 0.5 \text{ eV}$  we calculate an ON/OFF ratio of  $\sim 600$ . The large difference between the LRS and the HRS cannot be explained solely by a change of the resistivity within the filaments. A significant contribution is assigned to the distribution of the oxygen vacancies at the interface between the LSMO half-metal and the W metal electrode. This results in a Schottky contact. The oxygen vacancy concentration, the local temperature, the current density and the applied electric field have a profound effect on the Schottky barrier height, to the space charge region  $x_D$ , and consequently to the resistivity, which is summarized by the thermoionic-field emission, as it is already discussed in Sect. 2.3.

### 8.1.2 Summary

In this section we investigated the correct resistive switching parameters of a LSMO thin film in a vertical geometry. It turned out that a voltage set of same amplitude and opposite polarity (+5 V/-5 V) gives the optimal results in terms of reproducibility and a maximum ON/OFF ratio ( $\sim 600$ ). Moreover, the driving mechanisms behind the switching phenomenon in LSMO were discussed. Here, an electric field-directed migration of oxygen vacancies leads to a local redistribution of the oxygen concentration, which significantly affects the double exchange mechanism. Further, the oxygen vacancy concentration at the interface leads to a modulation of the Schottky barrier between the thin film and the electrode, which has a profound effect to the change in resistivity.

The above presented study demonstrates the feasibility of the resistive switching phenomenon in our LSMO thin films and serves as a preliminary experiment for the following one, in which we investigate the spectromicroscopical fingerprints of electrically modified areas switched into a high resistive state.

## 8.2 PEEM Study of the Magneto-Ionic Effect in $\text{La}_{0.7}\text{Sr}_{0.3}\text{MnO}_3$

The ultimate goal of this thesis is to image chemical and particularly magnetic changes induced by electrical modifications of LSMO thin films utilizing photoemission electron microscopy. The identification of the underlying microscale redox processes and their respective spectral fingerprints serves as a preparation for a prospective time-resolved monitoring of the resistive states during operation (i.e. "operando"). Since the voltage-driven change of the resistivity in LSMO thin films is assumed to depend on the oxygen vacancy concentration, occupation modifications are primarily expected for the  $\text{MnO}_6$  octahedron. Therefore, possible spectral fingerprints are expected to manifest in both line shape modifications of the Mn  $L_{3,2}$  and O  $K$ -edges and shifts of the work function and the Fermi level due to changing occupation of the conduction band. Also changes of the A site cations (i.e.  $\text{La}^{3+}$  and  $\text{Sr}^{2+}$ ) are possible and will be part of the discussion. But due to experimental limitations the A site cationic fingerprints were not entirely accessible, which allows only a superficial treatment of this topic.

The present section will begin with the electrical treatment of the LSMO thin film by locally conductive atomic force microscopy in vacuum as described in Sect. 8.2.1. Afterwards, it follows a detailed PEEM study of the respective electrically modified regions. In particular, chemical contrast images and spectra are recorded across the Mn  $L_{3,2}$ -, O  $K$ -, and the La  $M_{5,4}$ -edges in Sect. 8.2.2.

Subsequently, the magnetic properties will be investigated by spatially resolved XMCD. Here, it will be shown, that there is a distinct correlation between oxygen vacancies, resistivity, chemical structure, and magnetism. Finally, on the basis of literature and own reference spectra, possible brownmillerite structures in our resistively changed regions will be discussed, Sect. 8.2.4.

### 8.2.1 Electric Field Modification by LC-AFM

The electrical treatment of the LSMO sample was realized by utilizing LC-AFM in a commercial variable temperature scanning probe microscope (VT-SPM, Scienta Omicron) equipped with an ultrananocrystalline diamond (UNCD) cantilever (AppNano). The LC-AFM device was operated in the contact mode. The cantilever is coated with a boron-doped diamond layer and

exhibits a tip radius of  $R_{Tip} < 150$  nm. In order to remove any adsorbates, the sample was heated to 190°C for about 30 minutes in an oxygen environment of 0.1 mbar prior to the LC-AFM measurements. The base pressure during the switching experiment was set to  $3 \cdot 10^{-9}$  mbar.

**I-V switching in Vacuum** The same vertical switching geometry was applied as presented in the preliminary experiment performed in ambient atmosphere, i.e. the tip electrode was applied perpendicular to the LSMO thin film surface, while the Nb:STO substrate was set to ground. At a fixed tip position the voltage was ramped from +5 V to -5 V and vice versa.

Fig. 8.5 shows the resulting I-V curve. Due to a read out limitation of the LC-AFM device only an upper/lower limit on the current is available above/below 333 nA. However, a clear hysteretic behaviour and a SET/RESET range around -3V/+3V are observed. Further, there is a gradual RESET transition from LRS to HRS. Thus, the switching process seems to be comparable to the experiment performed in ambient atmosphere. However, the reproducibility of the resistive switching cycles was not comparable. The cell-to-cell variability (varying the tip electrode position) revealed an unreliable switching process. Approximately 70 % of the switching cycles showed a non-reversible behaviour and stayed at the high resistive state.

There are several possibilities, which might explain our observations. For instance, a tip electrode of several tens of nanometers might be sensitive to possible residual adsorbates at the thin film surface, which could be implanted during the application of a voltage. A local coating of insulating lanthanum- or strontium oxide could be a consequence, which reduces the conductivity of the tip electrode. A contrary indication is the fact that the sample can be switched reproducibly from the pristine state into the HRS. Moreover, the conductivity of the tip was verified on platinum electrodes between several I-V experiments. Thus, a significant change of the tip electrode can be excluded. A more plausible explanation might be found in the oxygen exchange process at the interface between the thin film surface and the vacuum. As extensively discussed in Sect. 8.1, a removal of the oxygen across the LSMO/vacuum interface driven by the gradient of the chemical potential leads to a transition from the pristine state or LRS into the HRS. On the other hand, the transition back to the LRS requires an incorporation of oxygen into the thin film. Regarding the fact, that the switching experiment was performed in vacuum, the question arises about the source of oxygen. From this point of view, it is surprising, that we observe switching cycles at all. Here, local spots of larger oxygen concentrations at the surface or adsorbed oxygen anions at the tip electrode could provide a sufficient supply to incorporate oxygen anions at least into the topmost layers within the filament, which could be enough for an interface switching type.

Furthermore, residual water or other hydrides could also be a part of the answer. Recent studies of magneto-ionic devices performed by A. J. Tan *et*

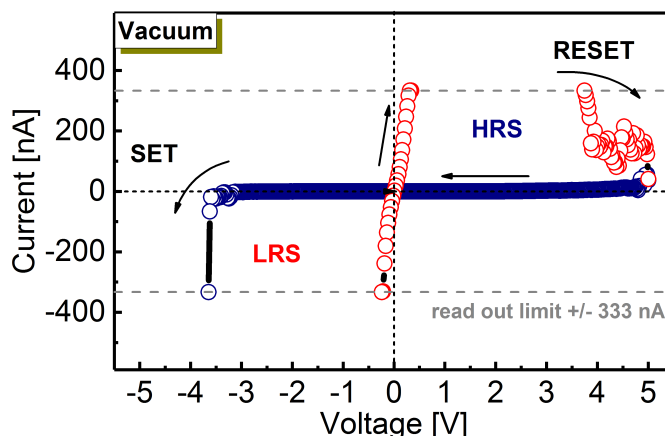


**Figure 8.5:** 30 % of the I-V cycles reveal the illustrated switching characteristics. By means of a LC-AFM the switching experiment was performed in vacuum. Due to a read out limitation of the device only an upper/lower limit on the current is available above/below 333 nA. However, a clear hysteretic behaviour and a SET/RESET range around -3V/+3V are observed.

*al.* have shown that the process of voltage-directed oxygen migration can tremendously depend on the atmosphere surrounding of the experimental device [146]. In vacuum or dry nitrogen, devices revealed no or only very slow function, whereas, in ambient atmosphere or "wet" nitrogen (bubbling nitrogen through water) the devices show high-speed performances. Worth mentioning is that the devices operate only at voltages greater than 1.5 V, which matches the standard decomposition potential of water. Thus, an electrolysis at the surface is assumed, where the hydrogen i.a. bind with the oxide to form hydroxides or interstitial water. This could be an explanation for the good switching performance of the LSMO thin film in ambient atmosphere. Finally, in the scope of the present thesis, the question about the switching mechanism of our thin film system in vacuum remains open.

Nevertheless, in order to follow our goal to investigate the chemical and magnetic properties of the respective resistive states, all required ingredients are given. The sample can be switched into the HRS reproducibly. Even though we do not switch back to the LRS, the pristine LSMO represents an oxygen saturated state. Thus, a significant variation of the chemical and magnetic fingerprint between the LRS and the pristine state is not expected. However, typically, "resistive switching" describes a reversible process, which is not the case here. Therefore, the following experiment describes an electrical modification of the LSMO thin film rather than resistive switching.

**Electric Field Modification** The electrical modification of the LSMO sample was realized by scanning over  $2 \times 2 \mu\text{m}^2$  sized areas with constantly applied voltages, while the substrate was set to ground (Fig. 8.6). The tip scan started at one corner of the area and the tip was moved back and forth using a total

of 500 lines to cover the entire area. The scan speed was set to  $5 \mu\text{m}/\text{s}$ . We wrote areas with different polarities between  $-3$  and  $+5$  V. Hereinafter, we label these areas by referring to the respective voltages applied. In order to prevent unintentional modifications of the resistive states after the writing process, no read out measurements were performed afterwards.

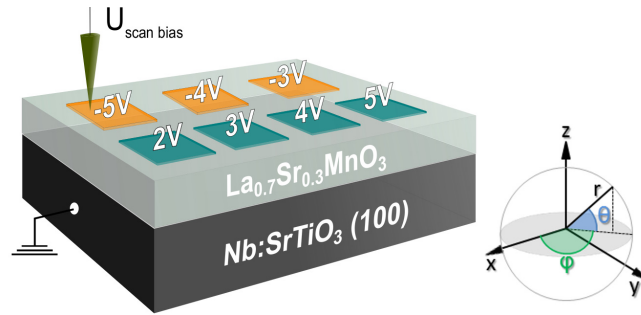


**Figure 8.6:** Setup of the experiment in UHV: Composition stack consisting of a conducting  $5 \times 5 \text{ mm}^2$  Nb:STO(001) substrate, and a 10 nm thick  $\text{La}_{0.7}\text{Sr}_{0.3}\text{MnO}_3$  thin film.  $2 \times 2 \mu\text{m}^2$  sized squares are written by a scanning LC-AFM tip electrode under applied constant voltages.

## 8.2.2 Chemical Fingerprint of Electrically Modified $\text{La}_{0.7}\text{Sr}_{0.3}\text{MnO}_{3-\delta}$

To study the microscale redox processes present in the electrically modified areas of the LSMO thin film, we performed X-ray photoemission electron microscopy. PEEM provides the capability of measuring all voltage-treated areas at the same time. This allows us to directly compare magnetic and chemical properties with the electrical pre-treatment and set them into relation, since one does not have to deal with homogeneity issues and sample preparation reproducibility. The respective images and spectra were recorded for the Mn  $L_{3,2-}$ , O  $K-$ , and La  $M_{5,4}$ -edges. Subsequently, we performed principle component analysis (PCA) [147, 148] on the PEEM data<sup>1</sup>. In PCA, the original data set is described in a new orthogonal coordinate system, which is spanned along new principal component (PC) axes. The PCs are oriented along the largest, uncorrelated variances in the data. The spectral information is covered by the largest data variances whereas smaller variances are generally related to noise. Hence, only a small number of PCs is sufficient to describe the relevant spectral features and one can reconstruct the original data using merely the small set of relevant PCs, thereby improving the signal-to-noise ratio substantially. As has been demonstrated in [149, 150], PCA can reveal small signals mostly camouflaged by noise. A further advantage of PCA is that the

<sup>1</sup> The PCA code was provided by Margret Giesen, Forschungszentrum Jülich GmbH, Peter-Grünberg-Institut 6, 52428 Jülich, Germany.

data variances can be related to certain pixels in the original PEEM image, thereby providing high spatial chemical resolution. A detailed description of the principal components and the respective PEEM data reconstructions for various photon energies of the absorption edges can be found in App. C.

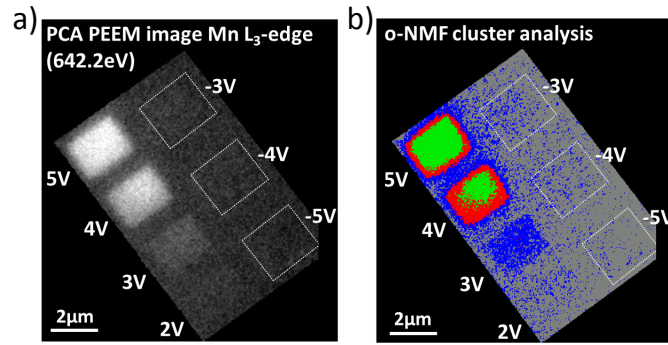
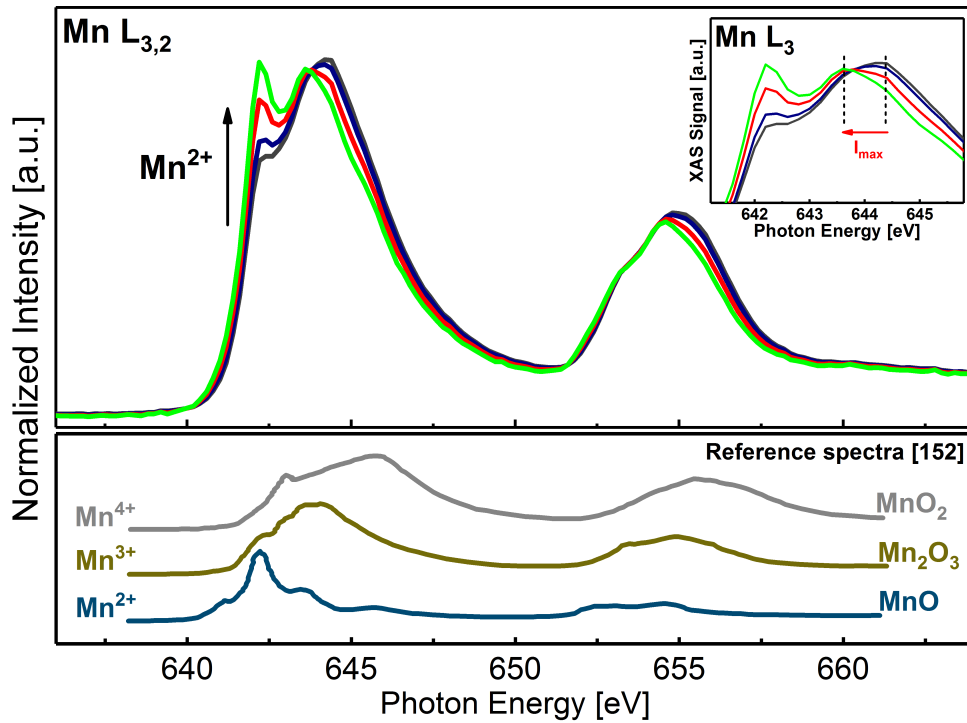


**Figure 8.7:** Real space imaging of the Mn  $L_3$ -edge. (a) Reconstruction of the original PEEM image by the main principle components. The chemical contrast of the modified regions at the Mn  $L_3$ -edge ( $h\nu = 642.2$  eV) reveals a significantly enhanced intensity for 4 V and 5 V (HRS). (b) False-colour representation of the PCA PEEM image in (a) indicating pixels of high spectral similarity as obtained by orthogonal non-negative matrix factorization (o-NMF). The mean spectra determined from the average over all spectra within the coloured areas (grey, blue, red, green) are plotted in Fig. 8.8, 8.10 (top) using the same colour code.

Fig. 8.7 (a) shows the PCA reconstruction of the original PEEM image for the Mn  $L$ -edge ( $h\nu = 642.2$  eV). The contrast of the areas modified with positive voltages raises with increasing amplitude and shows a significant chemical transition between 3 V and 4 V. From the previous resistive switching experiment shown in Fig. 8.5, we conclude that there is also a metal-to-insulator transition between 3 V and 4 V. Thus, there is an obvious correlation between the enhanced chemical contrast and the transition from pristine low resistivity to high resistivity. The areas written with a negative voltage reveal only weak contrast levels without any obvious trend.

For the cluster image and the corresponding spectra shown in Fig. 8.7 (b) and Fig. 8.8-8.15, we made use of a cluster analysis, which is based on ortho-non-negative matrix factorization (o-NMF) and group classification of similar Euclidian distances as described in [151]. In the work presented here, o-NMF identifies pixel groups where PEEM spectra are similar: chemical inhomogeneities cause spectral changes which lead to mean-square deviations between spectra. The o-NMF identifies those deviations and sorts spectra into different groups, which are visualized in Fig. 8.7 (b) as differently coloured pixels.

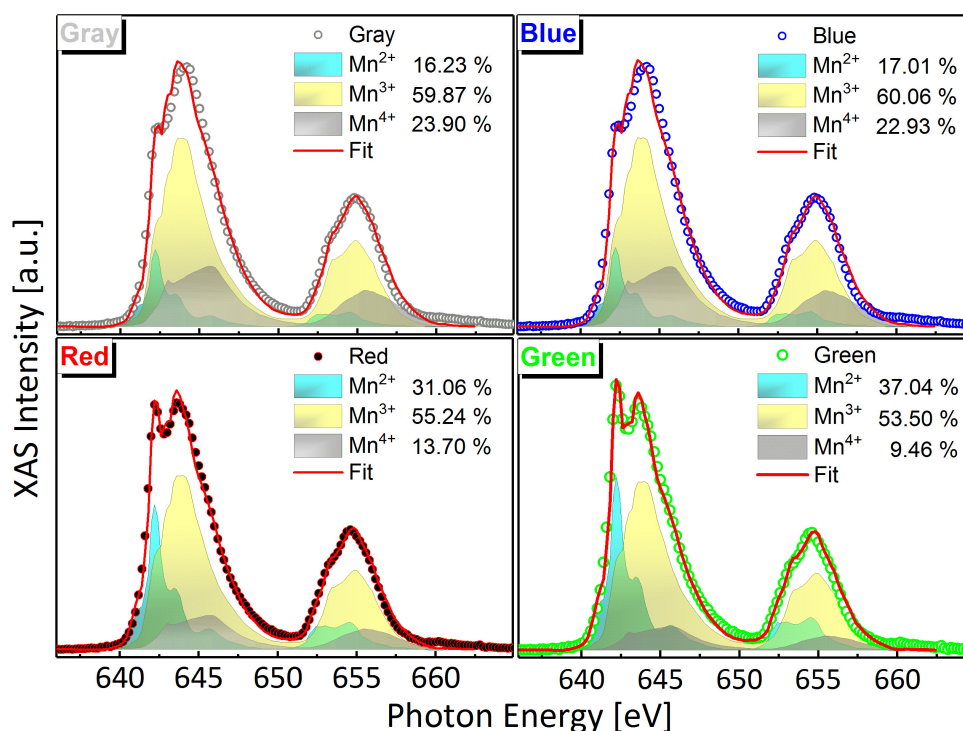
In the case of voltage-treated LSMO, four clusters with sufficient spectral resolution and the most physical sense (grey, blue, red and green) are identified for the Mn  $L_{3,2}$  and O  $K$ , and La  $M_{5,4}$ -edges. The grey cluster corresponds



**Figure 8.8:** (top) X-Ray absorption spectra of the Mn  $L_{3,2}$ -edge averaged over the cluster regions as shown in Fig. 8.7 (b) using the same colour code. The areas modified with a positive tip polarization show an increasing  $\text{Mn}^{2+}$  contribution with increasing voltage. (bottom) Reference spectra indicating  $\text{Mn}^{2+}$ ,  $\text{Mn}^{3+}$ , and  $\text{Mn}^{4+}$ . Adapted from [152].

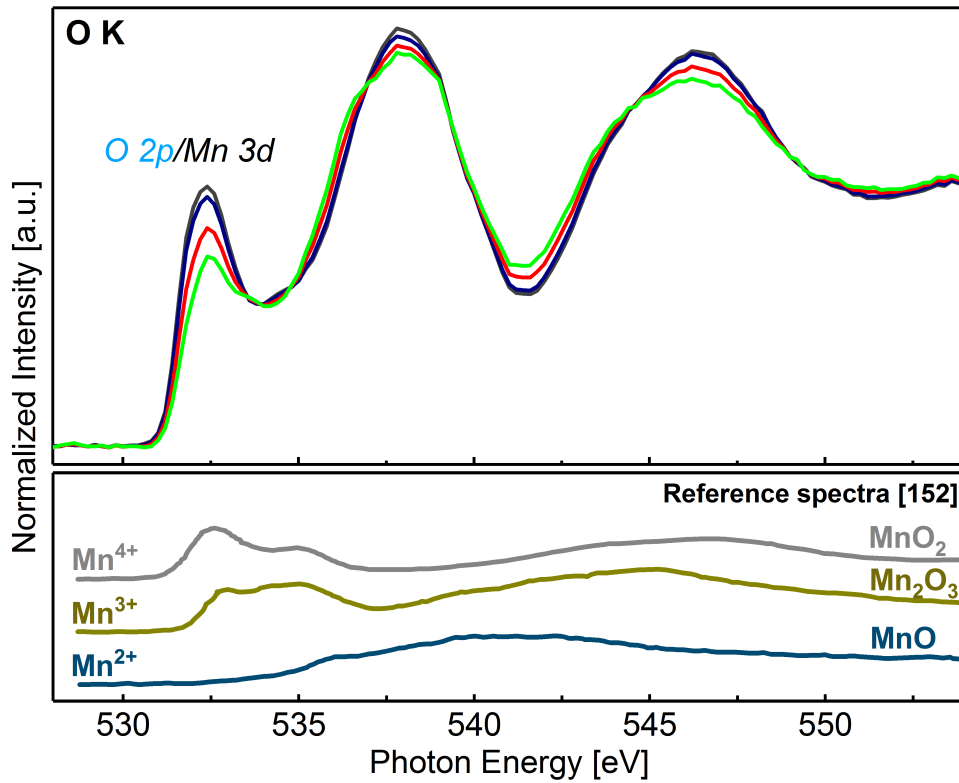
to untreated sample regions and represents the pristine state. Isolated, scattered blue pixels seem to be located mainly within areas treated with voltages. Between -5 V and -3 V, increasing the voltage leads to a slight increase in the contribution of the blue cluster. However, this increase is hardly above the noise level. The chemical contrast significantly changes between 2 V and 5 V. The area treated with 3 V shows a homogeneously distributed contribution of the blue cluster. The 4 V area consists of three clusters, which form a concentric alignment of rectangles. From the outermost region to the center the clusters are encoded in blue, red, and green, respectively. In case of 5 V we observe a similar concentric arrangement of clusters, but with a significantly larger contribution of green in the center.

Fig. 8.8 shows a direct comparison of the according spectra recorded at the Mn  $L_{3,2}$ -edge, where each colour is assigned to the respective cluster as defined in the o-NMF analysis (Fig. 8.7 (b)). We observe an emerging low energy peak at  $h\nu = 642.2$  eV from the grey to the green spectrum. A significant increase of the peak is obtained between the blue and the red spectrum, noticing, that this accompanies the metal-to-insulator transition. The low energy feature, which is separated by 1 eV from the main peak can be ascribed to the appearance of  $\text{Mn}^{2+}$  cations [153, 154]. We also note that the main peak of the red and green spectrum, located at  $h\nu = 644$  eV, reveals an apparent shift of



**Figure 8.9:** Decomposition of the measured spectra by linear superposition of the reference spectra from [152]. The curve fitting procedure was performed by applying the Levenberg-Marquardt-algorithm.

the maximum intensity  $I_{max}$  towards lower photon energy (Fig. 8.8 (inset)). The Mn  $L$ -edges of  $\text{MnO}$ ,  $\text{Mn}_2\text{O}_3$  and  $\text{MnO}_2$  reference samples are shown in Fig. 8.8. They indicate the three valence states of  $\text{Mn}^{2+}$ ,  $\text{Mn}^{3+}$  and  $\text{Mn}^{4+}$  [152] and illustrate the possible components, which might form the Mn  $L_{3,2}$ -edge spectra of a LSMO thin film after voltage-treatment. In particular, the  $\text{MnO}$  reference spectrum illustrates the origin of the low energy peak of the measured spectra at  $h\nu = 642.2$  eV, which is assigned to  $\text{Mn}^{2+}$ . In order to work out the trend of the manganese cation concentration, we used these reference spectra to decompose our measured data by a linear superposition with three coefficients  $a$ ,  $b$  and  $c$  indicating the  $\text{Mn}^{2+}$ ,  $\text{Mn}^{3+}$  and  $\text{Mn}^{4+}$  contributions. The optimization of the coefficients was realized by the numerical Levenberg-Marquardt-algorithm [155]. The relative binding energy positions of the respective manganese cations were adapted from the reference and fixed as an initial input parameter, while the output is the XAS intensity. The results of the iterative curve fitting are shown in Fig. 8.9. Here, the dotted lines denote the measured data, while the coloured filled spectra indicate the relative contributions of  $\text{Mn}^{2+}$ ,  $\text{Mn}^{3+}$  and  $\text{Mn}^{4+}$ . The respective fitting curve is illustrated by the red line. Although the curve fitting does not completely reproduce the experimental data, the line shape is already satisfying, considering that the reference spectra do not reflect the cationic behaviour within a perovskite structural environment.



**Figure 8.10:** (top) X-ray absorption spectra of the O K-edge averaged over the cluster regions as shown in Fig. 8.7 (b) using the same colour code. The areas modified with a positive voltage exhibit a decreased O 2p-Mn 3d hybridization peak with increasing voltage. (bottom) Reference spectra indicating  $\text{Mn}^{2+}$ ,  $\text{Mn}^{3+}$ , and  $\text{Mn}^{4+}$ . Adapted from [152].

It turns out that the pristine state (grey) already appears in a partially reduced state ( $\delta > 0$ ). A somewhat larger  $\text{Mn}^{2+}$  concentration is calculated for the blue cluster, which is already indicated by the increased low energy feature. It has been shown that  $\text{La}_{0.7}\text{Sr}_{0.3}\text{MnO}_{3-\delta}$  thin films initially tend to show a  $\text{Mn}^{2+}$  contribution at the surface [153]. But the question about the origin of the  $\text{Mn}^{2+}$  cations is not answered yet. A possible reason for the presence of  $\text{Mn}^{2+}$  could be a valence instability of the  $\text{Mn}^{3+}$  cations close to the surface. However, we conclude that the application of a negative tip bias does not significantly affect the oxidation state.

A considerable increase of the  $\text{Mn}^{2+}$  contribution is observed for the red and green spectrum, which validates the concept of a significant valence change from a  $\text{Mn}^{3+/4+}$  to a  $\text{Mn}^{2+/3+}$  dominated state, which is a consequence of the removal of oxygen anions due to the positive applied voltage. The deficiency of oxygen provides the system with additional electrons, which are received by the Mn cations leading to a larger  $\text{Mn}^{2+}$  concentration in order to compensate the charge disparity.

A variation of the oxygen vacancy concentration should also impact the O  $K$ -edge spectra (Fig. 8.10), in particular on the peak located at  $h\nu = 532.3$  eV, which is assigned to the hybridization state between the O  $2p$  and the Mn  $3d$  states [156, 157]. As becomes obvious from the reference spectra in Fig. 8.10 (bottom), a decrease in oxidation state of the Mn leads to a decrease of the O  $2p$ -Mn  $3d$  hybridization peak.

The grey spectrum shows the largest intensity as it represents the pristine LSMO thin film with the largest oxygen stoichiometry. The peak intensity decreases from blue to green, indicating less unoccupied electronic states of the manganese and corroborating the increasing oxygen vacancy concentration for increasing positive voltages. In line with the metal-to-insulator transition and the results from the Mn  $L$ -edge, we observe a considerable modification of the spectral intensities between the blue and the red spectrum.

It turned out that a fitting procedure of the O  $K$ -edge with the respective reference spectra only gives very poor results. There are multiple reasons for why the spectra cannot be reproduced. First, the length of the post-edge region is not long enough for both the measured and the reference spectra. Thus, the post-edge cannot be determined properly, which is essential for a reasonable background subtraction in order to perform a comparison of two independent data sets. Moreover, adsorbates like hydroxides and carbonates at the thin film surface can have profound effects to spectral features measured with surface sensitive techniques. Also residual oxygen attached to optical elements within the beam path of the synchrotron beamline plays a role and becomes crucial by comparing data sets measured at different beamlines.

After the spectral interpretation of the clusters, one can discuss the concentric alignment of the clusters, shown in Fig. 8.7 (b). The pattern is likely caused by the gradient of the applied electric field and the scanning pattern along which the field was applied. Thus, due to the radial decay of the electric field, there are only weak changes along the edges of the written rectangle area. However, a local point in the center of the modified area experiences the electric field of the tip electrode several times due to the writing pattern. Consequently, more oxygen anions will be released, which enhances the chemical contrast in the center with respect to the edges and forms the observed concentric contrast variation.

Besides the change of the oxygen octahedra and the B site cations also the A site cations might be affected by the occurrence of oxygen vacancies. It has been reported that oxygen vacancies in LSMO thin films can cause a segregation of Sr or La towards the thin film surface, which results in a formation of lanthanum- or strontium oxide [158]. An excess of one of the two A site cations at the surface would lead to an increase of the respective spectral intensities. The spectra of the measured La  $M_{5,4}$ -edge are shown in Fig. 8.11. The spectra do not show any remarkable differences in the line shape or spectral

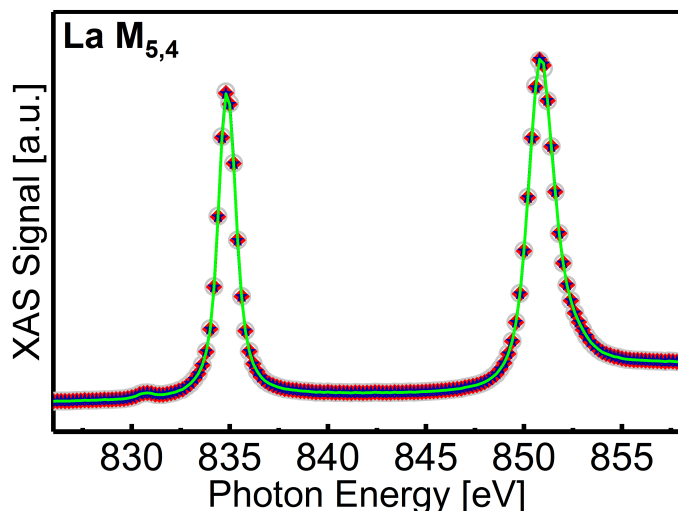


**Figure 8.11:** X-ray absorption spectra of the La  $M_{5,4}$ -edge averaged over the cluster regions as shown in Fig. 8.7 (b) using the same colour code. In contrast to manganese and oxygen, lanthanum shows a homogeneously distributed contribution over the whole field of view.

intensity. Since no significant contrast is obtained, we conclude that the La contribution is homogeneously distributed over the sample and the La signal is not affected within the electrically modified areas.

Since our synchrotron beamline only provides photon energies in the soft X-ray regime (55 - 1500 eV), we had no experimental access to any Sr absorption edges (Sr  $K$ -edge  $\sim 1600$  eV, Sr  $L_{3,2}$ -edge  $\sim 2000$  eV). From this, the question about A site stoichiometric changes in our LSMO thin film system cannot be fully answered here.

Our observations of significant changes of the manganese valence state, the incorporation of oxygen vacancies, and the metal-to-insulator transition already strongly suggest that the magnetic properties may very likely be affected as well as being due to a diminished DE coupling.

### 8.2.3 Magnetic Fingerprint

In order to gain a deeper understanding of the electrically induced change of the magnetic properties and altered exchange interactions, spin-sensitive and element-selective XMCD-PEEM measurements of the Mn L-edge will scrutinize the interplay between valence change, resistivity, and magnetic ordering.

Similar to the o-NMF cluster analysis as performed for the  $0^\circ$  XAS measurement (Fig. 8.7 (b)) we performed an o-NMF cluster analysis for the XMCD measurement (Fig. 8.15). Obviously, there is a similar distribution of clusters (grey, blue, red, green) as before.

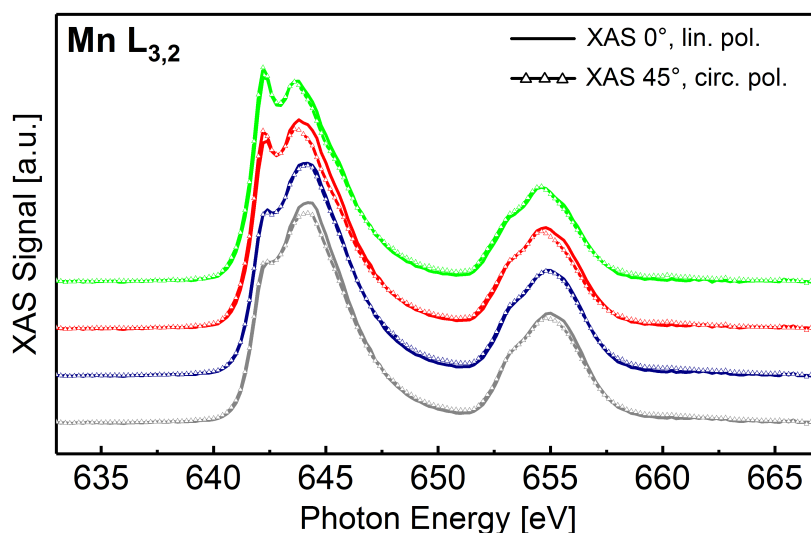


**Figure 8.12:** Comparison of XAS spectra recorded at an azimuthal angle of  $\varphi = 0^\circ$  (solid line) and  $\varphi = 45^\circ$  (line with symbols). At  $0^\circ$  the spectra were generated by means of linear horizontally polarized light. The XAS data recorded at a sample rotation of  $45^\circ$  are obtained by averaging left- and right circularly polarized XAS signals.

The following XMCD data were recorded under an azimuthal angle of  $\varphi = 45^\circ$  with respect to the XAS data shown above. The monitoring with circularly polarized light at a relative azimuthal angle of  $\varphi = 0^\circ$  revealed a non-perfect focus of the microscope, which in our case leads to unreasonable results, due to a low signal-to-noise ratio.

In order to check for the comparability of the two data sets (XAS at  $\varphi = 0^\circ$  and XMCD at  $\varphi = 45^\circ$ ), the left- and right circularly polarized XAS spectra were averaged, and subsequently a two-step function background was subtracted from all spectra. Fig. 8.12 shows the direct comparison of both data sets. Deviations are observed exclusively for the red and grey spectra. The small

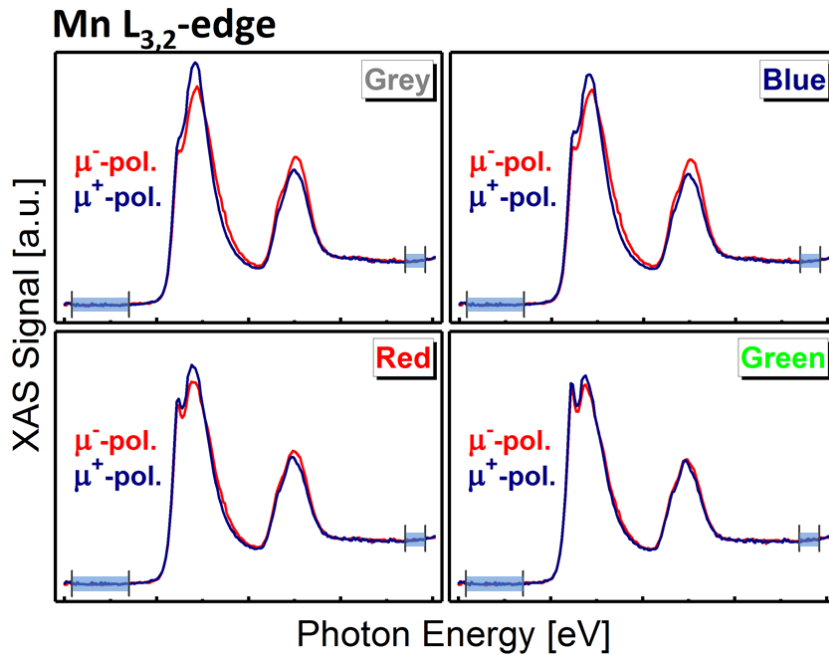


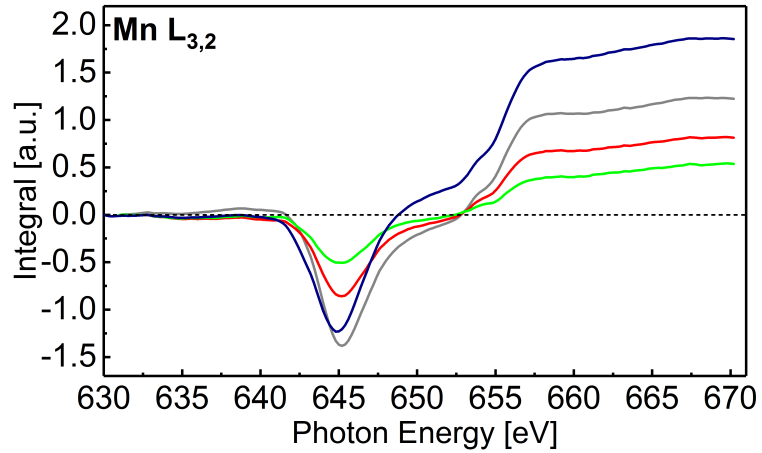
**Figure 8.13:** Left ( $\mu^-$ )- and right ( $\mu^+$ ) circularly polarized X-ray absorption spectra after background subtraction and normalization. The blue regions indicate the pre- and post edge regions chosen for the linear background subtraction and the normalization, respectively. The labelling (grey, blue, red and green) corresponds to the colour-coded regions defined by the PCA.

deviations can be explained by the approximative nature of the two-step function background subtraction (where the step position can vary). Since we do not observe an angle dependent XLD effect of the LSMO samples, the linearly polarized  $0^\circ$  XAS data can be directly compared to the circularly polarized  $45^\circ$  XMCD data.

Before a detailed discussion of the XMCD analysis, it is worth mentioning that there was no external magnetic field applied during the spectromicroscopical measurements, due to probable perturbations of the emitted photoelectrons' trajectory path. Thus, the observations made in this experiment are based on a remanent ferromagnetic response. The sample has been magnetized with an external magnetic field of 1.5 T prior to the electrical treatment utilizing the VSM. We did not observe any magnetic inhomogeneities. Hence, the pristine LSMO sample is in a single domain state. Therefore, we conclude that the magnetic contrast change as observed in our experiments is related to the electrical treatment.

A well-chosen pre-edge range was applied to all spectra and was used for calculating the linear background. Fig. 8.13 shows the left ( $\mu^-$ )- and right ( $\mu^+$ ) circularly polarized X-ray absorption spectra after background subtraction and normalization. The blue regions indicate the pre- and post-edge ( $h\nu_{post}$

**Figure 8.14:** Integrals over the XMCD curves in Fig. 8.15. All integration curves converge towards a finite value.



(= 668-672 eV) regions chosen for the linear background subtraction and the normalization, respectively. While the left ( $\mu^-$ ) circularly polarized curves (red line) exhibit lower intensities with respect to the right ( $\mu^+$ ) circularly polarized curves (blue line) at the  $L_3$ -edge, they reveal larger intensities at the  $L_2$ -edge. This is assigned to the opposite spin polarization at the two edges due to the opposite sign of the spin-orbit coupling of the  $2p_{3/2}$  ( $L_3$ ) and  $2p_{1/2}$  ( $L_2$ ) levels.

A further criterion, which indicates a correct processing of the XMCD analysis, can be found by the integration of the XMCD curves, which is shown in Fig. 8.14. The post-edge regions of all integrals do converge towards a finite value. The results in Fig. 8.13 and Fig. 8.14 already suggest a ferromagnetic behaviour for all clusters. Finally, the difference spectra or the XMCD signals of the respective circularly polarized data are calculated by Eq. 4.13. The XMCD signals of each cluster exhibit the characteristic ferromagnetic signature of perovskite LSMO thin films at room temperature [159, 160], which originates from the double-exchange interaction between  $\text{Mn}^{3+}$  and  $\text{Mn}^{4+}$ . The grey XMCD spectrum reveals the largest XMCD signal and represents the pristine ferromagnetic state. The strength of the XMCD signal decreases with increasing positive voltage.

From this, we deduce a clear dependence of the ferromagnetic properties on the oxygen vacancy concentration and the corresponding Mn valence state. The ferromagnetic properties degrade with increasing oxygen vacancy concentration and concurrently with an increasing  $\text{Mn}^{2+}$  contribution. A straightforward explanation for this phenomenon is a disturbed double-exchange interaction. The delocalization of the  $e_g$  electron between the  $\text{Mn}^{3+}$  and  $\text{Mn}^{4+}$  cations is crucial in order to stabilize a parallel and ferromagnetic alignment of the respective  $t_{2g}$  electron spin states. Since the delocalization of the  $e_g$  electron is mediated by an interlinking oxygen anion between  $\text{Mn}^{3+}$  and  $\text{Mn}^{4+}$ , the exchange process is perturbed due to a missing oxygen anion.

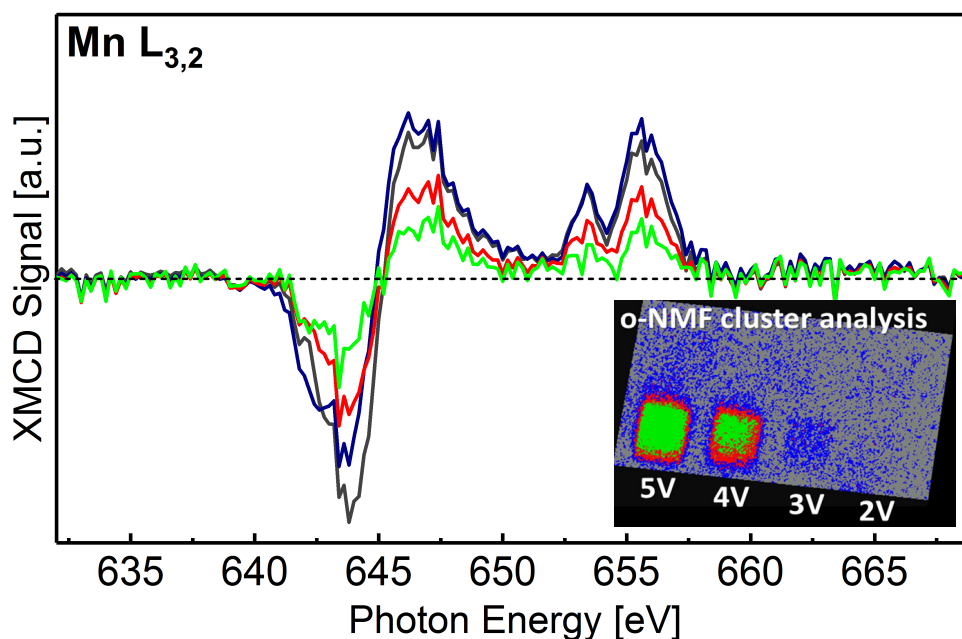


**Figure 8.15:** XMCD spectra of the Mn  $L_{3,2}$ -edge extracted and averaged over the color coded cluster regions defined by the o-NMF analysis (inset). The XMCD signal decreases with increasing positive voltage and reveals a significant ferromagnetic contrast between 3 and 4 V.

Besides a perturbation of the double-exchange mechanism there is also another scenario, which might drive the remarkable valence change, the degrading resistivity and the loss of ferromagnetic ordering. Recent studies have reported about a phase transition from a perovskite ( $\text{ABO}_3$ ) to a brownmillerite ( $\text{ABO}_{2.5}$ ) phase, which identify similar effects as described above. This has persuaded us to perform microspectroscopical investigations also on brownmillerite  $\text{La}_{0.7}\text{Sr}_{0.3}\text{MnO}_{2.5}$  thin films. A review of the literature and, subsequently, experimental results will be discussed in the following.

### 8.2.4 Brownmillerite Phase: Structural Phase Transition in $\text{La}_{0.7}\text{Sr}_{0.3}\text{MnO}_{3-\delta}$

**Review of Literature** The migration and redistribution of oxygen vacancies do have profound effects to chemical, electronic, and magnetic properties in complex manganites and particularly in LSMO. However, there have been several reports, which observe also a structural phase transition from a perovskite (PV) to a brownmillerite (BM) structure driven by thermal and/ or electrical treatment. Oxygen vacancies in  $\text{La}_{0.7}\text{Sr}_{0.3}\text{MnO}_{3-\delta}$  have been shown to accumulate near to interfaces and form a BM structure. The  $\text{ABO}_{2.5}$  BM phase reveals an alternating sequence of  $\text{BO}_6$  octahedral layers and  $\text{BO}_4$  tetrahedral layers along the stacking direction. The size of the BM LSMO unit cell is twice as large as the PV unit cell. The evolution from PV,  $\text{ABO}_3$ , to BM,  $\text{ABO}_{2.5}$  for  $\text{La}_{0.7}\text{Sr}_{0.3}\text{MnO}_{3-\delta}$  is illustrated in Fig. 8.16. Theoretical calculations

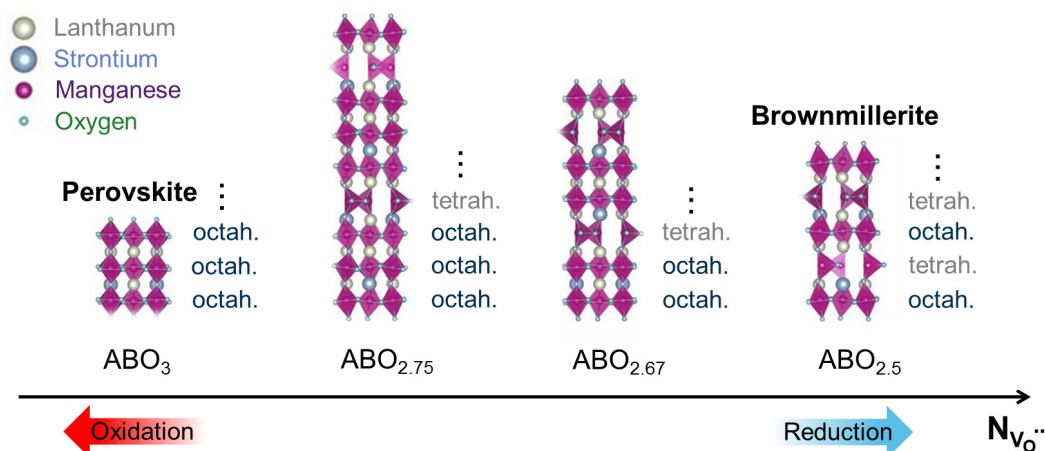


**Figure 8.16:** Evolution from a PV,  $\text{ABO}_3$ , to a BM,  $\text{ABO}_{2.5}$  structure for a  $\text{La}_{0.7}\text{Sr}_{0.3}\text{MnO}_{3-\delta}$  thin film on STO (001). Modified from [161].

performed by M. Moreau *et al.* have shown that the oxygen stoichiometry can be controlled in a "block-by-block" approach, where the number of octahedral layers decreases with reduction of the oxygen concentration [161]. Starting from  $\text{ABO}_3$  considering a pure octahedral based thin film, via  $\text{ABO}_{2.75}$ ,  $\text{ABO}_{2.67}$  and finally approaching  $\text{ABO}_{2.5}$ , the structure reveals a ratio between the octahedral and tetrahedral layer of 3:1, 2:1, and 1:1, respectively. The  $\text{Mn}^{2+}$  oxidation state is predicted to be located in all tetrahedral sites, while half of the octahedral sites exhibit a  $\text{Mn}^{2+}$  state and the other half a  $\text{Mn}^{3+}$  state. Further, DFT calculations on the basis of intra-layer and magnetic nearest-neighbour approximations reveal several possible magnetic configurations for an LSMO thin film in the BM phase on top of a STO (001) substrate [161]. Significantly lower ground state energies are found for different magnetic sublattices in the tetrahedral and octahedral layers instead of a homogeneously distributed spin ordering in the entire BM thin film ( $\sim 10$  meV/f.u.). The energy difference between those low energy ground states is lower than 1 meV/f.u. In case of a relaxed crystal structure, which is expected for a bulk-like film, both the octahedrally coordinated  $\text{Mn}^{2+}$  and  $\text{Mn}^{3+}$  cations and the tetrahedrally coordinated  $\text{Mn}^{2+}$  cations are antiferromagnetically coupled, which results in a total magnetic moment of zero. However, the calculation for an in-plane tensile strained thin film tends to show a ferromagnetic superexchange coupling between the two octahedrally coordinated  $\text{Mn}^{2+}$  and  $\text{Mn}^{3+}$  cations and an antiferromagnetic coupling between the tetrahedrally coordinated  $\text{Mn}^{2+}$  cations, which finally results in a ferromagnetic net magnetization.

The electronic band structure and layer resolved electronic density of states (DOS) for the spin configuration with the lowest energy for a strained BM structure are shown in Fig. 8.17. Considering the tetrahedral layers, one observes a band gap of  $\sim 1.5$  eV, while the octahedral layers reveal an indirect

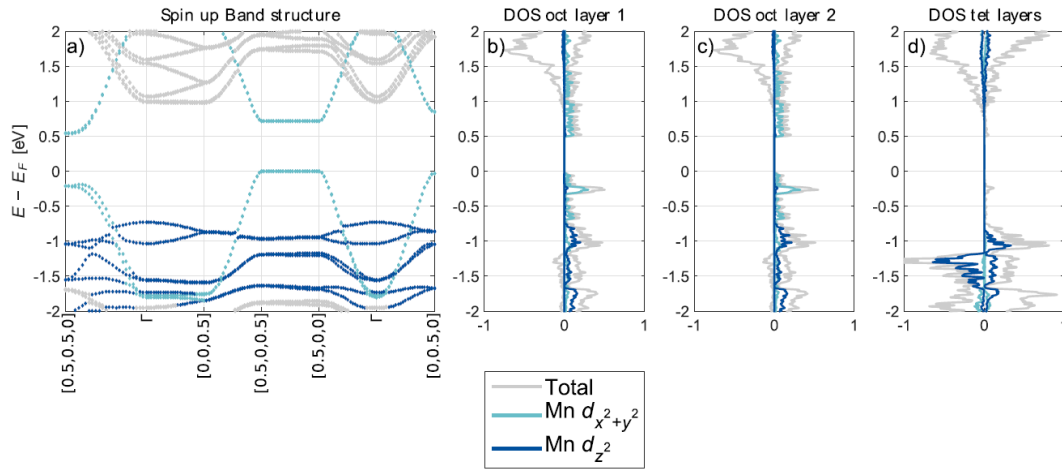


**Figure 8.17:** Electronic band structure and layer resolved density of states for the LSMO BM structure with ferromagnetic coupling in the octahedral layers and antiferromagnetic ordering in the tetrahedral layers. The bands where the projection on the Mn:  $d_{x^2-y^2}$  and Mn:  $d_{z^2}$  orbitals on each k-point exceeds 33 % are coloured according to the legend. Taken from [161].

band gap of  $\sim 0.5$  eV [161]. Moreover, the low band dispersion perpendicular to the layers compared to the in-plane band direction indicates a large effective mass and low electronic mobility in the out-of-plane direction, leading to a strong anisotropic conductivity [162, 163].

Experimentally, the insulating behaviour of the BM phase along the layer stack has been confirmed by L. Yao *et al.*. They have performed an *in operando* resistive switching experiment in a vertical geometry, which was monitored by a transmission electron microscope [24]. A striking correlation between the metal-to-insulator- and a structural phase transition from PV to BM was demonstrated. Both phase transitions have been assigned to a redistribution of oxygen vacancies close to the film/electrode interface.

L. Cao *et al.* performed an annealing study in vacuum and obtained a structural phase transition from PV  $\text{La}_{0.7}\text{Sr}_{0.3}\text{MnO}_3$  to a BM phase and revealed a concomitant magnetic phase transition from a ferromagnetic to an antiferromagnetic ordering with a Néel temperature of  $T_N = 30$  K [25]. Since the respective sample was a 45 nm thick film, this outcome corroborates the theoretical predictions of an antiferromagnetic spin ordering in a relaxed BM structure.

Finally, a spectral fingerprint was identified for the BM  $\text{La}_{0.5}\text{Ca}_{0.5}\text{MnO}_{2.5}$  system [164]. In particular, the Mn  $L_{3,2}$ - and O  $K$ -edge show characteristic spectral features, which are comparable to the results shown in the present thesis. Fig. 8.18 (a) and (b) show the Mn  $L_{3,2}$ - and O  $K$ -edge of their respective reference spectra indicating the  $\text{Mn}^{2+}$ ,  $\text{Mn}^{3+}$ , and  $\text{Mn}^{4+}$  fingerprints, and the PV and BM phase of LCMO. The BM phase reveals an emerged low energy feature at the Mn  $L_{3,2}$ -edge, which they assign to  $\text{Mn}^{2+}$ , and the O  $K$ -edge

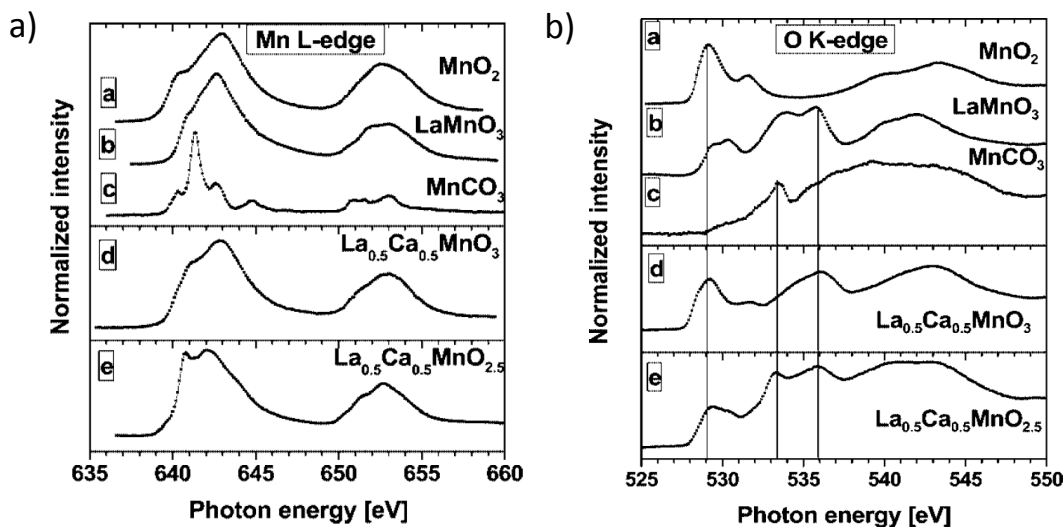


**Figure 8.18:** (a) Mn  $L_{3,2}$ - and (b) O  $K$ -edge XANES spectra of manganese reference compounds and samples. Taken from [164].

shows a decreasing O  $2p$ -Mn  $3d$  hybridization peak due to less unoccupied density of states at the Fermi level. Obviously, there is a significant valence change from a  $\text{Mn}^{3+/4+}$  state into a  $\text{Mn}^{2+/3+}$  dominated state.

The reported chemical and physical properties of BM manganites show similarities to our observations within the electrically modified areas treated with a positive voltage. Thus, we started to search for possible BM contributions in our voltage treated regions.

**Spectroscopical Investigation of a Brownmillerite Structure** To check for a possible BM phase in the electrically modified regions, the spectral fingerprint of a BM reference sample is first determined. A  $\text{La}_{0.7}\text{Sr}_{0.3}\text{MnO}_{2.5}$  BM sample was fabricated and provided by L. Cao from the Jülich Centre for Neutron Science (JCNS-2) and Peter-Grünberg-Institute (PGI-4), JARA-FIT, Forschungszentrum Jülich GmbH. The characterization of the sample has been performed as it can be taken from their publication [25]. The brownmillerite phase has been proven by XRD. Further, the 45 nm thick sample reveals low conductivity and an antiferromagnetic ordering below a Néel temperature of  $T_N = 30$  K. The BM structure of the investigated reference sample was evidenced also after the synchrotron experiment by a quick XRD-scan, as depicted in Fig. 8.19. Thus, we can be confident about having recorded the spectral signature of a BM phase. A comparison of the Mn  $L_{3,2}$ - and O  $K$ -edges of the respective PV and BM phase is shown in Fig. 8.20 (a) and (b). The black and green curve denote the pristine PV and the high resistive state already discussed in Sect. 8.2.2, while the dashed cyan coloured curve indicates the BM reference sample. A comparison of the spectral shape of the Mn  $L_{3,2}$ -edge

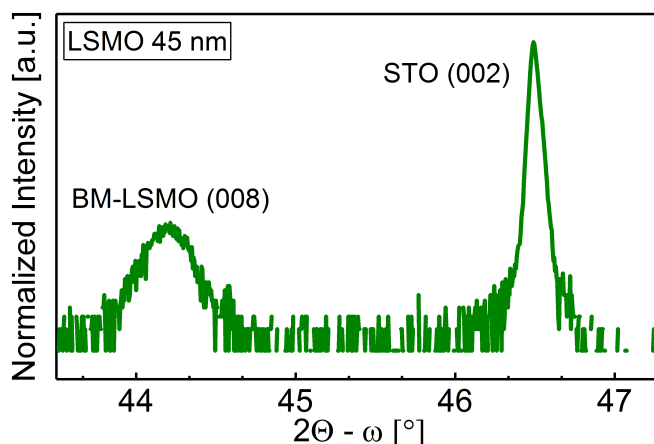


**Figure 8.19:**  $2\Theta - \omega$  scan reveals both the STO (002) Bragg peak and the BM (008) reflection of the LSMO thin film.

between the HRS and the BM phase shows that both spectral curves are almost identical, with its characteristic  $\text{Mn}^{2+}$  feature (Fig. 8.20 (a)). However, we observe a small difference in the high energy shoulder at  $h\nu = 645.6$  eV and at  $h\nu = 655.8$  eV, which is more pronounced in the HRS. The XAS data at the O  $K$ -edge show significant spectral deviations between the BM reference sample and the area switched into the HRS (Fig. 8.20 (b)). Even though the green (HRS) spectrum exhibits an emerging shoulder at  $h\nu = 533.6$  eV, which equals to the photon energy position of the maximum peak intensity of the BM reference sample, the respective intensity is not significant.

Even though the manganese absorption spectra are not perfectly identical,

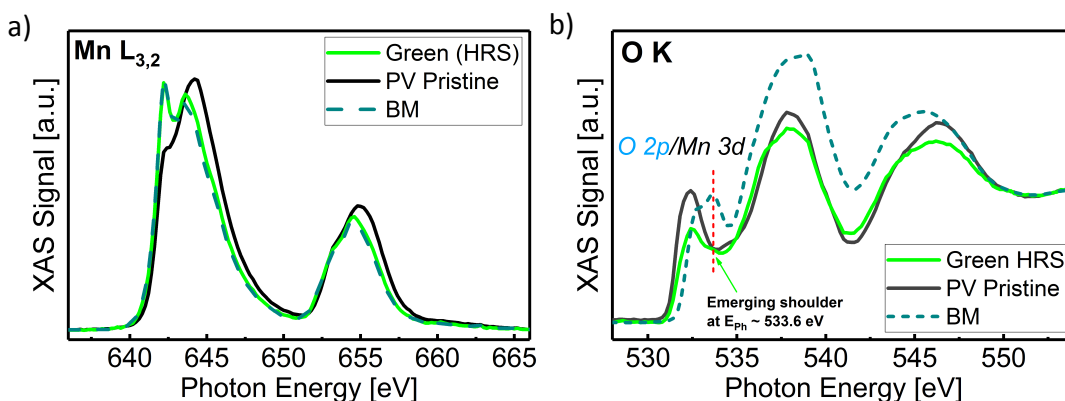


**Figure 8.20:** Spectral comparison of the LSMO pristine PV state, the high resistive state (HRS), and the LSMO reference sample in the BM phase. a) The Mn  $L_{3,2}$ -edge of the HRS and the BM phase reveals a similar spectral shape, except of a very small shoulder at  $h\nu = 645.5$  eV, and a small deviation in the aspect ratio of the maximum peak intensities. b) The spectral line shape of the O  $K$ -edge shows a significant deviation comparing the HRS and the BM phase.

and the O  $K$ -edges show considerable differences, there are spectral indications for a possible BM phase within the modified regions. One could think of a mixture or coexistence of the PV and the BM phase. A lateral distribution of PV and BM domains with a diameter of a few to several tens of nanometers could be the origin of a superimposed spectral signature. As long as the diameter of the domains does not exceed the resolution limit of the microscope, which amounts currently to  $\sim 100$  nm, the spectrum would reflect a superposition of both phases. A further scenario might be a vertical arrangement of BM layers at the topmost surface region followed by PV layers.

Following the trace of a possible mixture of BM and PV phases within the modified areas, we decomposed the green HRS spectrum by a linear combination of the PV pristine state and the measured BM reference, as it can be seen in Fig. 8.21. The symbols denote the measured spectrum according to the green cluster, the filled grey and cyan coloured curves indicate the pristine perovskite phase and the brownmillerite reference, respectively. The red curve gives the fitting result from the Levenberg-Marquardt algorithm, as it is already performed in Sect. 8.2.2.

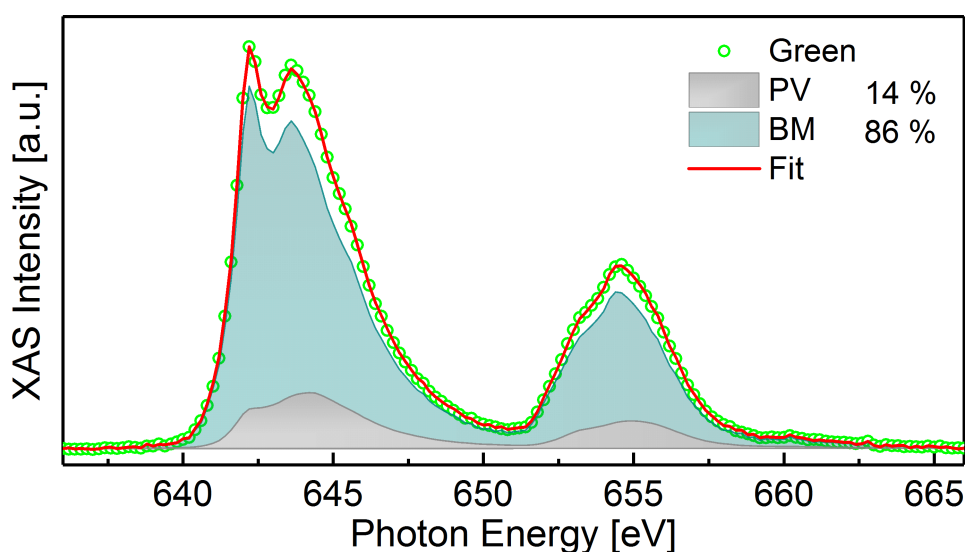


**Figure 8.21:** Decomposition of the measured spectra by linear superposition of the BM reference and the pristine state. The curve fitting procedure was performed by applying the Levenberg-Marquardt-algorithm.

We obtain a precise reproduction of the green spectrum by the best-fit curve. The calculation reveals a relative contribution of 14 and 86 % for the PV and the BM phase, respectively. So far, the concept of coexisting structural phases seems to work. But, as it is already discussed in Sect. 8.2.2, the analysis or the decomposition of the O  $K$ -edge is not straightforward. Also here, there is no

satisfying fit.

Complementary, the BM reference sample was probed by circularly polarized X-rays in order to check for possible XMCD signals. The XMCD analysis of the BM sample does not reveal any ferromagnetic signal, which is in agreement with the reported magnetic behaviour as the BM phase should be in a paramagnetic state at room temperature ( $T_N = 30$  K). Relating this result to the decreasing XMCD signal of the areas treated with a positive voltage, this could hint to a mixture of a perovskite and a brownmillerite structure in the areas +4 V and +5 V.

While the XMCD results and the analysis of the Mn L-edge support the picture of a coexisting BM phase in the areas treated with +4 V and +5 V, the O K-edge is not evidential. Thus, in order to answer the question about a brownmillerite phase within these electrically modified regions a careful structural study is required that will be the subject of future investigations.



## CHAPTER 9

---

### Summary and Conclusions

---

The scope of this thesis was to study a resistive switching magneto-ionic model system with respect to the correlation of an electric field-directed migration of oxygen vacancies and accompanying changes of the materials' chemical and physical properties. The ferromagnetic transition metal oxide,  $\text{La}_{0.7}\text{Sr}_{0.3}\text{MnO}_{3-\delta}$ , is an excellent sample material, since it exhibits a strong interplay between orbital, lattice, charge and spin. Thus, the distribution of oxygen vacancies has profound effects on the electronic, magnetic and structural behaviour. In order to investigate the underlying microscale redox processes, we employed local conductivity atomic force microscopy and X-ray photoemission electron microscopy.

As a prerequisite for a microscale analysis, the thin film growth process was optimized to ensure high quality. LSMO films were grown on a  $\text{Nb}:\text{SrTiO}_3$  substrate in a layer-by-layer growth mode utilizing high-pressure RHEED-assist-

ed pulsed laser deposition. A variety of characterization methods was used to investigate the quality of the thin film system. The morphology and the crystal structure were characterized by AFM and XRD confirming an epitaxial, single crystalline film and an atomically flat surface. The electronic structure was probed by HAXPES, which showed a well-screened feature at the Mn  $2p$  core level indicating a conductive state. The expected manganese valence state ( $\text{Mn}^{3.3}$ ) was validated by the Mn  $3s$  exchange splitting. Moreover, we performed a magnetic characterization using vibrating sample magnetometry. The measurement along the magnetic (011) easy axis yielding in a Curie temperature of  $T_C = 347$  K and a saturation magnetization  $M_{Sat} = 3.7 \pm 0.37 \mu_B/\text{f.u.}$  ( $3.4 \pm 0.34 \mu_B/\text{f.u.}$ ) for a 20 nm (10 nm) thick LSMO thin film. A complementary element-selective XMCD study showed the typical XMCD fingerprint of

LSMO and confirmed the total magnetic moment determined by VSM. Next, we confirmed the feasibility of resistive switching in LSMO in ambient atmosphere. In a vertical switching geometry, the correct switching parameters were determined. It turned out that a voltage set of same amplitude and opposite polarity (+5 V/-5 V) gives optimal results in terms of reproducibility and a maximum ON/OFF ratio ( $\sim 600$ ). Here, the resistive switching process is governed by a redistribution of oxygen vacancies. The electric field-directed migration of oxygen vacancies leads to an incorporation or release of oxygen anions via a surface exchange process driven by the gradient of the chemical potential of oxygen across the LSMO/ambient atmosphere interface. The resulting local change of the oxygen concentration considerably affects the double exchange mechanism. Moreover, the redistribution of oxygen vacancies also modulates the Schottky barrier at the interface between the thin film and the electrode altering significantly the resistance. However, while a reversible switching behaviour is observed in ambient atmosphere, a non-reversible switching process from the pristine state into the HRS is obtained in vacuum. A reasonable approach to this observation is the missing oxygen reservoir, which is required to be in exchange with the LSMO thin film.

As a preparation for the spectral analysis of the underlying voltage-driven microscale redox processes,  $2 \times 2 \mu\text{m}^2$  sized areas were scanned with constantly applied voltages by means of LC-AFM. A sequence of these areas with different polarities between -3 and +5 V was performed in order to probe the effect of the strength of the applied voltage amplitude.

A subsequent PEEM study allowed us to directly compare the magnetic and chemical properties of the electrically modified regions and set them into relation to each other. Chemical and magnetic contrast images and spectra were recorded for the Mn  $L_{3,2}$ -, O  $K$ -, and La  $M_{5,4}$ -edges. A following principle component analysis of these data improved the signal-to-noise ratio substantially and enhanced the chemical contrast and resolution. Significant chemical contrasts were observed for the areas modified with +4 and +5 V. The according spectra of the Mn  $L_{3,2}$ -edge showed an emerging low energy peak at  $h\nu = 642.2$  eV with increasing positive voltage amplitude. This feature is ascribed to the appearance of  $\text{Mn}^{2+}$  cations. Moreover, a decreasing O  $2p$ -Mn  $3d$  hybridization peak at the O  $K$ -edge was observed for increasing positive voltages. From this results we deduce a release of the oxygen from the LSMO thin film into the vacuum. Thus, the increased oxygen vacancy concentration is compensated by electrons. Consequently, a valence change with an arising  $\text{Mn}^{2+}$  cation contribution preserves the charge neutrality in the thin film system.

The question about changes of the A-site cations still remains open, since we had access to the La  $M_{5,4}$ -edge only. But, so far, there were no indications for A-site variations, like cationic segregation towards the surface, for instance. Spin-sensitive and element-selective XMCD-PEEM measurements across the Mn  $L_{3,2}$ -edge at room temperature completed the picture of the foregoing results about the interplay between changes in resistivity, Mn valence and

magnetic ordering. Consistently, the XMCD signal showed a significant decrease of the ferromagnetic response, which accumulates for +4 and +5 V. For a straightforward explanation one can again refer to a perturbed double-exchange mechanism. Since the interlinking oxygen anion between the  $\text{Mn}^{3+}$  and  $\text{Mn}^{4+}$  cations are crucial in order to mediate the ferromagnetic alignment of the electronic spin states, oxygen deficiency leads to a weakening of the ferromagnetic coupling.

According to recent studies, we also followed the trace of a possible structural phase transition from a perovskite to a brownmillerite phase, which comes along with the transition from metal to insulator. We investigated the spectral fingerprint of a  $\text{La}_{0.7}\text{Sr}_{0.3}\text{MnO}_{2.5}$  brownmillerite reference sample and compared it to the PEEM results. It turned out, that the Mn  $L_{3,2}$ -edge of the HRS can be reproduced by a linear superposition of the brownmillerite- and the pristine perovskite phase. Also the paramagnetic behaviour of the BM phase at room temperature could be a possible reason for the considerably reduced XMCD signal. However, the decomposition of the O  $K$ -edge is not straightforward and showed no evidential results. Thus, in the framework of the present thesis, the question about a possible coexistence of a brownmillerite phase within our electrically modified regions cannot be clearly answered and remains open.

As a future perspective a microscopic structural investigation of the LSMO film after chemical reduction could give important insights. In particular, a complementary structural depth profile by means of TEM is planned for the future. TEM of LSMO cross sections could clarify the question about a possible brownmillerite structure in the resistively switched areas. However, such experiments have to be carried out with utmost care, making sure that the preparation of the cross sections (i.e. cutting with a focused ion beam) does not affect the sample itself, and, likely, necessitating modification of larger areas.

Despite of the actual structural behaviour, we have identified clear chemical and magnetic fingerprints related to ON/OFF states. The next step on the way to in-operando experiments would be to establish well-defined microstructured top electrodes. The aim is to design and to fabricate devices for in-situ and in-operando characterizations in PEEM. The use of contact electrodes, however, cause a damping of the chemical signal originating from the functional layer. Here, the use of ultra-thin top electrodes like graphene could significantly enhance the yield of photoelectrons. Another possibility is to exploit the increased effective attenuation length of a hard X-ray excitation, which is realized in a HAXPEEM facility.

The ultimate goal is the investigation of the switching dynamics on picosecond timescales. An appropriate pump-probe experiment could be realized at the Nanospectroscopy beamline at the Elettra synchrotron in Trieste. Locatelli and co workers performed a proof-of-concept experiment, which demonstrates the feasibility of a time-resolved XAS measurement on magnetic domains in

magnetite islands on Re (0001) [165]. However, a stable switching mechanism is required in which both the LRS and the HRS are identically reproduced for each switching cycle. Moreover, to gain a significant XAS signal a large endurance performance is needed in order to support a required number of single bunch detection events of more than 60 million [166]. So far, these conditions have been observed solely for heterostructure devices with thick top electrodes of several tens of nanometers [167]. It is assumed that thick electrodes provide a sufficiently large oxygen reservoir being in constant exchange with the functional layer [144]. In contrast, a release of oxygen into the vacuum is observed for ultra-thin electrodes, which shortens the lifetime of switching devices. Thus, the investigation of the switching dynamics, using a PEEM pump-probe experiment, which requires ultra-thin top electrodes, requires further research activities.

## APPENDIX A

---

### Reciprocal Space Map (RSM)

---

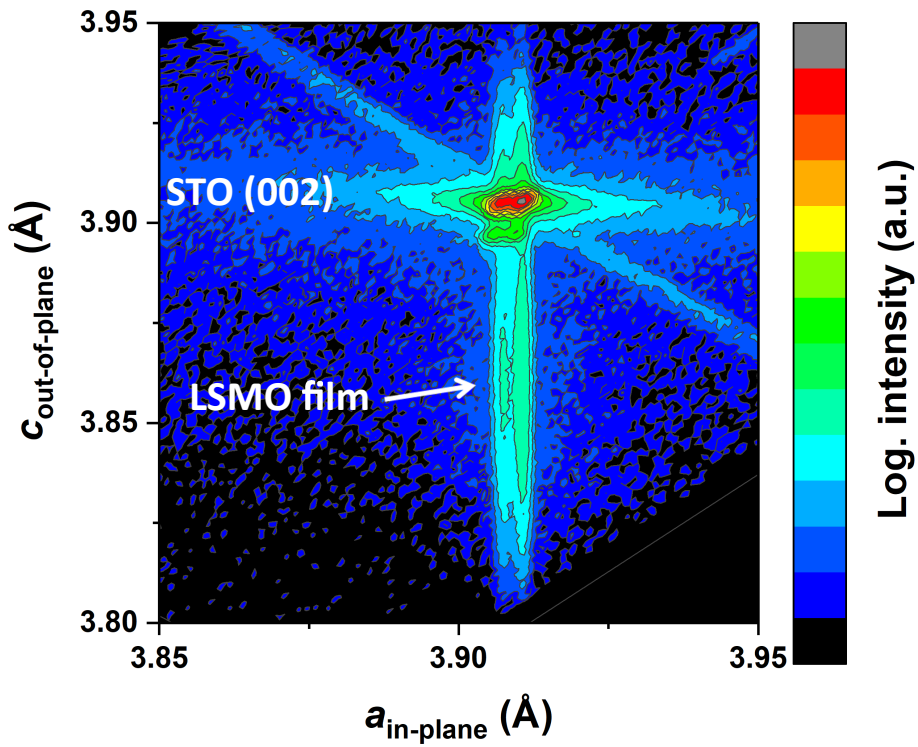


**Figure A.1:** XRD reciprocal space map (RSM) around the LSMO (002) reflection from an epitaxially grown  $\text{La}_{0.7}\text{Sr}_{0.3}\text{MnO}_3$  thin film on top of a  $\text{Nb:SrTiO}_3$  (001) substrate. The LSMO thin film is fully strained in the in-plane direction.

Reciprocal space mapping (RSM) were performed on a 10 nm thick  $\text{La}_{0.7}\text{Sr}_{0.3}\text{MnO}_3$  thin film, which was epitaxially grown on a Nb:STO (001) substrate<sup>1</sup>. Since there is no separation of intensity maxima along the  $a_{ip}$ -axis, we conclude that the LSMO film is fully strained and adapts the in-plane lattice constant of the STO. Further, a "rod-like" diffraction pattern is observed, which can be assigned to a pseudotetragonal symmetry [168].

---

<sup>1</sup> RSM measurement was performed by Moritz Weber, Forschungszentrum Jülich GmbH, Peter-Grünberg-Institute 7.

## APPENDIX B

### Magnetic Characterization of varying LSMO Thin Film Thicknesses

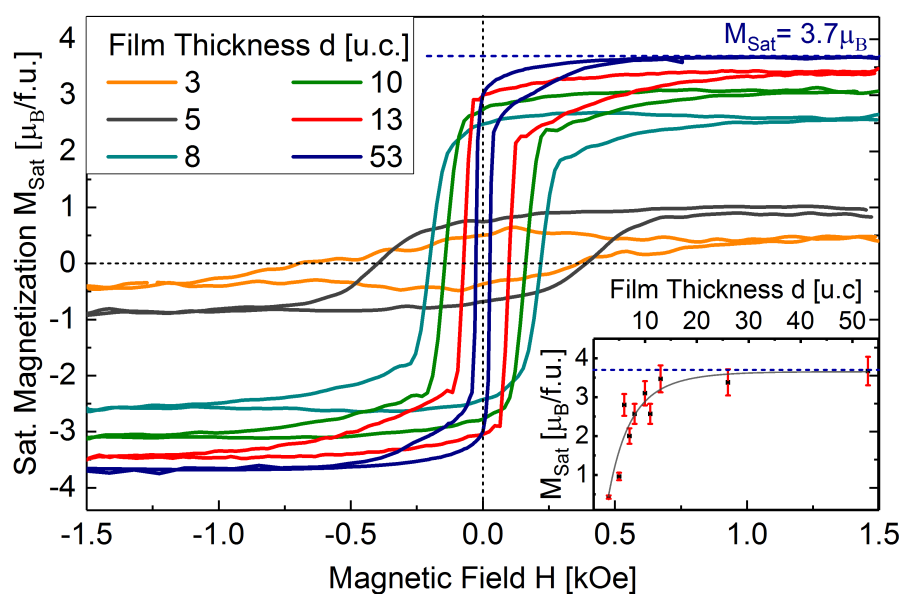


**Figure B.1:** VSM hysteresis loops of  $\text{La}_{0.7}\text{Sr}_{0.3}\text{MnO}_3$  thin films on  $\text{SrTiO}_3$  (001), measured at 10 K. The external magnetic field of  $H = 1.5$  kOe was applied along the (011) easy-axis. The diamagnetic contribution of the substrate has already been subtracted. The inset shows the development of the saturation magnetization  $M_{Sat}$  as a function of the  $\text{La}_{0.7}\text{Sr}_{0.3}\text{MnO}_3$  film thickness. The dashed line indicates the diamagnetic signal for a layer thickness of 2 u.c.

Based on the optimized growth parameters for a heteroepitaxial growth of  $\text{La}_{0.7}\text{Sr}_{0.3}\text{MnO}_3$  thin films on  $\text{SrTiO}_3$  (001) the magnetic properties were investigated for varying thicknesses. In particular, the focus was directed to the influence of the reduced dimensionality on the magnetic phase transition from a ferromagnetic- to a paramagnetic state. For this purpose, a detailed thickness study was performed, in which the thickness was gradually reduced from  $\sim 20$  nm (bulk) down to the ultra-thin film regime of  $\sim 0.8$  nm.

The hysteresis loops of all samples were recorded at  $T = 10$  K. Linear backgrounds have been fitted to the high-field tails of the raw signal and subtracted from the raw data in order to remove the diamagnetic contribution from the substrate. Representative hysteresis loops of the thickness study are depicted in Fig. B.1. All samples ranging between a thickness of  $d = 3$  and 53 u.c., show a ferromagnetic behaviour. However, large differences in the saturation magnetization values can be observed. The bulk sample with a thickness of 53 u.c. reaches a saturation magnetization of  $\sim 3.6 \mu_B/\text{f.u.}$ , whereas, the 3 u.c. thick sample exhibits a reduced value of  $M_{\text{Sat}} = 0.43 \mu_B/\text{f.u.}$  A decrease of the saturation magnetization (Fig. B.1 inset) as well as an increase in the coercive field  $H_C$  is observed for thicknesses below 13 u.c. ( $\sim 4.8$  nm). The 2 u.c. sample does not reveal any ferromagnetic signal, which leads to a magnetic phase transition between 2 and 3 u.c.

The dependence of the saturation magnetization  $M_{\text{Sat}}$  on the temperature  $T$  is shown in Fig. B.1. The bulk samples of 53 and 26 u.c. exhibit a Curie temperature of  $\sim 345$  K and show a sharp phase transition from the ferromagnetic to the paramagnetic state. Then, the Curie temperature gradually decreases until 8 u.c. ( $T_C \sim 270$  K). Between 8 and 6 u.c., we observe a jump of 110 K and finally the Curie temperature reaches its lowest value of  $\sim 80$  K for a layer thickness of 3 u.c. Consistently, the samples between 6 and 3 u.c. exhibit a broadened phase transition, indicating stoichiometric inhomogeneities in the  $\text{La}_{0.7}\text{Sr}_{0.3}\text{MnO}_3$  thin film. Finally, Fig. B.3 shows the correlation between the coercive field and the Curie temperature as a function of the film thickness.  $H_C$  and  $T_C$  are nearly constant for thicknesses down to 13 u.c. Further reduction of the layer thickness results in a significant change of the magnetic behaviour, although the films remain ferromagnetic down to three unit cells ( $\sim 1.2$  nm).

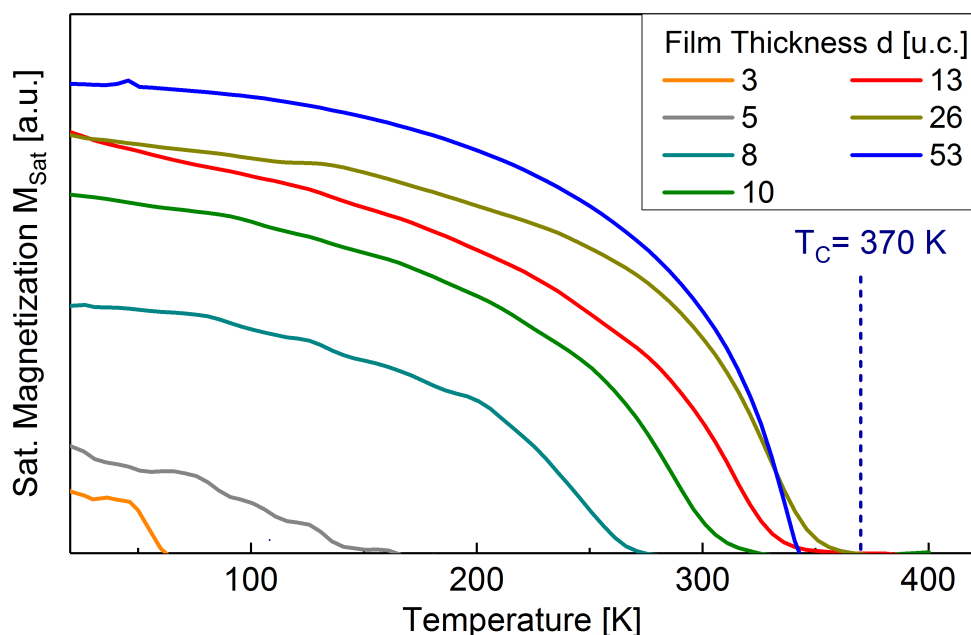


**Figure B.2:** Temperature dependent saturation magnetization for an applied external magnetic field of  $H = k\text{Oe}$ . All samples were field cooled at 1000 Oe from 300 K along the (011) direction before the measurements were performed. The inset reveals the development of the Curie temperature depending on the  $\text{La}_{0.7}\text{Sr}_{0.3}\text{MnO}_3$  film thickness.

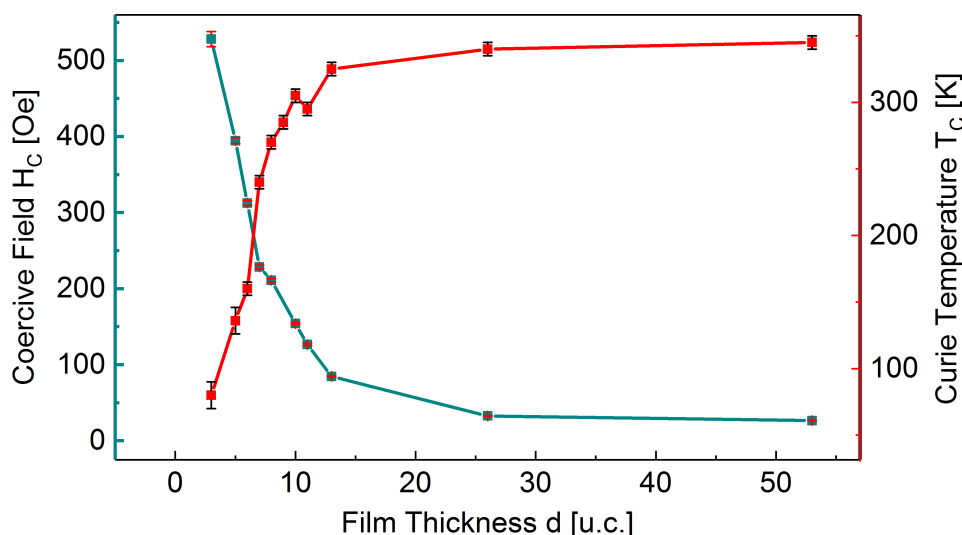


**Figure B.3:** Comparison of the coercive field  $H_C$  and the Curie temperature  $T_C$  of  $\text{La}_{0.7}\text{Sr}_{0.3}\text{MnO}_3$  depending on varying thicknesses  $d$ . The coercive field  $H_C$  decreases with increasing Curie temperature  $T_C$ .



## APPENDIX C

---

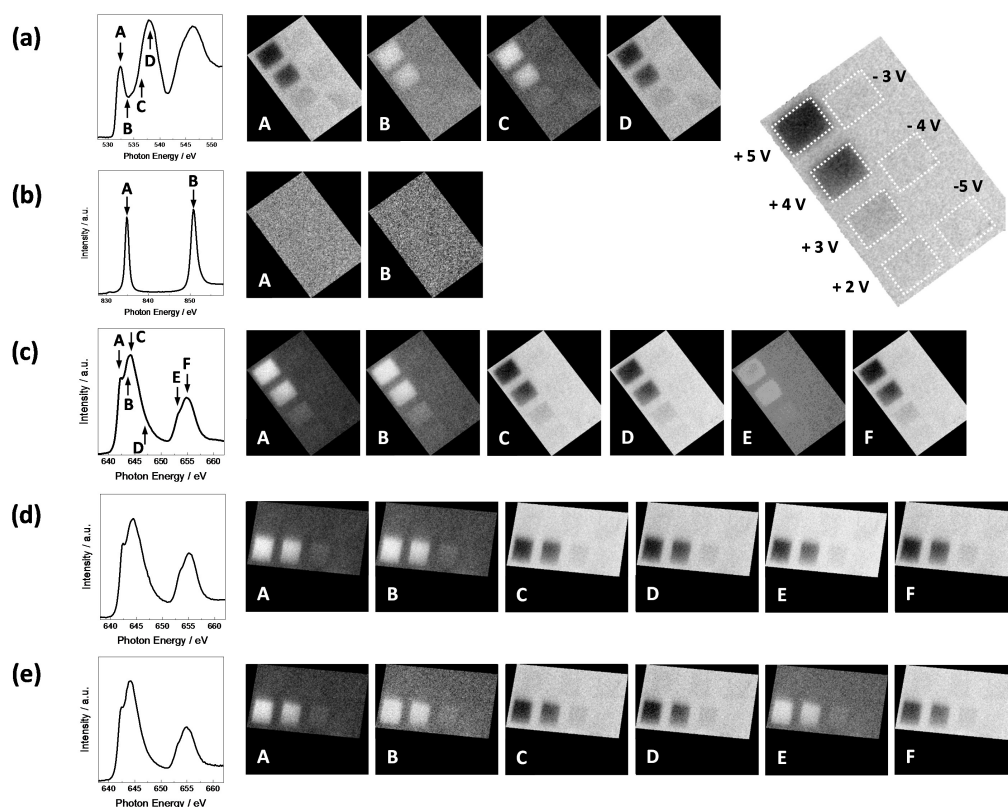
### Principal Component Analysis

---

The XAS-PEEM data was analyzed as described in detail elsewhere [149]. First, the field of view of the PEEM stack was reduced to the region of interest (ROI) including the areas treated with voltage pulses. The ROI included a total number of seven treated areas as shown in the sketch in Fig. C.1 in the upper right corner.

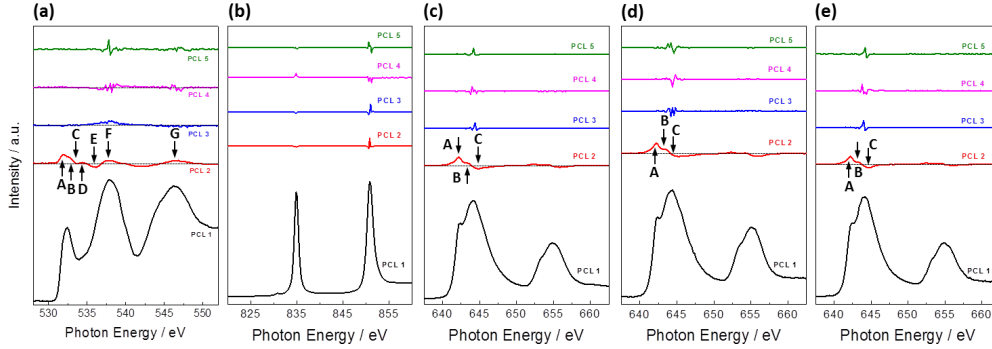
Following the procedure as described in [149], each pixel of the ROI was assigned to a full XAS spectrum vs. energy covered by the PEEM image stack. Using principal component analysis (PCA) spectral variations are identified with spatial resolution and noise is reduced substantially. This is done by reducing the original data to a small number of relevant principal components (PC) and principal component loadings (PCL) and their associated coefficients [147, 148] which are sufficient to describe the relevant spectral features. As shown in [149, 150], small signals mostly camouflaged by noise are easily detected and are mapped in PCA images which resemble the original PEEM data albeit with better contrast and resolution.

Fig. C.1 (a)-(e) show the PCA images at the O K-edge (a), the La M<sub>5,4</sub>-edge (b) and the Mn L<sub>3,2</sub>-edge for linear (c), left- (d) and right- (e) circular polarized light. For the data obtained at the O K-edge, PC 1 to 3 were considered, for La M<sub>5,4</sub>-edge and Mn L<sub>3,2</sub>-edge PC 1 to 2. The different images are obtained at the indicated spectral features. For better visibility, the intensity contrast as seen in the PCA images is enhanced using a histogram spread. At the O K-edge, all areas show a small reduction of the oxygen signal at all energies; safe for areas +5 and +4 V at features B and C, where the O 1s signal is enhanced. La is homogeneously distributed over the sample. The La signal is not affected in the areas.



**Figure C.1:** Mean XAS spectra and PCA images at the (a) O K-edge, (b) La  $M_{5,4}$  and the Mn  $L_{3,2}$ -edge for (c) linear, (d) left- and (e) right circular polarized light. (a)-(c) have been measured at  $\varphi = 0^\circ$  (azimuth), (d),(e) at  $\varphi = 45^\circ$ . The capital letters indicate the energies and spectral features as denoted in the PCA images. For the images at the Mn  $L_{3,2}$ -edge (c) - (e), the spectral features A-F refer to identical photon energies. The sketch in the upper right corner indicates the areas and the applied voltages. PCA images were obtained based on the principal components (a) 1 to 3 and (b)-(e) 1 to 2. To improve visibility, image contrast is enhanced using histogram spread.

The largest effect of the voltage treatment is found for the Mn signal: In the areas with applied positive voltage, the intensity of the Mn signal increases for features A, B for all polarizations. Features C, D, F show reduced intensity in the areas with positive voltages. Feature E, on the other hand shows a positive effect for linear- and right circular polarized light; however, a reduction of the Mn signal for left-circular polarized light. Areas with negative applied voltages are almost not affected in Mn signal intensity. In order to identify the spectral variations, Fig. C.2 shows the corresponding principal component loadings (PCL). PCL 1 resembles the mean spectrum, i.e. the average over all pixels in the ROI. Higher PCLs indicate local variations from the mean spectrum. For the O K-edge (a), deviations from PCL 1 are found in PCL 2 and 3. For higher PCL numbers, the curves cannot be distinguished from noise. For La  $M_{5,4}$  (b), no deviations from PCL 1 are observed at higher



**Figure C.2:** Principal component loadings (PCL) of the original PEEM spectra after PCA for the (a) O K-edge, (b) La  $M_{5,4}$ -edge and the Mn  $L_{3,2}$ -edge for (c) linear, (d) left- and (e) right circular polarized light. The data in (a)-(c) was obtained at  $\varphi = 0^\circ$ , (d),(e) at  $\varphi = 45^\circ$ . The first loading represents the mean spectrum averaged over all pixels in the ROI. Higher loadings correspond to deviations from the mean spectrum as found at distinct pixels. The curves are shifted along the ordinate to improve visibility. The former zero line is indicated for selected PCL curves as dotted black lines. Capital letters denote spectral features of the second PCL and correspond to PCA images in Fig. C.1. The spectral features A-C for Mn are located at those energies where the different oxidation states  $Mn^{2+}$ ,  $Mn^{3+}$ ,  $Mn^{4+}$  are expected.

PCL numbers; safe for tiny signals caused by small uncertainties in the peak position. For Mn  $L_{3,2}$  (c)-(e), deviations from PCL 1 are exclusively observed for PCL 2. Higher PCL numbers are dominated by noise. For further analysis of the data we therefore considered the following principal components: for the O K-edge, PC 1 to 3, for the La  $M_{5,4}$ -edge, PC 1 to 2 and for Mn  $L_{3,2}$ , PC 1 to 2. We emphasize that the dominant features A, B, C of Mn PCL 2 (c-e) are located where one expects spectral features for the different oxidation states  $Mn^{2+}$ ,  $Mn^{3+}$ ,  $Mn^{4+}$ . Note that in the PCL 2 curves, features A, B and C have opposite sign. The sign of a spectral feature in loadings does not a priori indicate a reduction or enhancement of spectral intensities. The final sign of the contribution to spectral intensity is determined by the product of loadings and coefficients. The latter may also be positive or negative. The conversion of the sign between A,B and C, however, remains unaffected. That is, if features A,B are locally enhanced, feature C is reduced and vice versa. The final sign of the contribution of features in the principal component loadings to the local spectra are shown with spatial resolution in mapping images of individual loadings. In mapping images, spectral changes caused by changes in oxidation states and/ or crystal structure are thereby assigned to distinct positions on the sample. Fig. C.3 shows (for selected photon energies, as indicated in Fig. C.1 of the supplement) the mapping of the second loading PCL 2, which represents the main deviation from the mean spectrum for the (a) O K-edge, and for the Mn  $L_{3,2}$  with (b) linear, (c) left-circular- and (d) right-circular polarized light. High/low intensity in the mapping images correspond to

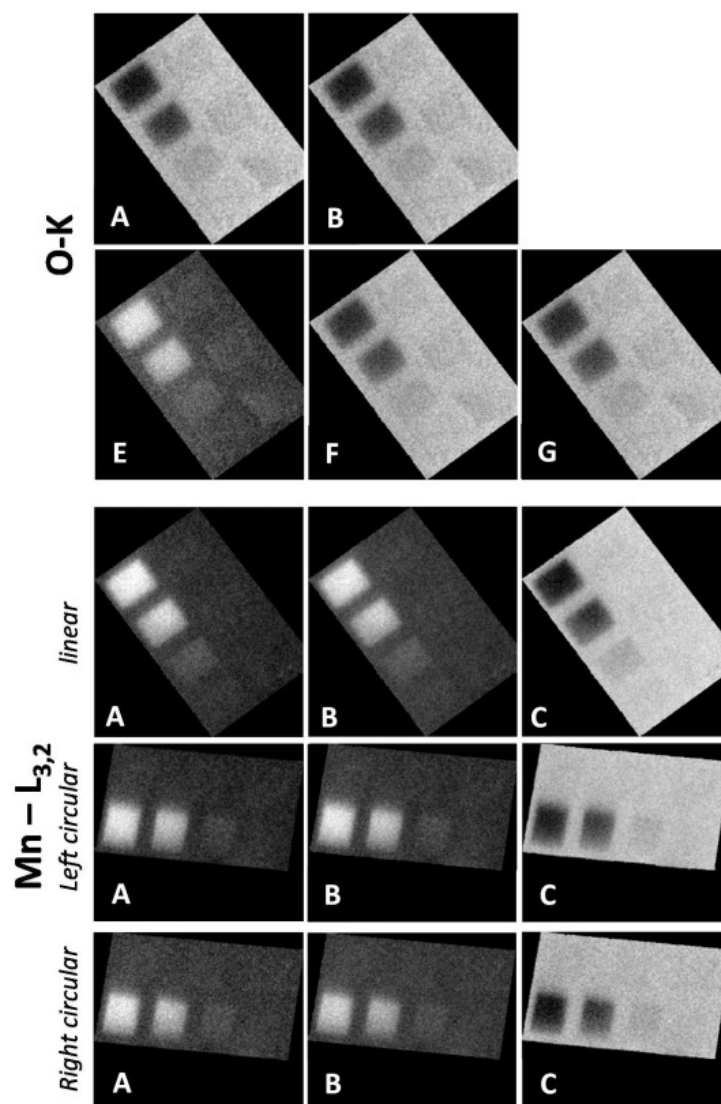


**Figure C.3:** Mapping images of the spectral loading PCL 2 for the O K- and the Mn  $L_{3,2}$ -edge as shown in Fig. C.2 a, c-e as red curves. For Mn, the spectral features A, B, C correspond to different oxidation states  $Mn^{2+}$ ,  $Mn^{3+}$ ,  $Mn^{4+}$ , respectively. For Mn, the linear polarized data was obtained from  $\varphi = 0^\circ$  azimuthal angle, the left- and right-circular polarized data from  $\varphi = 45^\circ$ . To improve visibility, image contrast is enhanced using histogram spread.

larger positive/negative contribution of the second principal component to the spectrum. For the O K-edge, the mapping images for A, B, F, G indicate that PCL 2 points toward a reduction of  $\text{Mn}^{2+}$  and  $\text{Mn}^{3+}$  (feature A and B) in both, HRS and LRS areas: the higher the applied voltage though, the stronger the reduction compared to the pristine state. That is, most of the reduction is found in the HRS areas. The mapping images show that the spectral intensity of PCL 2 at energies corresponding to feature E is enhanced for both, HRS and LRS areas. For Mn, features A, B, C are indicative of the different oxidation states  $\text{Mn}^{2+}$ ,  $\text{Mn}^{3+}$ ,  $\text{Mn}^{4+}$ . The mapping images for Mn in Fig. C.3 indicate that the PCL 2 contribution to the measured spectrum in the LRS areas is negligible. In the HRS areas  $\text{Mn}^{2+}$  and  $\text{Mn}^{3+}$  are enhanced, whereas  $\text{Mn}^{4+}$  is reduced.

# List of Tables

4.1	Specifications of the BESSY UE56-1 SGM beamline. .	41
7.1	Input parameters for the quantitative XMCD analysis and the resulting orbital, spin and total magnetic moment $m_l$ , $m_s$ and $m_{l+s}$ . The ratio of orbital to spin moment $m_l/m_s$ gives a quantity, which is dependent from $n_h$ and $P_C$ . . . . .	70
8.1	Median values of both the LRS and the HRS, and the ON/OFF ratio for the right switching amplitudes +5 V/-5 V. . . . .	75

---

## Bibliography

---

- [1] Sergei V. Kalinin and Nicola A. Spaldin. "Functional Ion Defects in Transition Metal Oxides". In: 341.6148 (2013), pp. 858–859. ISSN: 0036-8075. DOI: [10.1126/science.1243098](https://doi.org/10.1126/science.1243098).
- [2] M. A. Peña and J. L. G. Fierro. "Chemical Structures and Performance of Perovskite Oxides". In: *Chemical Reviews* 101.7 (2001), pp. 1981–2018. DOI: [10.1021/cr980129f](https://doi.org/10.1021/cr980129f).
- [3] Svein Stølen, Egil Bakken, and Chris E. Mohn. "Oxygen-deficient perovskites: linking structure, energetics and ion transport". In: *Phys. Chem. Chem. Phys.* 8 (4 2006), pp. 429–447. DOI: [10.1039/B512271F](https://doi.org/10.1039/B512271F).
- [4] Y. P. Yao et al. "Multi-state resistive switching memory with secure information storage in Au/BiFe<sub>0.95</sub>Mn<sub>0.05</sub>O<sub>3</sub>/La<sub>5/8</sub>Ca<sub>3/8</sub>MnO<sub>3</sub> heterostructure". In: *Applied Physics Letters* 100.19 (2012), p. 193504. DOI: [10.1063/1.4714514](https://doi.org/10.1063/1.4714514).
- [5] V. E. Heinrich and P. A. Cox. *The Surface Science of Metal Oxides*. 1994, pp. 158–161.
- [6] Noriaki Hamada et al. "Electronic band structure and lattice distortion in perovskite transition-metal oxides". In: *Physica B: Condensed Matter* 237-238 (1997), pp. 11–13. ISSN: 0921-4526. DOI: [10.1016/S0921-4526\(97\)00016-1](https://doi.org/10.1016/S0921-4526(97)00016-1).
- [7] Jak Chakhalian et al. "Colloquium: Emergent properties in plane view: Strong correlations at oxide interfaces". In: *Rev. Mod. Phys.* 86 (4 2014), pp. 1189–1202. DOI: [10.1103/RevModPhys.86.1189](https://doi.org/10.1103/RevModPhys.86.1189).
- [8] C. N. R. Rao. "Transition Metal Oxides". In: *Annual Review of Physical Chemistry* 40.1 (1989), pp. 291–326. DOI: [10.1146/annurev.pc.40.100189.001451](https://doi.org/10.1146/annurev.pc.40.100189.001451).
- [9] M. Bowen et al. "Nearly total spin polarization in La<sub>2/3</sub>Sr<sub>1/3</sub>MnO<sub>3</sub> from tunneling experiments". In: *Applied Physics Letters* 82.2 (2003), pp. 233–235. DOI: [10.1063/1.1534619](https://doi.org/10.1063/1.1534619).

- [10] A. Urushibara et al. "Insulator-metal transition and giant magnetoresistance in  $\text{La}_{1-x}\text{Sr}_x\text{MnO}_3$ ". In: *Phys. Rev. B* 51 (20 1995), pp. 14103–14109. DOI: [10.1103/PhysRevB.51.14103](https://doi.org/10.1103/PhysRevB.51.14103).
- [11] Andy Thomas and Elisabetta Chicca. "Tunnel junction based memristors as artificial synapses". In: *Frontiers in Neuroscience* 9 (2015), p. 241. ISSN: 1662-453X. DOI: [10.3389/fnins.2015.00241](https://doi.org/10.3389/fnins.2015.00241).
- [12] "Third-Generation Hard X-ray Synchrotron Radiation Sources, 2nd Edition". In: ed. by D.M. Mills. John Wiley Sons, Inc., New York, 2002.
- [13] "Zahlenwerte und Funktionen 1.4, Atom- und Molekularphysik, 4. Teil Kristalle". In: ed. by Landolt-Börnstein. Springer Berlin, S.524 ff., 1955.
- [14] Maryvonne Hervieu. "The Surface Science of Metal Oxides. By V. E. Henrich and P. A. Cox, Cambridge University Press, Cambridge 1994, XIV, 464 pp., hardcover, £ 55.00, ISBN 0-521-44389-X". In: *Advanced Materials* 7.1 (1995), pp. 91–92. DOI: [10.1002/adma.19950070122](https://doi.org/10.1002/adma.19950070122).
- [15] "Physics of Magnetism and Magnetic Materials". In: ed. by K.H.J. Buschow und F.R. de Boer. Kluwer Academic/Plenum Publishers, 2003.
- [16] Jonathan R. Petrie et al. "Strain Control of Oxygen Vacancies in Epitaxial Strontium Cobaltite Films". In: *Advanced Functional Materials* 26.10 (2016), pp. 1564–1570. DOI: [10.1002/adfm.201504868](https://doi.org/10.1002/adfm.201504868).
- [17] Jiagang Wu et al. "Migration Kinetics of Oxygen Vacancies in Mn-Modified  $\text{BiFeO}_3$  Thin Films". In: *ACS Applied Materials & Interfaces* 3.7 (2011). PMID: 21675732, pp. 2504–2511. DOI: [10.1021/am2003747](https://doi.org/10.1021/am2003747).
- [18] Dustin A. Gilbert et al. "Ionic tuning of cobaltites at the nanoscale". In: *Physical Review Materials* 2.10 (2018). ISSN: 2475-9953. DOI: [10.1103/physrevmaterials.2.104402](https://doi.org/10.1103/physrevmaterials.2.104402).
- [19] Nianpeng Lu et al. "Electric-field control of tri-state phase transformation with a selective dual-ion switch". In: *Nature* 546.7656 (June 2017), pp. 124–128. ISSN: 1476-4687.
- [20] K. Duschek et al. "Research Update: Magnetoionic control of magnetization and anisotropy in layered oxide/metal heterostructures". In: *APL Materials* 4.3 (2016), p. 032301. DOI: [10.1063/1.4942636](https://doi.org/10.1063/1.4942636).
- [21] Bin Cui et al. "Reversible Ferromagnetic Phase Transition in Electrode-Gated Manganites". In: *Advanced Functional Materials* 24.46 (2014), 7233–7240. DOI: [10.1002/adfm.201402007](https://doi.org/10.1002/adfm.201402007).
- [22] Alan Molinari, Horst Hahn, and Robert Kruk. "Voltage-Controlled On/Off Switching of Ferromagnetism in Manganite Supercapacitors". In: *Advanced Materials* 30.1 (2018), p. 1703908. DOI: [10.1002/adma.201703908](https://doi.org/10.1002/adma.201703908).
- [23] A. J. Grutter et al. "Reversible control of magnetism in  $\text{La}_{0.67}\text{Sr}_{0.33}\text{MnO}_3$  through chemically-induced oxygen migration". In: *Applied Physics Letters* 108.8 (2016), p. 082405. DOI: [10.1063/1.4942645](https://doi.org/10.1063/1.4942645).

- [24] Lide Yao, Sampo Inkinen, and Sebastiaan van Dijken. "Direct observation of oxygen vacancy-driven structural and resistive phase transitions in  $\text{La}_{2/3}\text{Sr}_{1/3}\text{MnO}_3$ ". In: *Nature communications* 8 (2017), p. 14544. ISSN: 2041-1723. DOI: [10.1038/ncomms14544](https://doi.org/10.1038/ncomms14544).
- [25] Lei Cao et al. "Reversible Control of Physical Properties via an Oxygen-Vacancy-Driven Topotactic Transition in Epitaxial  $\text{La}_{0.7}\text{Sr}_{0.3}\text{MnO}_{3-\delta}$  Thin Films". In: *Advanced Materials* 31.7 (2019), p. 1806183. DOI: [10.1002/adma.201806183](https://doi.org/10.1002/adma.201806183).
- [26] "From Fundamentals of Nanoionic Redox Processes to Memristive Device Applications". In: *Resistive Switching*. Ed. by D. Lelmini and R. Waser. Wiley-VCH Verlag GmbH Co. KGaA, 2016. ISBN: 978-3-527-33417-9.
- [27] Rainer Waser et al. "Redox-Based Resistive Switching Memories – Nanoionic Mechanisms, Prospects, and Challenges". In: *Advanced Materials* 21.25-26 (2009), pp. 2632–2663. DOI: [10.1002/adma.200900375](https://doi.org/10.1002/adma.200900375).
- [28] S. Balatti et al. "Multiple Memory States in Resistive Switching Devices Through Controlled Size and Orientation of the Conductive Filament". In: *Advanced Materials* 25.10 (2013), pp. 1474–1478. DOI: [10.1002/adma.201204097](https://doi.org/10.1002/adma.201204097).
- [29] Lide Yao, Sampo Inkinen, and Sebastiaan Dijken. "Direct observation of oxygen vacancy-driven structural and resistive phase transitions in  $\text{La}_{2/3}\text{Sr}_{1/3}\text{MnO}_3$ ". In: *Nature Communications* 8 (Feb. 2017), p. 14544. DOI: [10.1038/ncomms14544](https://doi.org/10.1038/ncomms14544).
- [30] A. Koehl et al. "Evidence for multifilamentary valence changes in resistive switching  $\text{SrTiO}_3$  devices detected by transmission X-ray microscopy". In: *APL Materials* 1.4 (2013), p. 042102. DOI: [10.1063/1.4822438](https://doi.org/10.1063/1.4822438).
- [31] J. Joshua Yang et al. "Memristive switching mechanism for metal/oxide/metal nanodevices". In: *Nature Nanotechnology* 3.7 (2008), pp. 429–433. DOI: [10.1038/nnano.2008.160](https://doi.org/10.1038/nnano.2008.160).
- [32] Y. B. Nian et al. "Evidence for an Oxygen Diffusion Model for the Electric Pulse Induced Resistance Change Effect in Transition-Metal Oxides". In: *Phys. Rev. Lett.* 98 (14 2007), p. 146403. DOI: [10.1103/PhysRevLett.98.146403](https://doi.org/10.1103/PhysRevLett.98.146403).
- [33] F.A. Kröger and H.J. Vink. "Relations between the Concentrations of Imperfections in Crystalline Solids". In: ed. by Frederick Seitz and David Turnbull. Vol. 3. Solid State Physics. Academic Press, 1956, 307–435. DOI: [10.1016/S0081-1947\(08\)60135-6](https://doi.org/10.1016/S0081-1947(08)60135-6).
- [34] Krzysztof Szot et al. "Switching the electrical resistance of individual dislocations in single-crystalline  $\text{SrTiO}_3$ ". In: *Nature Materials* 5.4 (Apr. 2006), pp. 312–320. ISSN: 1476-4660. DOI: [10.1038/nmat1614](https://doi.org/10.1038/nmat1614).
- [35] M. Wojtyniak et al. "Electro-degradation and resistive switching of Fe-doped  $\text{SrTiO}_3$  single crystal". In: *Journal of Applied Physics* 113.8 (2013), p. 083713. DOI: [10.1063/1.4793632](https://doi.org/10.1063/1.4793632).

- [36] Doo Seok Jeong et al. "Characteristic electroforming behavior in Pt/TiO<sub>2</sub>/Pt resistive switching cells depending on atmosphere". In: *Journal of Applied Physics* 104.12 (2008), p. 123716. DOI: [10.1063/1.3043879](https://doi.org/10.1063/1.3043879).
- [37] Rainer Waser. "Resistive non-volatile memory devices (Invited Paper)". In: *Microelectronic Engineering* 86.7 (2009). INFOS 2009, pp. 1925–1928. ISSN: 0167-9317. DOI: [10.1016/j.mee.2009.03.132](https://doi.org/10.1016/j.mee.2009.03.132).
- [38] D.I. Khomskii and G.A. Sawatzky. "Interplay between spin, charge and orbital degrees of freedom in magnetic oxides". In: *Solid State Communications* 102.2 (1997). Highlights in Condensed Matter Physics and Materials Science, pp. 87–99. ISSN: 0038-1098. DOI: [10.1016/S0038-1098\(96\)00717-X](https://doi.org/10.1016/S0038-1098(96)00717-X).
- [39] Stephan Menzel et al. "Origin of the Ultra-nonlinear Switching Kinetics in Oxide-Based Resistive Switches". In: *Advanced Functional Materials* 21.23 (2011), pp. 4487–4492. DOI: [10.1002/adfm.201101117](https://doi.org/10.1002/adfm.201101117).
- [40] Ruth Muenstermann et al. "Correlation between growth kinetics and nanoscale resistive switching properties of SrTiO<sub>3</sub> thin films". In: *Journal of Applied Physics* 108.12 (2010), p. 124504. DOI: [10.1063/1.3520674](https://doi.org/10.1063/1.3520674).
- [41] Akihito Sawa. "Review". English. In: *Materials Today* 11.6 (2008), pp. 28–36. DOI: [10.1016/S1369-7021\(08\)70119-6](https://doi.org/10.1016/S1369-7021(08)70119-6).
- [42] Gang He and Z. Sun. *High-k Gate Dielectrics for CMOS Technology*. Aug. 2012. DOI: [10.1002/9783527646340](https://doi.org/10.1002/9783527646340).
- [43] Ee Wah Lim and Razali Ismail. "Conduction Mechanism of Valence Change Resistive Switching Memory: A Survey". In: *Electronics* 4 (Sept. 2015), pp. 586–613. DOI: [10.3390/electronics4030586](https://doi.org/10.3390/electronics4030586).
- [44] M. S. Tyagi. "Physics of Schottky Barrier Junctions". In: *Metal-Semiconductor Schottky Barrier Junctions and Their Applications*. Ed. by B. L. Sharma. Boston, MA: Springer US, 1984, pp. 1–60. ISBN: 978-1-4684-4655-5. DOI: [10.1007/978-1-4684-4655-5\\_1](https://doi.org/10.1007/978-1-4684-4655-5_1).
- [45] C.J. Schmitz. "Operando X-ray photoemission electron microscopy (XPEEM) investigations of resistive switching metal-insulator-devices". PhD thesis. Research Centre Jülich GmbH, PGI-6, 2017.
- [46] Shimeng Yu, Ximeng Guan, and H.-S. Philip Wong. "Conduction mechanism of TiN/HfO<sub>x</sub>/Pt resistive switching memory: A trap-assisted-tunneling model". In: *Applied Physics Letters* 99.6 (2011), p. 063507. DOI: [10.1063/1.3624472](https://doi.org/10.1063/1.3624472).
- [47] Fu-Chien Chiu. "A Review on Conduction Mechanisms in Dielectric Films". In: *Advances in Materials Science and Engineering* 2014 (Feb. 2014), pp. 1–18. DOI: [10.1155/2014/578168](https://doi.org/10.1155/2014/578168).
- [48] S. M. Sze and K.K. Ng. "Physics of Schottky Barrier Junctions". In: *Physics of semiconductor devices*. Ed. by Hoboken and 3rd edition N.J. Wiley-Interscience, 2007. ISBN: 0-471-14323-5.
- [49] Y.Q. Zhu et al. "Measurement and analysis of substrate leakage current of RF mems capacitive switches". English. In: *Microelectronics Reliability* 54.1 (2014), pp. 152–159. DOI: [10.1016/j.microrel.2013.07.011](https://doi.org/10.1016/j.microrel.2013.07.011).

- [50] B. Majkusiak et al. "Modeling and Simulation Approaches for Gate Current Computation". In: *Nanoscale CMOS*. John Wiley Sons, Ltd, 2013. Chap. 7, pp. 213–257. ISBN: 9781118621523. DOI: [10.1002/9781118621523.ch7](https://doi.org/10.1002/9781118621523.ch7).
- [51] G.H. Jonker and J.H. Van Santen. "Ferromagnetic compounds of manganese with perovskite structure". In: *Physica* 16.3 (1950), pp. 337–349. ISSN: 0031-8914. DOI: [10.1016/0031-8914\(50\)90033-4](https://doi.org/10.1016/0031-8914(50)90033-4).
- [52] G.H. Jonker and J.H. Van Santen. "Magnetic compounds with perovskite structure III. ferromagnetic compounds of cobalt". In: *Physica* 19.1 (1953), pp. 120–130. ISSN: 0031-8914. DOI: [10.1016/S0031-8914\(53\)80011-X](https://doi.org/10.1016/S0031-8914(53)80011-X).
- [53] John B. Goodenough. "An interpretation of the magnetic properties of the perovskite-type mixed crystals  $\text{La}_{1-x}\text{Sr}_x\text{CoO}_3$ ". In: *Journal of Physics and Chemistry of Solids* 6.2 (1958), pp. 287–297. ISSN: 0022-3697. DOI: [10.1016/0022-3697\(58\)90107-0](https://doi.org/10.1016/0022-3697(58)90107-0).
- [54] G. H. Jonker. "Magnetic and Semiconducting Properties of Perovskites Containing Manganese and Cobalt". In: *Journal of Applied Physics* 37.3 (1966), pp. 1424–1430. DOI: [10.1063/1.1708498](https://doi.org/10.1063/1.1708498).
- [55] C.N.R. RAO and A.K. RAYCHAUDHURI. "COLOSSAL MAGNETORESISTANCE, CHARGE ORDERING AND OTHER NOVEL PROPERTIES OF MANGANATES AND RELATED MATERIALS". In: *Colossal Magnetoresistance, Charge Ordering and Related Properties of Manganese Oxides*, pp. 1–42. DOI: [10.1142/9789812816795\\_0001](https://doi.org/10.1142/9789812816795_0001).
- [56] C Rao et al. "Electronic phase separation in transition metal oxide systems". In: *Dalton transactions (Cambridge, England : 2003)* 19 (Nov. 2004), pp. 3003–11. DOI: [10.1039/b406785a](https://doi.org/10.1039/b406785a).
- [57] Clarence Zener. "Interaction between the  $d$ -Shells in the Transition Metals. II. Ferromagnetic Compounds of Manganese with Perovskite Structure". In: *Phys. Rev.* 82 (3 1951), pp. 403–405. DOI: [10.1103/PhysRev.82.403](https://doi.org/10.1103/PhysRev.82.403).
- [58] P. W. Anderson and H. Hasegawa. "Considerations on Double Exchange". In: *Phys. Rev.* 100 (2 1955), pp. 675–681. DOI: [10.1103/PhysRev.100.675](https://doi.org/10.1103/PhysRev.100.675).
- [59] P. G. de Gennes. "Effects of Double Exchange in Magnetic Crystals". In: *Phys. Rev.* 118 (1 1960), pp. 141–154. DOI: [10.1103/PhysRev.118.141](https://doi.org/10.1103/PhysRev.118.141).
- [60] Sayani Majumdar. "Pulsed laser deposition of  $\text{La}_{1-x}\text{Sr}_x\text{MnO}_3$ : Thin-film properties and spintronic applications". In: *Journal of Physics D Applied Physics* 47 (Dec. 2013), p. 034010. DOI: [10.1088/0022-3727/47/3/034010](https://doi.org/10.1088/0022-3727/47/3/034010).
- [61] Wilfrid Prellier, Mangala Singh, and Pattukkannu Murugavel. "The Single-Phase Multiferroic Oxides: From Bulk to Thin Film". In: *Journal of Physics: Condensed Matter* 17 (July 2005), R803. DOI: [10.1088/0953-8984/17/30/R01](https://doi.org/10.1088/0953-8984/17/30/R01).

- [62] W. Z. Yang et al. "Structure, magnetic, and dielectric properties of  $\text{La}_2\text{Ni}(\text{Mn}_{1-x}\text{Ti}_x)\text{O}_6$  ceramics". In: *Journal of Applied Physics* 111.8 (2012), p. 084106. DOI: [10.1063/1.4704392](https://doi.org/10.1063/1.4704392).
- [63] A.S. Dzunuzovic et al. "Magneto-electric properties of  $x\text{Ni}_{0.7}\text{Zn}_{0.3}\text{Fe}_2\text{O}_4 - (1-x)\text{BaTiO}_3$  multiferroic composites". In: *Ceramics International* 44.1 (2018), pp. 683–694. ISSN: 0272-8842. DOI: [10.1016/j.ceramint.2017.09.229](https://doi.org/10.1016/j.ceramint.2017.09.229).
- [64] Akihito Sawa. "Resistive switching in transition metal oxides". In: *Materials Today* 11.6 (2008), pp. 28–36. ISSN: 1369-7021. DOI: [10.1016/S1369-7021\(08\)70119-6](https://doi.org/10.1016/S1369-7021(08)70119-6).
- [65] Xiaoyan Li et al. "Impact of interfacial coupling of oxygen octahedra on ferromagnetic order in  $\text{La}_{0.7}\text{Sr}_{0.3}\text{MnO}_3$  heterostructures". In: *Scientific Reports* 7.1 (Jan. 2017), p. 40068. ISSN: 2045-2322. DOI: [10.1038/srep40068](https://doi.org/10.1038/srep40068).
- [66] V. M. Goldschmidt. "Die Gesetze der Krystallochemie". In: *Naturwissenschaften* 14.21 (1926), pp. 477–485. ISSN: 1432-1904. DOI: [10.1007/BF01507527](https://doi.org/10.1007/BF01507527).
- [67] J.M. Longo J.B. Goodenough and K.H. Hellwege. "Crystallographic and Magnetic Properties of Perovskite and Perovskite-Related Compounds (Ed)". In: *Colossal Magnetoresistance, Charge Ordering and Related Properties of Manganese Oxides*, New Series III 4a, Springer-Verlag, Berlin, 126.
- [68] H. Y. Hwang et al. "Lattice Effects on the Magnetoresistance in Doped  $\text{LaMnO}_3$ ". In: *Phys. Rev. Lett.* 75 (5 1995), pp. 914–917. DOI: [10.1103/PhysRevLett.75.914](https://doi.org/10.1103/PhysRevLett.75.914).
- [69] Sven Uhlenbruck. "Transporteigenschaften von dotierten Manganaten". PhD thesis. Universität zu Köln, 2000.
- [70] J. R. Sun, G. H. Rao, and J. K. Liang. "Crystal structure and electronic transport property of perovskite manganese oxides with a fixed tolerance factor". In: *Applied Physics Letters* 70.14 (1997), pp. 1900–1902. DOI: [10.1063/1.118725](https://doi.org/10.1063/1.118725).
- [71] Zhou Shengming et al. "The effect of cation disorder on electrical transport properties of  $\text{Nd}_{0.7}(\text{Ca}, \text{Sr}, \text{Ba})_{0.3}\text{MnO}_3$ ". In: *Journal of Physics: Condensed Matter* 11.36 (1999), pp. 6877–6882. DOI: [10.1088/0953-8984/11/36/305](https://doi.org/10.1088/0953-8984/11/36/305).
- [72] "Lehrbuch der Anorganischen Chemie". In: ed. by A.F. Holleman und E. Wiberg. 91,-100. Aufl., de Gruyter Berlin, S.126, 1985.
- [73] Y. Tokura and N. Nagaosa. "Orbital Physics in Transition-Metal Oxides". In: *Science* 288.5465 (2000), pp. 462–468. ISSN: 0036-8075. DOI: [10.1126/science.288.5465.462](https://doi.org/10.1126/science.288.5465.462).
- [74] "Chemie". In: *Das Basiswissen der Chemie*. Ed. by Ch. E. Mortimer. Georg Thieme Verlag Stuttgart, 1987, 484 ff.
- [75] H. A. Jahn, E. Teller, and Frederick George Donnan. "Stability of polyatomic molecules in degenerate electronic states - I-Orbital degeneracy". In: *Proceedings of the Royal Society of London. Series A - Mathematical*

- and Physical Sciences* 161.905 (1937), pp. 220–235. DOI: [10.1098/rspa.1937.0142](https://doi.org/10.1098/rspa.1937.0142).
- [76] Kliment I Kugel' and D I Khomskii. "The Jahn-Teller effect and magnetism: transition metal compounds". In: *Soviet Physics Uspekhi* 25.4 (1982), pp. 231–256. DOI: [10.1070/pu1982v025n04abeh004537](https://doi.org/10.1070/pu1982v025n04abeh004537).
- [77] E. Müller Hartmann. *Einführung in die theoretische Festkörperphysik II: Ausgewählte Probleme aus der Theorie korrelierter Elektronensysteme, Vorlesung*. 1999.
- [78] F. Moussa et al. "Spin waves in the antiferromagnet perovskite  $\text{LaMnO}_3$ : A neutron-scattering study". In: *Phys. Rev. B* 54 (21 1996), pp. 15149–15155. DOI: [10.1103/PhysRevB.54.15149](https://doi.org/10.1103/PhysRevB.54.15149).
- [79] Q. Huang et al. "Structure and magnetic order in undoped lanthanum manganite". In: *Phys. Rev. B* 55 (22 1997), pp. 14987–14999. DOI: [10.1103/PhysRevB.55.14987](https://doi.org/10.1103/PhysRevB.55.14987).
- [80] E. O. Wollan and W. C. Koehler. "Neutron Diffraction Study of the Magnetic Properties of the Series of Perovskite-Type Compounds  $[(1-x)\text{La}, x\text{Ca}]\text{MnO}_3$ ". In: *Phys. Rev.* 100 (2 1955), pp. 545–563. DOI: [10.1103/PhysRev.100.545](https://doi.org/10.1103/PhysRev.100.545).
- [81] A. Urushibara et al. "Insulator-metal transition and giant magnetoresistance in  $\text{La}_{1-x}\text{Sr}_x\text{MnO}_3$ ". In: *Phys. Rev. B* 51 (20 1995), pp. 14103–14109. DOI: [10.1103/PhysRevB.51.14103](https://doi.org/10.1103/PhysRevB.51.14103).
- [82] "Einführung in die Festkörperphysik". In: ed. by K. Kopitzki. 2. Aufl., Teubner, Stuttgart, 1989, p. 206.
- [83] P. Fazekas. *Lecture Notes on Electron Correlation and Magnetism, Series in Modern Condensed Matter Physics, Vol. 5, World Scientific, Singapur*, S. 137.
- [84] E. Müller Hartmann. *Einführung in die theoretische Festkörperphysik II: Ausgewählte Probleme aus der Theorie korrelierter Elektronensysteme, Vorlesung*. 1997.
- [85] E. Müller Hartmann. "Überlegungen zur Theorie der Hochtemperatursupraleiter". In: *in 19. IFF Ferienkurs: Supraleitung und verwandte Quantenphänomene*. 1988.
- [86] "Festkörperphysik". In: ed. by Rudolf Gross and Achim Marx. De Gruyter Studium, 2018.
- [87] Anthony Arulraj et al. "Insulator–Metal Transitions, Giant Magnetoresistance, and Related Aspects of the Cation-Deficient  $\text{LaMnO}_3$  Compositions  $\text{La}_{1-t}\text{MnO}_3$  and  $\text{LaMn}_{1-t}\text{O}_3$ ". In: *Journal of Solid State Chemistry* 127.1 (1996), pp. 87–91. ISSN: 0022-4596. DOI: [10.1006/jssc.1996.0360](https://doi.org/10.1006/jssc.1996.0360).
- [88] Bjørn C. Hauback, Helmer Fjellvåg, and Natsuko Sakai. "Effect of Nonstoichiometry on Properties of  $\text{La}_{1-t}\text{MnO}_{3+}$ : III. Magnetic Order Studied by Powder Neutron Diffraction". In: *Journal of Solid State Chemistry* 124.1 (1996), pp. 43–51. ISSN: 0022-4596. DOI: [10.1006/jssc.1996.0205](https://doi.org/10.1006/jssc.1996.0205).

- [89] C. Ritter et al. "Influence of oxygen content on the structural, magneto-transport, and magnetic properties of  $\text{LaMnO}_{3-\delta}$ ". In: *Phys. Rev. B* 56 (14 1997), pp. 8902–8911. DOI: [10.1103/PhysRevB.56.8902](https://doi.org/10.1103/PhysRevB.56.8902).
- [90] A. Einstein. "Über einen die Erzeugung und Verwandlung des Lichtes betreffenden heuristischen Gesichtspunkt". In: *Annalen der Physik* 322.6 (1905), pp. 132–148. DOI: [10.1002/andp.19053220607](https://doi.org/10.1002/andp.19053220607).
- [91] "Photoelectron spectroscopy: Principles and applications, Volume 82". In: ed. by S. Hüfner. Springer-Verlag, Berlin and New York, 1995.
- [92] J.B. Pendry. "Theory of photoemission". In: *Surface Science* 57.2 (1976), pp. 679–705. ISSN: 0039-6028. DOI: [10.1016/0039-6028\(76\)90355-1](https://doi.org/10.1016/0039-6028(76)90355-1).
- [93] Bradley H Frazer et al. "The probing depth of total electron yield in the sub-keV range: TEY-XAS and X-PEEM". In: *Surface Science* 537.1 (2003), pp. 161–167. ISSN: 0039-6028. DOI: [10.1016/S0039-6028\(03\)00613-7](https://doi.org/10.1016/S0039-6028(03)00613-7).
- [94] S. Tanuma, C. J. Powell, and D. R. Penn. "Calculations of electron inelastic mean free paths. IX. Data for 41 elemental solids over the 50 eV to 30 keV range". In: *Surface and Interface Analysis* 43.3 (2011), pp. 689–713. DOI: [10.1002/sia.3522](https://doi.org/10.1002/sia.3522).
- [95] J.M. Hackl. "Reduction properties of a model ceria catalyst at the microscopic scale". PhD thesis. Research Centre Jülich GmbH, PGI-6, 2018.
- [96] National Institute for Standards and Technology. *NIST X-ray Photoelectron Spectroscopy Database, Version 4.1*. 2012.
- [97] "Magnetismus: From Fundamentals to Nanoscale Dynamics". In: ed. by J. Stöhr und H.C. Siegmann. Springer-Verlag, Berlin and Heidelberg, 2006.
- [98] F. M. F. de Groot et al. "2p x-ray absorption of 3d transition-metal compounds: An atomic multiplet description including the crystal field". In: *Phys. Rev. B* 42 (9 1990), pp. 5459–5468. DOI: [10.1103/PhysRevB.42.5459](https://doi.org/10.1103/PhysRevB.42.5459).
- [99] Hidekazu Ikeno et al. "Multiplet calculations of  $L_{2,3}$  x-ray absorption near-edge structures for 3d transition-metal compounds". In: *Journal of Physics: Condensed Matter* 21.10 (2009), p. 104208. DOI: [10.1088/0953-8984/21/10/104208](https://doi.org/10.1088/0953-8984/21/10/104208).
- [100] B. T. Thole et al. "X-ray circular dichroism as a probe of orbital magnetization". In: *Phys. Rev. Lett.* 68 (12 1992), pp. 1943–1946. DOI: [10.1103/PhysRevLett.68.1943](https://doi.org/10.1103/PhysRevLett.68.1943).
- [101] Paolo Carra et al. "X-ray circular dichroism and local magnetic fields". In: *Phys. Rev. Lett.* 70 (5 1993), pp. 694–697. DOI: [10.1103/PhysRevLett.70.694](https://doi.org/10.1103/PhysRevLett.70.694).
- [102] J. Stöhr and H. König. "Determination of Spin- and Orbital-Moment Anisotropies in Transition Metals by Angle-Dependent X-Ray Magnetic Circular Dichroism". In: *Phys. Rev. Lett.* 75 (20 1995), pp. 3748–3751. DOI: [10.1103/PhysRevLett.75.3748](https://doi.org/10.1103/PhysRevLett.75.3748).

- [103] E. Brüche. "Elektronenmikroskopische Abbildung mit lichtelektrischen Elektronen". In: *Zeitschrift für Physik* 86.7 (July 1933), pp. 448–450. ISSN: 0044-3328. DOI: [10.1007/BF01341360](https://doi.org/10.1007/BF01341360).
- [104] E. Brüche and W. Knecht. "Bemerkung über die Erreichung hoher Auflösungen mit dem elektronenoptischen Immersionsobjektiv". In: *Zeitschrift für Physik* 92.7 (July 1934), pp. 462–466. DOI: [10.1007/BF01339351](https://doi.org/10.1007/BF01339351).
- [105] F. Nickel. "Aberrationskorrigierte Photoemissionsmikroskopie an magnetischen Systemen: Von statischer Charakterisierung zu zeitaufgelöster Abbildung," PhD thesis. Universität Duisburg-Essen, 2013.
- [106] S. Cramm. *Probing the Nanoworld - Synchrotron Radiation Sources and Beamlines: Overview, IFF Spring School Lecture Notes, vol. 38, chap. B2*. 2007.
- [107] "Elements of Modern X-ray Physics, 2nd Edition". In: ed. by J. Als-Nielsen and D. McMorrow. John Wiley Sons, 2011.
- [108] Gertjan Koster et al. "Quasi-ideal Strontium Titanate Crystal Surfaces through Formation of Strontium Hydroxide". In: *Applied Physics Letters* 73 (Nov. 1998), pp. 2920–2922. DOI: [10.1063/1.122630](https://doi.org/10.1063/1.122630).
- [109] Jong Hyun Song, Tomofumi Susaki, and Harold Y. Hwang. "Enhanced Thermodynamic Stability of Epitaxial Oxide Thin Films". In: *Advanced Materials* 20.13 (), pp. 2528–2532. DOI: [10.1002/adma.200701919](https://doi.org/10.1002/adma.200701919).
- [110] Chunrui Ma and Chonglin Chen. "Pulsed Laser Deposition for Complex Oxide Thin Film and Nanostructure". In: *Advanced Nano Deposition Methods*. John Wiley Sons, Ltd, 2016. Chap. 1, pp. 1–31. ISBN: 9783527696406. DOI: [10.1002/9783527696406.ch1](https://doi.org/10.1002/9783527696406.ch1).
- [111] P. R. Willmott and J. R. Huber. "Pulsed laser vaporization and deposition". In: *Rev. Mod. Phys.* 72 (1 2000), pp. 315–328. DOI: [10.1103/RevModPhys.72.315](https://doi.org/10.1103/RevModPhys.72.315).
- [112] Hans Christen and Gyula Eres. "Recent advances in pulsed-laser deposition of complex oxides". In: *Journal of physics. Condensed matter : an Institute of Physics journal* 20 (July 2008), p. 264005. DOI: [10.1088/0953-8984/20/26/264005](https://doi.org/10.1088/0953-8984/20/26/264005).
- [113] Zhaoyan Zhang, Zhen-Xue Han, and George S. Dulikravich. "Numerical simulation of laser induced plasma during pulsed laser deposition". In: *Journal of Applied Physics* 90.12 (2001), pp. 5889–5897. DOI: [10.1063/1.1415068](https://doi.org/10.1063/1.1415068).
- [114] A. Miotello and R. Kelly. "Laser-induced phase explosion: new physical problems when a condensed phase approaches the thermodynamic critical temperature". In: *Applied Physics A* 69.1 (1999), S67–S73. ISSN: 1432-0630. DOI: [10.1007/s003399900296](https://doi.org/10.1007/s003399900296).
- [115] J. F. Mitchell et al. "Structural phase diagram of  $\text{La}_{1-x}\text{Sr}_x\text{MnO}_{3+\delta}$ : Relationship to magnetic and transport properties". In: *Phys. Rev. B* 54 (9 1996), pp. 6172–6183. DOI: [10.1103/PhysRevB.54.6172](https://doi.org/10.1103/PhysRevB.54.6172).

- [116] Marianna Španková et al. "Characterization of Epitaxial LSMO Films Grown on STO Substrates". In: *Acta Physica Polonica A* 131 (Apr. 2017), pp. 848–850. DOI: [10.12693/APhysPolA.131.848](https://doi.org/10.12693/APhysPolA.131.848).
- [117] F. Gunkel. "The role of defects at functional interfaces between polar and non-polar perovskite oxides". PhD thesis. Forschungszentrum Jülich GmbH, Peter - Grünberg - Institut 7, 2013.
- [118] Rajiv K. Singh and J. Narayan. "Pulsed-laser evaporation technique for deposition of thin films: Physics and theoretical model". In: *Phys. Rev. B* 41 (13 1990), pp. 8843–8859. DOI: [10.1103/PhysRevB.41.8843](https://doi.org/10.1103/PhysRevB.41.8843).
- [119] A.J.H.M. Rijnders. "The initial growth of complex oxides: study and manipulation". PhD thesis. Enschede: University of Twente, 2001.
- [120] L Ranno et al. "Influence of substrate temperature on magnetotransport properties of thin films of  $\text{La}_{0.7}\text{Sr}_{0.3}\text{MnO}_3$ ". In: *Applied Surface Science* 138-139 (1999), pp. 228–232. ISSN: 0169-4332. DOI: [10.1016/S0169-4332\(98\)00400-0](https://doi.org/10.1016/S0169-4332(98)00400-0).
- [121] Jos E. Boschker et al. "Consequences of High Adatom Energy during Pulsed Laser Deposition of  $\text{La}_{0.7}\text{Sr}_{0.3}\text{MnO}_3$ ". In: *Crystal Growth & Design* 12.2 (Feb. 2012), pp. 562–566. ISSN: 1528-7483. DOI: [10.1021/cg201461a](https://doi.org/10.1021/cg201461a).
- [122] Hangwen Guo et al. "Growth diagram of  $\text{La}_{0.7}\text{Sr}_{0.3}\text{MnO}_3$  thin films using pulsed laser deposition". In: *Journal of Applied Physics* 113.23 (2013), p. 234301. DOI: [10.1063/1.4811187](https://doi.org/10.1063/1.4811187).
- [123] Min Zhang et al. "Transport properties and microstructure of  $\text{La}_{0.7}\text{Sr}_{0.3}\text{MnO}_3$  nanocrystalline thin films grown by polymer-assisted chemical solution deposition". In: *Journal of Modern Transportation* 22.1 (2014), pp. 50–54. ISSN: 2196-0577. DOI: [10.1007/s40534-014-0032-4](https://doi.org/10.1007/s40534-014-0032-4).
- [124] O.J. González et al. "Room temperature colossal magnetoresistance in nanocrystalline  $\text{La}_{0.67}\text{Sr}_{0.33}\text{MnO}_3$  sputtered thin films". In: *Journal of Magnetism and Magnetic Materials* 222.1 (2000), pp. 199–206. ISSN: 0304-8853. DOI: [10.1016/S0304-8853\(00\)00534-5](https://doi.org/10.1016/S0304-8853(00)00534-5).
- [125] A. Chikamatsu et al. "In situ angle-resolved photoemission study on  $\text{La}_{1-x}\text{Sr}_x\text{MnO}_3$  thin films grown by laser MBE". In: *Journal of Electron Spectroscopy and Related Phenomena* 144-147 (2005). Proceeding of the Fourteenth International Conference on Vacuum Ultraviolet Radiation Physics, pp. 511–514. ISSN: 0368-2048. DOI: [10.1016/j.elspec.2005.01.024](https://doi.org/10.1016/j.elspec.2005.01.024).
- [126] M. Wilhelm. "Evolution of Magnetic Properties and Electronic Structure at Critical Thicknesses of  $\text{La}_{0.7}\text{Sr}_{0.3}\text{MnO}_3$  Thin Films". MA thesis. Forschungszentrum Jülich GmbH, Peter - Grünberg - Institut 6/7, 2016.
- [127] P. H. Dederichs. *B.I., Elastizitätstheorie und Gitterverzerrungen, in Ferienkurs 82, Physikalische Grundlagen metallischer Werkstoffe*. 1982.
- [128] D Sander. "The correlation between mechanical stress and magnetic anisotropy in ultrathin films". In: *Reports on Progress in Physics* 62.5 (1999), pp. 809–858. DOI: [10.1088/0034-4885/62/5/204](https://doi.org/10.1088/0034-4885/62/5/204).

- [129] Anders Sandell and Alexander J. Jaworowski. "The Mn 2p core-level photoelectron spectrum of Pd–Mn bimetallic systems on Pd(100)". In: *Journal of Electron Spectroscopy and Related Phenomena* 135.1 (2004), pp. 7–14. ISSN: 0368-2048. DOI: [10.1016/j.elspec.2003.11.005](https://doi.org/10.1016/j.elspec.2003.11.005).
- [130] Michel van Veenendaal. "Competition between screening channels in core-level x-ray photoemission as a probe of changes in the ground-state properties of transition-metal compounds". In: *Phys. Rev. B* 74 (8 2006), p. 085118. DOI: [10.1103/PhysRevB.74.085118](https://doi.org/10.1103/PhysRevB.74.085118).
- [131] C. Schlueter et al. "Evidence of electronic band redistribution in  $\text{La}_{0.65}\text{Sr}_{0.35}\text{MnO}_{3-\delta}$  by hard x-ray photoelectron spectroscopy". In: *Phys. Rev. B* 86 (15 2012), p. 155102. DOI: [10.1103/PhysRevB.86.155102](https://doi.org/10.1103/PhysRevB.86.155102).
- [132] V. R. Galakhov et al. "Mn 3s exchange splitting in mixed-valence manganites". In: *Phys. Rev. B* 65 (11 2002), p. 113102. DOI: [10.1103/PhysRevB.65.113102](https://doi.org/10.1103/PhysRevB.65.113102).
- [133] M. L. Wilson et al. "Effects of defects on magnetoresistivity in  $\text{La}_{0.7}\text{Sr}_{0.3}\text{MnO}_3$ ". In: *Journal of Applied Physics* 81.8 (1997), pp. 4971–4973. DOI: [10.1063/1.365016](https://doi.org/10.1063/1.365016).
- [134] Sayani Majumdar. "Pulsed laser deposition of  $\text{La}_{1-x}\text{Sr}_x\text{MnO}_3$ : Thin-film properties and spintronic applications". In: *Journal of Physics D Applied Physics* 47 (Dec. 2013), p. 034010. DOI: [10.1088/0022-3727/47/3/034010](https://doi.org/10.1088/0022-3727/47/3/034010).
- [135] Åsmund Monsen et al. "Thickness dependence of dynamic and static magnetic properties of pulsed laser deposited  $\text{La}_{0.7}\text{Sr}_{0.3}\text{MnO}_3$  films on  $\text{SrTiO}_3(001)$ ". In: *Journal of Magnetism and Magnetic Materials* 369 (2014), pp. 197–204. ISSN: 0304-8853. DOI: [10.1016/j.jmmm.2014.06.038](https://doi.org/10.1016/j.jmmm.2014.06.038).
- [136] J. M. D. Coey et al. "Electron Localization in Mixed-Valence Manganites". In: *Phys. Rev. Lett.* 75 (21 1995), pp. 3910–3913. DOI: [10.1103/PhysRevLett.75.3910](https://doi.org/10.1103/PhysRevLett.75.3910).
- [137] Xiaoyan Li et al. "Impact of interfacial coupling of oxygen octahedra on ferromagnetic order in  $\text{La}_{0.7}\text{Sr}_{0.3}\text{MnO}_3/\text{SrTiO}_3$  heterostructures". In: *Scientific Reports* 7.1 (Jan. 2017), p. 40068. DOI: [10.1038/srep40068](https://doi.org/10.1038/srep40068).
- [138] M. Huijben et al. "Critical thickness and orbital ordering in ultrathin  $\text{La}_{0.7}\text{Sr}_{0.3}\text{MnO}_3$  films". In: *Phys. Rev. B* 78 (9 2008), p. 094413. DOI: [10.1103/PhysRevB.78.094413](https://doi.org/10.1103/PhysRevB.78.094413).
- [139] Younghak Kim, Sangkyun Ryu, and Hyoungjeen Jeon. "Strain-effected physical properties of ferromagnetic insulating  $\text{La}_{0.88}\text{Sr}_{0.12}\text{MnO}_3$  thin films". In: *RSC Adv.* 9 (5 2019), pp. 2645–2649. DOI: [10.1039/C8RA09851D](https://doi.org/10.1039/C8RA09851D).
- [140] F. Yang et al. "Strain engineering to control the magnetic and magnetotransport properties of  $\text{La}_{0.67}\text{Sr}_{0.33}\text{MnO}_3$  thin films". In: *Applied Physics Letters* 97.9 (2010), p. 092503. DOI: [10.1063/1.3484147](https://doi.org/10.1063/1.3484147).
- [141] M. Hoppe. "Magnetic, structural, and electronic properties of  $\text{NiFe}_2\text{O}_4$  ultrathin films". PhD thesis. Forschungszentrum Jülich GmbH, Peter-Grünberg - Institut 6, 2015.

- [142] C. T. Chen et al. "Experimental Confirmation of the X-Ray Magnetic Circular Dichroism Sum Rules for Iron and Cobalt". In: *Phys. Rev. Lett.* 75 (1 1995), pp. 152–155. DOI: [10.1103/PhysRevLett.75.152](https://doi.org/10.1103/PhysRevLett.75.152).
- [143] Lide Yao et al. "Electron-Beam-Induced Perovskite–Brownmillerite–Perovskite Structural Phase Transitions in Epitaxial  $\text{La}_{2/3}\text{Sr}_{1/3}\text{MnO}_3$  Films". In: *Advanced Materials* 26.18 (2014), pp. 2789–2793. DOI: [10.1002/adma.201305656](https://doi.org/10.1002/adma.201305656).
- [144] Wonjoo Kim et al. "Impact of oxygen exchange reaction at the ohmic interface in Ta<sub>2</sub>O<sub>5</sub>-based ReRAM devices". In: *Nanoscale* 8 (41 2016), pp. 17774–17781. DOI: [10.1039/C6NR03810G](https://doi.org/10.1039/C6NR03810G).
- [145] P. Orgiani et al. "Evidence of direct correlation between out-of-plane lattice parameter and metal-insulator transition temperature in oxygen-depleted manganite thin films". In: *Applied Physics Letters* 100.4 (2012), p. 042404. DOI: [10.1063/1.3676268](https://doi.org/10.1063/1.3676268).
- [146] Aik Jun Tan et al. "Magneto-ionic control of magnetism using a solid-state proton pump". In: *Nature Materials* 18.1 (2019), pp. 35–41. DOI: [10.1038/s41563-018-0211-5](https://doi.org/10.1038/s41563-018-0211-5).
- [147] I.T. Jolliffe. *Principal Components in Regression Analysis*. In: *Principal Component Analysis*. 1986.
- [148] J.E. Jackson. *A User's Guide to Principal Components*. 2004.
- [149] Margret Giesen et al. "Principal component analysis: Reveal camouflaged information in x-ray absorption spectroscopy photoemission electron microscopy of complex thin oxide films". In: *Thin Solid Films* 665 (2018), pp. 75–84. ISSN: 0040-6090. DOI: [10.1016/j.tsf.2018.09.010](https://doi.org/10.1016/j.tsf.2018.09.010).
- [150] Daniel Stadler et al. "Magnetic Field-Assisted Chemical Vapor Deposition of Iron Oxide Thin Films: Influence of Field-Matter Interactions on Phase Composition and Morphology". In: *J. Phys. Chem. Lett.* 10.20 (Oct. 2019), pp. 6253–6259. DOI: [10.1021/acs.jpcllett.9b02381](https://doi.org/10.1021/acs.jpcllett.9b02381).
- [151] Andri Mirzal. "A convergent algorithm for orthogonal nonnegative matrix factorization". In: *Journal of Computational and Applied Mathematics* 260 (2014), pp. 149–166. ISSN: 0377-0427. DOI: [10.1016/j.cam.2013.09.022](https://doi.org/10.1016/j.cam.2013.09.022).
- [152] Ruimin Qiao et al. "Spectroscopic fingerprints of valence and spin states in manganese oxides and fluorides". In: *Current Applied Physics* 13.3 (2013), pp. 544–548. ISSN: 1567-1739. DOI: [10.1016/j.cap.2012.09.017](https://doi.org/10.1016/j.cap.2012.09.017).
- [153] M. P. de Jong et al. "Evidence for  $\text{Mn}^{2+}$  ions at surfaces of  $\text{La}_{0.7}\text{Sr}_{0.3}\text{MnO}_3$  thin films". In: *Phys. Rev. B* 71 (1 2005), p. 014434. DOI: [10.1103/PhysRevB.71.014434](https://doi.org/10.1103/PhysRevB.71.014434).
- [154] G van der Laan and I W Kirkman. "The 2p absorption spectra of 3d transition metal compounds in tetrahedral and octahedral symmetry". In: *Journal of Physics: Condensed Matter* 4.16 (1992), pp. 4189–4204. DOI: [10.1088/0953-8984/4/16/019](https://doi.org/10.1088/0953-8984/4/16/019).

- [155] Jorge J. Moré. "The Levenberg-Marquardt algorithm: Implementation and theory". In: *Numerical Analysis*. Ed. by G. A. Watson. Berlin, Heidelberg: Springer Berlin Heidelberg, 1978, pp. 105–116. ISBN: 978-3-540-35972-2.
- [156] B. Cui et al. "Tuning the entanglement between orbital reconstruction and charge transfer at a film surface". In: *Scientific Reports* 4.1 (Feb. 2014), p. 4206. ISSN: 2045-2322. DOI: [10.1038/srep04206](https://doi.org/10.1038/srep04206).
- [157] L. F.J. Piper et al. "Erratum: Soft X-ray spectroscopic study of dense strontium-doped lanthanum manganite cathodes for solid oxide fuel cell applications (Journal of Electrochemical Society (2011) B99 (158))". English. In: *Journal of the Electrochemical Society* 158.4 (Apr. 2011). ISSN: 0013-4651. DOI: [10.1149/1.3549649](https://doi.org/10.1149/1.3549649).
- [158] Zhipeng Li et al. "Interface and Surface Cation Stoichiometry Modified by Oxygen Vacancies in Epitaxial Manganite Films". In: *Advanced Functional Materials* 22.20 (2012), pp. 4312–4321. DOI: [10.1002/adfm.201200143](https://doi.org/10.1002/adfm.201200143).
- [159] J-S Lee et al. "Reversed remanent magnetic configuration in epitaxial  $\text{La}_{1-x}\text{Sr}_x\text{MnO}_3$  films". In: *Journal of Physics D: Applied Physics* 44.24 (2011), p. 245002. DOI: [10.1088/0022-3727/44/24/245002](https://doi.org/10.1088/0022-3727/44/24/245002).
- [160] T. Taniuchi et al. "Observation of step-induced magnetic domain formation in  $\text{La}_{1-x}\text{Sr}_x\text{MnO}_3$  thin films by photoelectron emission microscopy". In: *Applied Physics Letters* 89.11 (2006), p. 112505. DOI: [10.1063/1.2347895](https://doi.org/10.1063/1.2347895).
- [161] Magnus Moreau, Sverre Selbach, and Thomas Tybell. "Spatially Confined Spin Polarization and magnetic sublattice control in  $(\text{La,Sr})\text{MnO}_{3-\delta}$  Thin Films by Oxygen Vacancy Ordering". In: *Scientific Reports* 7 (June 2017), p. 4386. DOI: [10.1038/s41598-017-04103-y](https://doi.org/10.1038/s41598-017-04103-y).
- [162] B. R. K. Nanda and S. Satpathy. "Spin-Polarized Two-Dimensional Electron Gas at Oxide Interfaces". In: *Phys. Rev. Lett.* 101 (12 2008), p. 127201. DOI: [10.1103/PhysRevLett.101.127201](https://doi.org/10.1103/PhysRevLett.101.127201).
- [163] W. E. Pickett, R. E. Cohen, and H. Krakauer. "Precise band structure and Fermi-surface calculation for  $\text{YBa}_2\text{Cu}_3\text{O}_7$ : Importance of three-dimensional dispersion". In: *Phys. Rev. B* 42 (13 1990), pp. 8764–8767. DOI: [10.1103/PhysRevB.42.8764](https://doi.org/10.1103/PhysRevB.42.8764).
- [164] José M. Alonso et al. "Influence of the Synthetic Pathway on the Properties of Oxygen-Deficient Manganese-Related Perovskites". In: *European Journal of Inorganic Chemistry* 2007.21 (2007), pp. 3350–3355. DOI: [10.1002/ejic.200700108](https://doi.org/10.1002/ejic.200700108).
- [165] A. Locatelli. *Detector Gating for Time Resolved Measurements*. Trieste and Italy, 2012.
- [166] Elettra Synchrotron. Elettra Parameters. 2015.
- [167] A. Locatelli et al. "High lateral resolution spectroscopic imaging of surfaces: The undulator beamline "nanospectroscopy" at Elettra". In: *J. Phys. IV France* 104 (2003), pp. 99–102. DOI: [10.1051/jp4:200300038](https://doi.org/10.1051/jp4:200300038).

- 
- [168] M. Kanai, H. Tanaka, and T. Kawai. "Origin of metal-insulator transition temperature enhancement in  $\text{La}_{0.8}\text{Ba}_{0.2}\text{MnO}_3$  thin films as determined by structural analysis". In: *Phys. Rev. B* 70 (12 2004), p. 125109. DOI: [10.1103/PhysRevB.70.125109](https://doi.org/10.1103/PhysRevB.70.125109).

---

## Acknowledgements

---

At the end, I would like to express my sincere thanks to all the people who have supported me during my work and contributed to the successful completion of this thesis.

First of all, I owe my gratitude to my advisor Prof. Dr. Claus M. Schneider for giving me the chance to join the PGI-6 institute, which gave me the opportunity to work in an excellent environment for my research. Thank you for supervising and personally supporting my project and in particular for the numerous of inspiring discussions.

Furthermore, I would like to thank Prof. Dr. Martina Müller not only for being the 2nd reviewer of this thesis, but also for the warm and friendly welcome into her research group (Oxide Spintronics Lab) and always having an open door.

I would like to explicitly thank Prof. Dr. Regina Dittmann for both her scientific and personal support. I am grateful for all the fruitful discussions, advices, technical guidance and encouragements.

Special thanks goes to Dr. Tomas Duchon for his enormous support during important beamtimes and beyond that, I like to thank you for a fruitful collaboration, your significant contribution to my work and for your inexhaustible patience.

Also Grateful thanks to Dr. Margret Giesen for her great commitment and the numerous PCA calculations.

Thanks to Dr. Carsten Wiemann for supervising my research and proofreading my thesis on short notice. In particular, thank you for lively discussions with coffee and Knoppers.

This work is a result of great collaborations with other institutes. Thus, I would like to thank Dr. Christoph Bäumer, Dr. Marco Moors and Miriam Glöß for their experimental support and expertise. I like to thank Prof. Dr. Regina Dittmann and Dr. Felix Gunkel for teaching me the operation of the PLD and fundamental characterization methods. Thanks to Rene Borowski,

who introduced me to the secrets of the cleanroom (PGI-7, Forschungszentrum Jülich GmbH, 52425 Jülich, Germany).

Further, I appreciate the cooperation with Dr. Oleg Petravic, Dr. Lei Cao and Hengbo Zhang (Jülich Centre for Neutron Science (JCNS-2) and Peter-Grünberg-Institute (PGI-4), JARA-FIT, Forschungszentrum Jülich GmbH, 52425 Jülich, Germany).

Thanks to Slavomir Nemsak and Alfa T. N'Diaye for enabling first proof of principles studies at the LEEM/PEEM beamline at BESSY II and ALS (PGI-6, Advanced Light Source, Lawrence Berkeley National Laboratory, Berkeley, CA 94720, USA).

Thanks goes to Johanna Hackl and Stefan Cramm for enduring and fruitful beamline support (PGI-6).

Thanks goes to my colleagues from the Oxide Spintronics Lab: Timm Gerber, Tristan Heider, Patrick Lömker, Ronja Heinen, Mai Hussein Hamed and Paul Rosenberger.

I thank my family and my friends for their continued support during my entire studies and the PhD time.

---

## Own Publications

---

- [1] M. Wilhelm, Margret Giesen, Tomáš Duchoň, Marco Moors, David N. Mueller, Johanna Hackl, Christoph Baeumer, Mai Hussein Hamed, Lei Cao, Hengbo Zhang, Oleg Petravic, Maria Glöß, Stefan Cramm, Slavomír Nemšák, Carsten Wiemann, Regina Dittmann, Claus M. Schneider, and Martina Müller. "Photoemission electron microscopy of magneto-ionic effects in  $\text{La}_{0.7}\text{Sr}_{0.3}\text{MnO}_3$ ". In: *APL Materials* 8, 111102 (2020). DOI:10.1063/5.0022150.
- [2] M. Weber, Marek Wilhelm, Lei Jin, Uwe Breuerg, Regina Dittmann, Rainer Waser, Olivier Guillona, Christian Lenser, and Felix Gunkel. "Transport of Embedded Nanoparticles in Defect Engineered Perovskite Layers". In: *ACS Nano* 15, 3, 4546–4560 (2021). DOI:10.1021/acsnano.0c08657.
- [3] Mai Hussein Hamed, Ronja Anika Hinz, Patrick Lomker, Marek Wilhelm, Andrei Gloskovskii, Peter Bencok, Carolin Schmitz-Antoniak, Hebatalla El-naggar, Claus M. Schneider, Martina Muller. "Tunable Magnetic Phases at  $\text{Fe}_3\text{O}_4/\text{SrTiO}_3$  Oxide Interfaces". In: *ACS Appl. Mater. Interfaces* 11, 7, 7576-7583 (2019). DOI:10.1021/acсами.8b20625.



---

## Conference Contributions

---

- [1] M. Wilhelm, T. Gerber, P. Lömker, R. Heinen, F. Gunkel, R. Dittmann, A. Gloskovskii, W. Drube, M. Gorgoi, C.M. Schneider, M. Müller, "*Evolution of Magnetic Properties and Electronic Structure at Critical Thicknesses of  $La_{0.7}Sr_{0.3}MnO_3$  Thin Films*", Poster, DPG- Frühjahrstagung, Dresden, 2017.
- [2] M. Wilhelm, C. Wiemann, C. Schmitz, A. Gloskowskii, W. Drube, and C.M. Schneider, "*Photoemission Microscopy using Hard X-rays Recent State of HAX-PEEM*", Poster, HAXPES Conference 2017, Berkeley Lab, Berkeley (California), 2017.
- [3] M. Wilhelm, T. Gerber, P. Lömker, R. Heinen, F. Gunkel, R. Dittmann, A. Gloskovskii, W. Drube, M. Gorgoi, C.M. Schneider, M. Müller, "*Evolution of Magnetic Properties and Electronic Structure at Critical Thicknesses of  $La_{0.7}Sr_{0.3}MnO_3$  Thin Films*", Poster, HAXPES Conference 2017, Berkeley Lab, Berkeley (California), 2017.
- [4] M. Wilhelm, M. Moors, C. Bäumer, C. Wiemann, R. Dittmann, C.M. Schneider, M. Müller, "*Electric Field Modification of Structure and Magnetism in  $Nb:SrTiO_3/La_{0.7}Sr_{0.3}MnO_3$  Device*", Poster, SFB Conference, Spa (Belgium), 2017.
- [5] M. Wilhelm, M. Moors, C. Bäumer, M. Glöß, C. Wiemann, R. Dittmann, C.M. Schneider, M. Müller, "*Correlation of Oxygen Vacancies and Magnetism in  $La_{0.7}Sr_{0.3}MnO_3$  Thin Films*", Poster, Faraday Discussions, Royal Chemical Society, Aachen, 2018.
- [6] M. Wilhelm, W. Drube, M. Gorgoi, C.M. Schneider, M. Müller, "*Correlation of Oxygen Vacancies and Magnetism  $La_{0.7}Sr_{0.3}MnO_3$  Thin Films in Vertical Memristive Devices*", Talk, Joint European Magnetic Symposia (JEMS), Mainz, 2018.
- [7] M. Wilhelm, M. Giesen, M. Moors, C. Bäumer, M. Hussein Hamed, J. Hackl, L. Cao, H. Zhang, T. Duchon, M. Glöß, O. Petravic, S. Cramm, S. Nemsak, C. Wiemann, R. Dittmann, M. Müller, C.M. Schneider, "*Transition of the Magnetic Exchange Coupling Induced by Oxygen Vacancies in  $La_{0.7}Sr_{0.3}MnO_3$  Thin Films*", Poster, Heraeus Seminar, Bad Honnef, 2020.

02/2017 - 11/2020 **Forschungszentrum Jülich GmbH,**

# DuEPublico

Duisburg-Essen Publications online

UNIVERSITÄT  
D U I S B U R G  
E S S E N

*Offen im Denken*

ub | universitäts  
bibliothek

Diese Dissertation wird via DuEPublico, dem Dokumenten- und Publikationsserver der Universität Duisburg-Essen, zur Verfügung gestellt und liegt auch als Print-Version vor.

**DOI:** 10.17185/duepublico/75186

**URN:** urn:nbn:de:hbz:464-20220118-142234-0

Alle Rechte vorbehalten.